INVESTIGATION OF NANOSTRUCTURES FOR HIGHLY SENSITIVE SURFACE PLASMON RESONANCE SENSORS

by

HUSSEIN AKAFZADE

Presented to the Faculty of the Graduate School of
The University of Texas at Arlington in Partial Fulfillment
of the Requirements
for the Degree of

DOCTOR OF PHILOSOPHY

THE UNIVERSITY OF TEXAS AT ARLINGTON
August 2020

ACKNOWLEDGEMENTS

I would like to immensely appreciate my great supervising professor, Dr. Suresh C. Sharma, for his amiable character, deep knowledge, and persistent support, which always led me through difficult times. I'm also deeply grateful to have Dr. Nader Hozhabri as an active collaborator and committee member, since his contribution, including thin film preparation, made this work possible.

Special thanks to my other committee members, Dr. Alex Weiss, Dr. Qiming Zhang, and Dr. Ali Koymen for devoting time and expressing their suggestions and corrections. Additional thanks to physics department, for financially supporting its PhD students, and also to physics staff, especially Stacey and Holly, for their ceaseless work. I would like to extend my acknowledgment to the current and previous members in our group, including Kunal Tiwari, Vivek Khickar, and Douglas Zinn, that helped a lot in the lab for data acquisition and analysis.

I would like to also express my sincere gratitude to my parents, siblings, and my beautiful wife Sima, for their encouragement and inspiration throughout these years. My mother's share in enhancing my educational level is unforgettable and I hope to be someone who always makes her proud.

July 1st, 2020

ABSTRACT

INVESTIGATION OF NANOSTRUCTURES FOR
HIGHLY SENSITIVE SURFACE PLASMON RESONANCE SENSORS

Hussein Akafzade, Ph.D.

The University of Texas at Arlington, 2020

Supervising Professor: Dr. Suresh C. Sharma

An extensive study of Surface Plasmon Polaritons (SPPs) and their applications has been undertaken in this work. Highly sensitive surface plasmon resonance sensors, made of noble metals, as well as multilayer nanostructures, are investigated. Detailed simulations are performed to optimize and improve the structure of these sensors. Evanescent fields created on the surface of the sensor are evaluated. It is demonstrated theoretically and experimentally that sensor sensitivity can be increased significantly by choosing the right index of the prism used in our Kretschmann and Fixed Detector Kretschmann Spectrometers.

The interaction of the SPPs and CdSe/ZnS quantum dots that leads to Rabi splitting in the dispersion curve, is studied by COMSOL simulations in relation to the experimen-

tal photoluminescence data obtained previously in our research group. These simulations provide an explanation for the observed shift in the PL wavelength emitted by QDs when coupled to SPPs and meanwhile exposed to a 514 nm laser beam.

Additionally, a new metamaterial nanostructure, consisting of TiN, SiO_2 and HfO_2, is proposed and investigated for applications as an efficient solar absorber. This nanostructure increases absorption of the solar energy up to an unprecedented amount of 98% for wavelengths from 250 to 1100 nm. In case of indirect sunlight incidence, we see a continuous decrease in absorption by going to higher angles, but still it remains higher than 80% for majority of wavelengths for $\theta_{in} < 60^{\circ}$.

TABLE OF CONTENTS

ACKNOWLEDGEMENTS iv

ABSTRACT v

LIST OF ILLUSTRATIONS x

LIST OF TABLES xv

Chapter 1Page

1. The Theory of Surface Plasmon Resonance 1

    1.1 Overview 1

        1.1.1 Drude Model and Bulk Plasmons 2

        1.1.2 Dispersion Relation for SPPs 6

    1.2 SPPs Excitation Methods 12

        1.2.1 Attenuated Total Reflection (ATR) 12

        1.2.2 Grating 22

2. Fabrication of Thin Films and Nano-structures 26

    2.1 Thermal Evaporation 27

        2.1.1 Deposition Control 29

        2.1.2 Chamber's Pressure 29

    2.2 Sputtering 30

2.2.1 Sputter Yield . . . 32
2.2.2 Glow Discharge . . . 32
2.2.3 NanoFab at UT Arlington . . . 34
2.2.4 Characterization using Ellipsometry, SEM, & TEM . . . 36
3. COMSOL Simulations . . . 39
3.1 COMSOL Multiphysics Software . . . 39
3.2 Single Layer Simulations . . . 41
3.3 Multilayer Simulations . . . 47
3.4 Hemispherical Dielectrics on Silver . . . 48
3.5 Grating Simulations of SPPs . . . 51
4. Experiments and Data . . . 54
4.1 Kretschmann Configuration . . . 54
4.2 Fixed Detector System . . . 57
4.3 Sensitivity and Resolution of SPR Signal . . . 58
4.4 Precise Measurements of Glucose Concentration in Distilled Water . . . 61
4.5 SPR Measurements on Several Samples . . . 67
5. Theory and Simulation of Quantum Dots . . . 69
5.1 Quantum Dots and their coupling with SPPs . . . 69
5.2 Simulation of Rabi Splitting . . . 72
5.3 Data on QDs . . . 78
6. Highly Efficient Sunlight Absorber . . . 81
6.1 Previous Studies on Sunlight Absorbers . . . 81
6.2 Suggested Design For The Maximum Absorption . . . 82
6.3 COMSOL Simulations on Absorption Efficiency . . . 83
6.4 Calculations Using Sun Spectrum on Earth . . . 88
6.5 Indirect Light Absorption . . . 88

6.6 Electric Field Strength 91
7. Conclusions and Future Work 94
REFERENCES 97

LIST OF ILLUSTRATIONS

Figure Page

1.1 dielectric constants of Ag ($\tau = 38.15 \times 10^{-15}$, $\omega_P = 13.64 \times 10^{15}$) vs. ω/ω_P 4

1.2 Electric field lines caused by SPPs on the metal-dielectric interface 7

1.3 Evanescent fields spreading into dielectric (blue arrow) and metal (red arrow) 10

1.4 E-Fields in air created by SPPs located at ($z = 0$) on Silver film, in x (left Fig.) and z (right Fig.) directions. Silver is coated on a substrate and is adjacent to air on top 11

1.5 Dispersion Curves of Bulk plasmons and SPPs for a metal in contact with air ($k_P = \omega_P/c$) 12

1.6 A p-polarized laser beam hitting the base of prism with incidence angle θ_i . . 13

1.7 SPR point for Prism/Metal/Air structure and $\omega = 0.4\,\omega_P$ 15

1.8 Simulated reflectivity for 48nm Au film, using p -polarized (left) & s -polarized (right) waves 16

1.9 Elliptic polarized wave, reflected and transmitted at media interface 17

1.10 Light interference in a stack of thin films, with different refractive indices . . 18

1.11 Quantum Mechanical wave passing through a square potential well 20

1.12 Periodic structure like a square-wave, with periodicity of Λ and the height of h; along with its first order Fourier series 23
1.13 Diffraction orders with arbitrary periodicity and wavelength as it's reflected off of a grating structure. 24
2.1 Schematics of Thermal Evaporation Machine using electric current (Left) and E-Beam Machine (Right) 28
2.2 Schematics of Sputtering technique. Ar^+ plasma (green dots) hit the substrate (red slab) in helix motion due to EM Fields and release its molecules (red circles) 31
2.3 Sections of Glow Discharge Tube 33
2.4 Thermal Evaporation Machine 35
2.5 Sputtering Machine 35
2.6 Surface topography of a $5\mu m \times 5\mu m$ region of 50 nm silver film using AFM tip in a non-contact mode at a scanning rate of 0.5 Hertz 37
2.7 SEM Machine at UTA NanoFab used for characterization of our samples . . 38
2.8 SEM pictures of a silver sample use in our experiments. 38
3.1 Reflection plot of Au with varying thickness of 40 to 55 nm in x- direction and angle range of 32 to 40 degrees in y direction. z axis shows the reflectance. 42
3.2 Strength of various components of electric field on gold along with SPR curve, For 1mW laser intensity over 9 mm^2 area 43
3.3 Incidence angle from left to right: 33°, 34°, SPR=35.9°, and 37° in Prism-Gold-Air system 44
3.4 Reflection plot as a function of wavelength and angle for the gold film 45
3.5 Cu SPR and Max E-fields 46
3.6 Ag SPR and Max E-fields 46
3.7 Au SPR and Max E-fields 46

3.8 Al SPR and Max E-fields 46
3.9 $Ag/Si_3N_4/Au/H_2O$ Field with prism index 1.496 and water on top for z (left) and x (right) directions 47
3.10 Resonance condition on Niobium, in case of single layer Nb sensor (left) and multilayer $Ag(50nm)/HfO_2(130nm)/Nb$ (20nm) sensor (right) using 1.78 index prism and He-Ne laser 48
3.11 Reflection from silver sensor with HfO_2 strands 49
3.12 $\theta_{in} = 8.6°$ 50
3.13 $\theta_{in} = 11.2°$ 50
3.14 $\theta_{in} = 24.2°$ 50
3.15 $\theta_{in} = 31°$ 50
3.16 $\theta_{in} = 37°$ 50
3.17 $\theta_{in} = 46°$ 50
3.18 Electric field for prism/silver/HfO_2(half-cylinder)/Air configuration 50
3.19 Grating simulation for $\Lambda = 1\mu m$ (left) and $\Lambda = 1.5\mu m$ (right) of 30nm gold film. Peak to peak in grating is 150 nm 51
3.20 Absorptance plot of a 30nm thick gold film on glass in contact with air and for different periodicities 52
3.21 Vertical Electric field at $\theta_{inc} = 40°$ (left) and $\theta_{inc} = 54°$ (right), Air/Gold-film/Glass. Input laser power is $1mW$ and it's coming from the air side on top. 53
4.1 Schematics for checking polarization of light using Brewster angle. No reflection is detected when the beam is perfectly p-polarized 55
4.2 Kretschmann configuration for creating SPR. Figure from [1] with some corrections 57
4.3 Fixed prism and detector configuration, Figure from [2] 58

4.4 θ_{spr} as a function of dielectric's refractive index for a gold film and prism index of $n = 1.4960$ (left) and $n = 1.7847$ (right) in Kretschmann configuration 59
4.5 Resonance and critical angles as a function of dielectric's refractive index . . 60
4.6 Schematics of structure of a bi-metal waveguide coupled sensor attached to a prism 62
4.7 Liquid holder of our setup 63
4.8 Gold sensor reflectivity data along with simulations 64
4.9 SPR angle vs. index of Glucose solution with various concentrations for single gold layer sensor 65
4.10 Reflectivity data for Ag/Si_3N_4/Au sensor along with simulations 65
4.11 SPR angle vs. index of glucose solution with various concentrations for Ag/Si_3N_4/Au sensor 66
4.12 Index of refraction vs. concentration of glucose, based on results of experiment with Ag/Si_3N_4/Au sensor 66
4.13 SPR data on noble metals 68
4.14 E-field decay length for noble metals at SPR condition 68
5.1 General structure of quantum dots [3] 70
5.2 Size-dependence of quantum dot radiation [4] 70
5.3 Coupled harmonic oscillators 71
5.4 Rabi Split for hypothetical QD coupling with SPPs of silver and $\Omega = 0.1$ . . 73
5.5 Maximum electric field amplitude on gold surface at a range of angles 75
5.6 Meshed structure of SPPs-QDs coupling 76
5.7 Number of emitters, N=0 (a), N=10 (b), N=20 (c), and N=30 (d) in each QD on gold sensor 77
5.8 Number of emitters, N=0 (a), N=5 (b), N=10 (c), and N=20 (d) in each QD on silver sensor 78

5.9 SPR and PL curve for QD thin film coated at the Bi-WC SPR sensor 79
6.1 Top - the metamaterial structure containing TiN/SiO_2/TiN disks/HfO_2disks. Bottom - a unit cell containing six Au NPs 84
6.2 Physics controlled fine mesh of a free triangular type used in COMSOL simulations 85
6.3 Optimization of disk's radius 87
6.4 Optimization of TiN disk's thickness 87
6.5 Optimization of SiO_2 layer's thickness 87
6.6 Optimization by doping with Au NPs 87
6.7 The solar optical spectrum on Earth (black), absorption by the optimized metamaterial (red), and difference between the solar spectrum and absorption by the metamaterial (dashed blue) 89
6.8 Absorption for different angles, p-polarized light 90
6.9 Absorption for different angles, s-polarized light 90
6.10 Evanescent electric fields present in two metamaterial nanostructures: one without Au NPs (left) and another with Au NPs embedded in the material (right) 91
6.11 Relative absorption for disks using Si_3N_4 and HfO_2 93
7.1 M-UTR80 rotation stage by Newport™ 95

LIST OF TABLES

Table Page

4.1 Detection threshold and material's indices that correspond to 200° sensitivity for some commonly used prism types 61

1

The Theory of Surface Plasmon Resonance

1.1 Overview

In this chapter the theoretical aspects of our work is explained and relevant formulas are derived in detail. At first, different types of excitations, including phonon, plasmon, and excitons are discussed. Then we will talk about the interaction between photon and excitons (polariton) especially plasmon polaritons, dispersion relation, and conditions for creating these states. There are important applications for plasmons in optical sensors, which will be investigated as well.

Elementary excitations consist of Phonons, Plasmons, and Excitons. We are primarily interested in studying plasmons here, which are defined as oscillations of a collection of charges, especially electrons, inside or on the surface of a metal. When these oscillations are coupled to photons, or in other words, are created by a beam of light, the resulting quasi-particles are called plasmon polaritons. If these states are created on the surface of material, they are referred to as Surface Plasmon Polaritons (SPPs); and when created inside a metal, they're called Volume Plasmons or Bulk Plasmons. There is also Localized Surface Plasmon concept, which is not discussed here. [5–7]

1.1.1 Drude Model and Bulk Plasmons

According to free electron model, in a metal, electrons are moving randomly at any direction as they collide with other electrons and nuclei. The average speed of each electron is zero even over fairly small period of time.

If we now apply a DC electric field on both sides of the metal's bulk, the average speed of a single electron, based on simplest assumptions and the Newton's second law, is given by

$$\frac{d < v >}{dt} = -\frac{eE}{m}, \tag{1.1}$$

and then,

$$< p >= -eE\tau. \tag{1.2}$$

$< p >$ is the electron's average momentum and e is the magnitude of its electric charge, while τ is the average time between electron's collisions (average scattering time), and m is the effective mass of electron inside the metal. For best conductors like silver and copper, τ is of order of $10^{-14}s$. Overall, under constant electric field, electron has almost steady speed which is proportional to the strength of the field.

Meanwhile we have the definition of current density as:

$$J = ne < v >, \tag{1.3}$$

in which n is the density of electrons inside certain metal, and it's different from one kind of metal to the other, due to the difference in their electron configuration; but its order of magnitude is about $10^{23} cm^{-3}$. Substituting average velocity into this equation results in:

$$J = \frac{ne^2\tau}{m} E = \sigma_0 E. \tag{1.4}$$

The quantity $\sigma_0 = \frac{ne^2\tau}{m}$ is defined as conductivity. Measuring σ_0 allows us to determine the τ. The above discussion is over simplified and in order to determine a more general relation between p and E, we need to consider additional drag force which causes a delayed response of electron to the electric field, due to the lattice collisions. Drude Model, which implements correct classical differential equation for alternating electric field, tells us, [8]

$$\frac{d < p >}{dt} + \frac{< p >}{\tau} = -eE. \tag{1.5}$$

Situation is like induced oscillation under friction force. Now assume that we have a time varying electric field like $E = E_0 e^{i\omega t}$. Since electron also oscillates with the same frequency as electric field, we are safe to say $< p >=< p_0 > e^{i\omega t}$ and then after a few steps we get:

$$J = \frac{ne^2\tau}{m}(\frac{1}{1 - i\omega\tau})E = \frac{\sigma_0}{1 - i\omega\tau} E = \sigma E. \tag{1.6}$$

Combination of above equation with the following Maxwell's equations in free space (permittivity of ϵ_0, permeability of μ_0, and zero net charge)

$$\nabla.E = 0, \;\; \nabla.B = 0, \;\; \nabla \times E = -\frac{\partial B}{\partial t}, \;\; \nabla \times B = \mu_0 J + \mu_0\epsilon_0 \frac{\partial E}{\partial t}, \tag{1.7}$$

leads us to the general formula for dielectric constant of a metal:

$$\epsilon_m(\omega) = 1 + i\frac{\sigma}{\epsilon_0 \omega}. \tag{1.8}$$

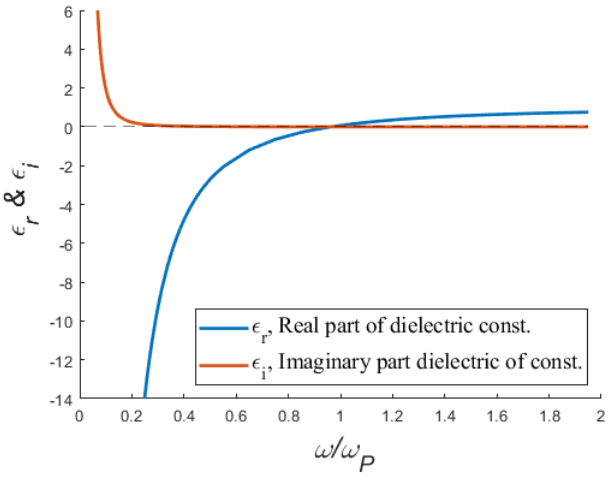

Figure 1.1. dielectric constants of Ag ($\tau = 38.15 \times 10^{-15}$, $\omega_P = 13.64 \times 10^{15}$) vs. ω/ω_P.

Using the exact definition of σ, this can be rewritten as:

$$\epsilon_m(\omega) = 1 - \frac{ne^2\tau/m}{\epsilon_0\omega^2\tau + i\epsilon_0\omega}, \tag{1.9}$$

which has both real and imaginary parts. Let's put $\gamma = 1/\tau$, and $\omega_P = \sqrt{\frac{ne^2}{\epsilon_0 m}}$, so that the real and imaginary parts can be expressed as:

$$\mathbf{Re}(\epsilon_m(\omega)) \equiv \epsilon_r(\omega) = 1 - \frac{\omega_P^2}{\omega^2 + \gamma^2} \overset{\gamma<<\omega}{\simeq} 1 - \frac{\omega_P^2}{\omega^2}, \tag{1.10}$$

$$\mathbf{Im}(\epsilon_m(\omega)) \equiv \epsilon_i(\omega) = \frac{\gamma\omega_P^2}{\omega^3 + \gamma^2\omega}. \tag{1.11}$$

ω_P is an important quantity and it's called plasma frequency. Each metal has specific value of ω_P, which obviously depends on its electron density and electron's effective mass inside that metal. Under the condition of negligible γ (which is a good approximation for most metals in case of visible light); having a frequency less than plasma frequency, metal gets a negative dielectric constant. Otherwise ϵ value is between zero and one. Figure 1.1 shows how the real and imaginary parts of ϵ_m change as a function of frequency.

More realistic model (known as Lorentz-Drude Model) also includes bound electrons. Electric field of light breaks the charge symmetry of these electron's cloud, but they

tend to regain symmetry due to a restoring force by nucleus, with some natural frequency of ω_0. This adds a correction term to equation 1.5, so for bound electrons, it'll be rewritten as:

$$\frac{d^2 < r >}{dt^2} + \frac{1}{\tau}\frac{d < r >}{dt} + \omega_0^2 < r >= -eE/m. \tag{1.12}$$

Multiple kinds of resonators with different ω_0 is possible in a single material, but they won't evenly contribute to $\epsilon_m(\omega)$. Adding solutions for free and bound electrons, with total number of resonators equal to M, gives us:

$$\epsilon_m(\omega) \simeq 1 + \omega_P^2 \sum_{m=1}^{M} \frac{f_m}{\omega_{0,m}^2 - \omega^2 - i\omega\gamma_m}. \tag{1.13}$$

$\omega_{0,m}$ vanishes if the electron is free, while f_m is the weight associated with that term and $\sum_{m=1}^{M} f_m = 1$. Ordinary metals have a plasma frequency much higher than visible light's frequency spectrum. This means, for visible light, the metal's dielectric constant is negative. What does this indicate in terms of reflection and transmission? Having a negative ϵ_m causes high dissipation and damping waves. So the visible light can't penetrate much inside the metal and it's mostly reflected. That's why metals typically look shiny when exposed to sunlight. On the other hand, extra high frequency waves, like X-ray and gamma-ray, can considerably get into the volume of metals, since ϵ_m for those frequencies is positive (Although they get weaker and weaker due to the nucleic collisions).

Suppose a light wave with $\omega > \omega_P$ hits a metal. Then we are sure that $\epsilon_m \simeq \epsilon_r > 0$, and it can be securely replaced with k^2c^2/ω^2, (k is the wavevector of the light and c is the speed of light in vacuum), based on the fact that in general $k^2 = \epsilon\frac{\omega^2}{c^2}$. If we do so in equation 1.10, it gives us the equation:

$$k^2c^2/\omega^2 = 1 - \omega_P^2/\omega^2,$$

that can be rearranged as:

$$\omega = \sqrt{\omega_P^2 + k^2c^2}. \tag{1.14}$$

This is called Bulk Plasmon Dispersion and corresponding curve is plotted in Figure 1.5 in red color. It's usually called 'upper branch', since it's located above surface plasmons' dispersion curve that will be derived in the next section. [9]

One can find refractive indices of a metal by using dielectric components and its magnitude $|\epsilon| = \sqrt{\epsilon_r^2 + \epsilon_i^2}$ as below:

$$n = \sqrt{\frac{|\epsilon| + \epsilon_r}{2}}, \tag{1.15}$$

$$\kappa = \sqrt{\frac{|\epsilon| - \epsilon_r}{2}}. \tag{1.16}$$

where n and κ are the real and imaginary parts of metal's refractive index respectively, so the general refractive index can be written as $N = n + i\kappa$.

1.1.2 Dispersion Relation for SPPs

Let's derive dispersion curve of surface plasmon polaritons and for doing so we start with their definition. These are collective oscillation of electron density on the surface. Wherever higher density of free electrons is created for any reason, they must have left some positive regions behind in their neighbourhood. So one can imagine a simple model of metal's surface under SPPs, next to a dielectric substance as figure 1.2 with that particular coordinates of in-plane x and z, and inward y axis. This choice of wave propagation means,

$$E_y = 0, \qquad \& \qquad H_x = H_z = 0.$$

The fields inside the two materials are expressed as the following (First index shows direction of the field, and second one indicates whether its in metal (m) or dielectric (d)):

$$\textbf{Dielectric} : \begin{cases} \mathbf{H_d} = (0, H_{yd}, 0)e^{i(k_{xd}x + k_{zd}z - \omega t)} \\ \mathbf{E_d} = (E_{xd}, 0, E_{zd})e^{i(k_{xd}x + k_{zd}z - \omega t)} \end{cases} \tag{1.17}$$

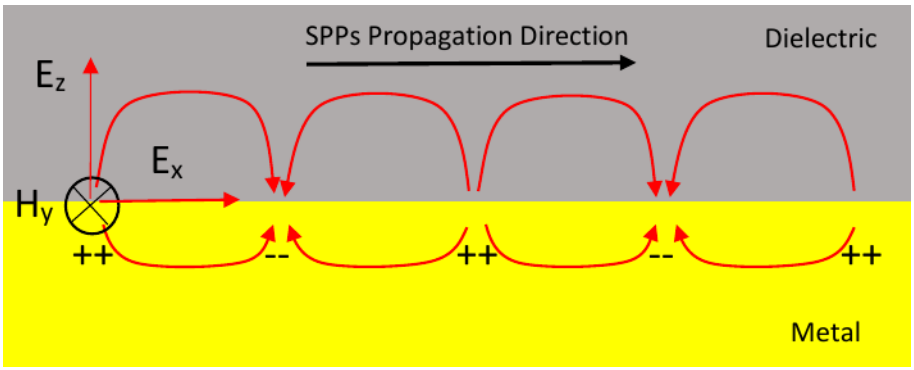

Figure 1.2. Electric field lines caused by SPPs on the metal-dielectric interface.

and

$$\textbf{Metal}: \begin{cases} \mathbf{H_m} = (0, H_{ym}, 0)e^{i(k_{xm}x - k_{zm}z - \omega t)} \\ \mathbf{E_m} = (E_{xm}, 0, E_{zm})e^{i(k_{xm}x - k_{zd}z - \omega t)} \end{cases} \tag{1.18}$$

ω is the frequency of the SPPs oscillations and k's are their wavevector components. Now we can apply boundary conditions for electric and magnetic fields (defining $\overrightarrow{n}_{md}$ as the normal vector from metal to dielectric and assuming zero net charge and current on the surface),

$$(\mathbf{D_d} - \mathbf{D_m}).\overrightarrow{n}_{md} = \sigma = 0 \quad \Rightarrow \quad \epsilon_m E_{zm} = \epsilon_d E_{zd}. \tag{1.19}$$

while,

$$\begin{cases} \overrightarrow{n}_{md} \times (\mathbf{E_d} - \mathbf{E_m}) = 0 \rightarrow E_{xm} = E_{xd} \\ \overrightarrow{n}_{md} \times (\mathbf{H_d} - \mathbf{H_m}) = 0 \rightarrow H_{ym} = H_{yd} \end{cases} \Rightarrow k_{xm} = k_{xd}. \tag{1.20}$$

The other Maxwell's equation: $\nabla \times \mathbf{H} = \frac{\epsilon}{c}\frac{\partial}{\partial t}\mathbf{E}$, in both metal and dielectric, can provide us valuable information,

$$\begin{bmatrix} \partial_x \\ \partial_y \\ \partial_z \end{bmatrix} \times \begin{bmatrix} 0 \\ \mathbf{H}_y \\ 0 \end{bmatrix} = \frac{\epsilon}{c}\partial_t \begin{bmatrix} \mathbf{E}_x \\ 0 \\ \mathbf{E}_z \end{bmatrix},$$

which leads to

$$\begin{bmatrix} -\partial_z \mathbf{H}_y \\ 0 \\ \partial_x \mathbf{H}_y \end{bmatrix} = -i\epsilon\frac{\omega}{c}\begin{bmatrix} \mathbf{E}_x \\ 0 \\ \mathbf{E}_z \end{bmatrix}. \tag{1.21}$$

$\mathbf{H}_y, \mathbf{E}_x$, and $\mathbf{E}_z$ in addition to magnitude in specified directions, have a phase which differs from metal to dielectric. For example $\mathbf{E}_{zm} = E_{zm}e^{i(k_{xm}x - k_{zm}z - \omega t)}$ and $\mathbf{E}_{zd} = E_{zd}e^{i(k_{xd}x + k_{zm}z - \omega t)}$ (see Equations 1.17 and 1.18). Equation 1.21 can be decomposed into two components, in x and z directions, and taking derivatives results

$$x: \begin{cases} \textbf{Dielectric}: \quad k_{zd}H_{yd} = +\epsilon_d\frac{\omega}{c}E_{xd}, \\ \textbf{Metal} \qquad : k_{zm}H_{ym} = -\epsilon_m\frac{\omega}{c}E_{xm}, \end{cases} \quad z: \begin{cases} \textbf{Dielectric}: \quad k_{xd}H_{yd} = -\epsilon_d\frac{\omega}{c}E_{zd}, \\ \textbf{Metal} \qquad : k_{xm}H_{ym} = +\epsilon_m\frac{\omega}{c}E_{zm}. \end{cases} \tag{1.22}$$

Let's focus on just the x component for now, and divide each sides of the two equations by each other,

$$\frac{k_{zm}}{k_{zd}}\frac{H_{ym}}{H_{yd}} = -\frac{\epsilon_m}{\epsilon_d}\frac{E_{xm}}{E_{xd}}. \tag{1.23}$$

Using above equation and boundary conditions given at Equation 1.20, we are left with a key relation in deriving SPPs dispersion curve:

$$\frac{k_{zm}}{k_{zd}} = -\frac{\epsilon_m}{\epsilon_d} \qquad \Longleftrightarrow \qquad \frac{k_{zd}}{\epsilon_d} + \frac{k_{zm}}{\epsilon_m} = 0. \tag{1.24}$$

The magnitude of any three dimensional wavevector is given by $k_x^2 + k_y^2 + k_z^2 = k^2 = \epsilon\frac{\omega^2}{c^2}$. In our case $k_y = 0$ and k_x is the same for metal and dielectric on the surface. So then

$$\begin{cases} \textbf{Dielectric}: \qquad k_x^2 + k_{zd}^2 = \epsilon_d\frac{\omega^2}{c^2}, \\ \textbf{Metal}: \qquad k_x^2 + k_{zm}^2 = \epsilon_m\frac{\omega^2}{c^2}. \end{cases} \tag{1.25}$$

Plugging in 1.24 into 1.25, leads to the long-awaited SPPs dispersion relation (Equation 1.26), and also two evanescent waves in z direction (Equations 1.27& 1.28),

$$k_x = \frac{\omega}{c}\sqrt{\frac{\epsilon_d \epsilon_m}{\epsilon_d + \epsilon_m}}, \tag{1.26}$$

and

$$k_{zd} = \frac{\omega}{c}\frac{\epsilon_d}{\sqrt{\epsilon_m + \epsilon_d}}, \tag{1.27}$$

$$k_{zm} = \frac{\omega}{c}\frac{\epsilon_m}{\sqrt{\epsilon_m + \epsilon_d}}. \tag{1.28}$$

Considering the fact that ϵ_m is frequency dependent and it can be positive or negative based on how the frequency is compared to ω_P, the left side of equation 1.26 can be a negative number and hence we'd have an imaginary wavevector in x-direction, which corresponds to a damping wave. In order to avoid this, we need to satisfy the conditions of $|\epsilon_m| >> \epsilon_d$, while $\epsilon_d \geq 1$ and $\epsilon_m < 0$. With these expectations met, both numerator and denominator are negative and the ratio remains a positive number. For a metal like silver this happens if $0 \lesssim \omega \lesssim 0.4\,\omega_P$, see Figure 1.1. Ideally, these surface waves can travel infinitely in x direction; but if the damping factor γ, is taken into account, then SPPs lose their amplitude after tens or hundreds of oscillations (order of ten or hundred μm), depending on their frequency and value of γ; since there will be a factor of $e^{-\mathbf{Im}(k_x)x}$ multiplied by the oscillatory term.

Equations 1.27 and 1.28 which represent wavevectors in z direction and under above mentioned conditions, both are imaginary and it makes their waves exponentially damping or evanescent. The decay length in dielectric is in order of 100 nm and given by:

$$\delta_d = \frac{1}{|k_{zd}|}, \tag{1.29}$$

and in metal is in order of 10 nm and given by

$$\delta_m = \frac{1}{|k_{zm}|}. \tag{1.30}$$

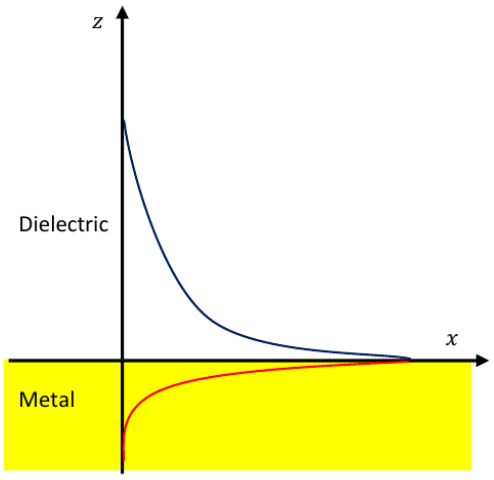

Figure 1.3. Evanescent fields spreading into dielectric (blue arrow) and metal (red arrow).

We see that $\delta_d >> \delta_m$, which is predictable from the condition $|\epsilon_m| >> \epsilon_d \geq 1$ and Equation 1.24. Since $\mathbf{E}_z$ and $\mathbf{E}_x$, have k_z in their phase term, both will decay like Fig. 1.3, in z direction. In Equation 1.22, dividing dielectric terms, and doing simplifications, provide,

$$E_{zd} = -i\sqrt{\frac{|\epsilon_m|}{\epsilon_d}}E_x, \tag{1.31}$$

that means $\mathbf{E}_{zd}$ is stronger in magnitude, compared to $\mathbf{E}_x$, anywhere including near the surface of metal and they are in $\pi/2$ phase shift (see Figure 1.4). In nano-scale vicinity of the interface, the combination of these fields happens to be very high, and interesting effects can be observed if we put some quantum dots on the surface.

What if we work on frequencies higher than ω_P, in which $\epsilon_m > 0$? The answer is, in that regime, the source of oscillations, typically light, can penetrate inside the metal and cause bulk plasmons, rather than surface plasmons, as was discussed earlier.

In $0.1\,\omega_P \lesssim \omega \lesssim 0.4\,\omega_P$ region of frequency, by a good approximation the metal dielectric constant is given as

$$\epsilon_m \simeq \epsilon_r \simeq 1 - \omega_P^2/\omega^2. \tag{1.32}$$

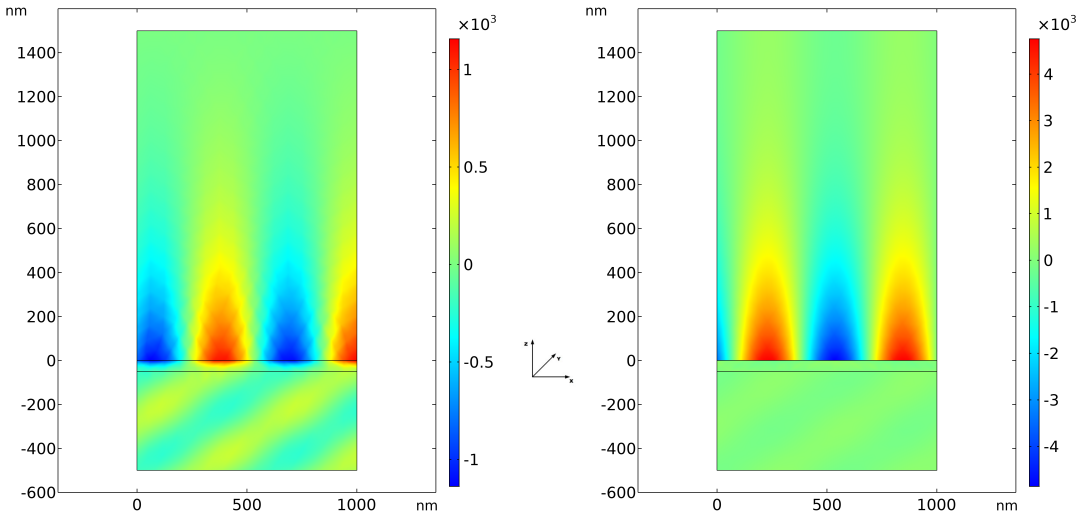

Figure 1.4. E-Fields in air created by SPPs located at ($z = 0$) on Silver film, in x (left Fig.) and z (right Fig.) directions. Silver is coated on a substrate and is adjacent to air on top.

substituting equation 1.32 into equation 1.26 leads to:

$$\omega^2 = \frac{\omega_P^2}{2} + \frac{\epsilon_d + 1}{2\epsilon_d} k^2 c^2 \pm \sqrt{\frac{1}{4\epsilon_d^2}((\epsilon_d \omega_P^2 + (\epsilon_d + 1)k^2c^2)^2 - 4\epsilon_d \omega_P^2 k^2 c^2)}. \tag{1.33}$$

So we got two answers. The one with the negative square root, describes SPPs dispersion. The other one is not physical and although its curve looks similar to the bulk plasmons' curve, it has nothing to do with it. In case that $\epsilon_d = 1$, with omitting the nonphysical answer, equation 1.33 is simplified as

$$\omega^2 = \frac{\omega_P^2}{2} + k^2 c^2 - \sqrt{\frac{\omega_P^4}{4} + k^4 c^4}. \tag{1.34}$$

Figure 1.5 shows SPPs dispersion for this specific condition along with the bulk dispersion curve and it's worth reminding that here k is totally in x-direction. If we choose another dielectric with $\epsilon_d > 1$, the curve will distance itself more from the light line. Frequency-wise, bulk plasmons and SPPs, don't overlap and they are generated at different regions. But in those regions, for any value of frequency, a bulk plasmon never gets to the same wavenumber as the light line in free space, and it's always lower than that; while

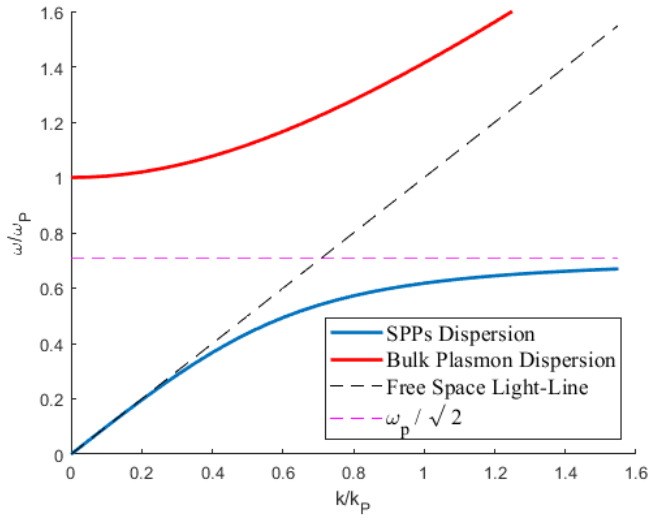

Figure 1.5. Dispersion Curves of Bulk plasmons and SPPs for a metal in contact with air ($k_P = \omega_P/c$).

on the other hand, SPPs always have higher wavenumber compare to the light line. The latter means that we can not produce SPPs using free space light, on its own; since energy-momentum matching condition is not met to excite SPPs. So we need to find a way to somehow boost the light's momentum. The techniques to achieve this are the topic of the next sections.

1.2 SPPs Excitation Methods

There are two main methods to excite SPPs. One is using prism or Attenuated Total Reflection (ATR) and the other is by letting light to go through grating structure. Both of these methods can increase magnitude of wavevector k_x and we will explain each in detail.

1.2.1 Attenuated Total Reflection (ATR)

Depending on the types of material they are made of, prisms can have high refractive indices as much as ~ 2. As the light passes through a dielectric material with refractive

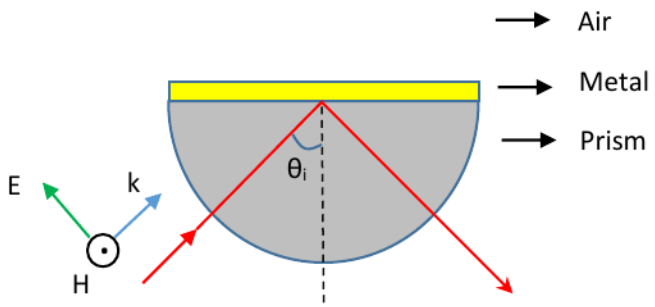

Figure 1.6. A p-polarized laser beam hitting the base of prism with incidence angle θ_i.

index n, its speed decreases from c to $v = c/n$ and its wavelength from λ_0 to $\lambda = \lambda_0/n$. Frequency of the light, $f = v/\lambda$, remains the same in this transition, so wavelength needs to decrease with the same ration. This is good news, since we know $k = 2\pi/\lambda$, and smaller lambda means higher wavevector or momentum ($p = \hbar k$), while the frequency or energy is intact ($E = \hbar\omega$).

Assume we have a hemispherical prism with refractive index of n, coated with a thin layer of metal on its base. A beam of monochromatic p-polarized laser comes and hits the base of it from prism side, with incidence angle θ_i with respect to the normal vector of the prism/metal interface. This configuration is known as Kretschmann-Raether geometry, shown in Figure 1.6. The beam is selected as p-polarized, because calculations show later on that s-polarized waves have no contribution in SPPs excitation; they only add to the background (In p-polarization, the light's electric field is parallel to the plane of incidence; while in s-polarization, it's perpendicular). There will be a partial reflected beam coming out, as well as some transmission and absorption. If the incidence angle is greater than critical angle, or $\theta_i > \theta_c$, then we expect the light to be totally reflected and no energy should flow into the metal and dielectric.

Based on the way SPPs behave, light has to have the right momentum component in x-direction, parallel to the metal/air interface in order to excite them. So k_x is the component that we care about here, and inside the prism it's given by

$$k_x = k \sin\theta = \frac{2\pi n}{\lambda} \sin\theta. \tag{1.35}$$

It's easy to guess that we need to put equation 1.35 equal to 1.26, to assure SPPs' needed momentum is provided. The angle that satisfies this condition is called θ_{spr} or Surface Plasmon Resonance (SPR) Angle. It will be clear shortly why this is called a resonance angle.

$$\sin\theta_{spr} = \frac{1}{n}\sqrt{\frac{\epsilon_m \epsilon_d}{\epsilon_m + \epsilon_d}}. \tag{1.36}$$

According to the condition $|\epsilon_m| >> \epsilon_d$, the square root of this ratio is going to be always more than 1; and to be able to see SPPs excitations at relatively low angles or even at any angle, refractive index of prism needs to be high enough; otherwise the right side of equation becomes greater than 1, and results an imaginary θ_{spr}. Also since critical angle for the case of prism and air is given by $\sin\theta_c = \frac{1}{n}$, in comparison with Equation 1.36, conclusion is that $\theta_{spr} > \theta_c$.

Figure 1.7 shows the SPPs dispersion curve for metal adjacent to air, and dispersion lines for light in free space and inside the prism. The angular frequency of a hypothetical laser, $\omega = 0.4\,\omega_P$, is also shown as green dashed line. Depending on the angle that the laser hits the base of prism, its k_x is going to be different. For $\theta_i = 90°$, $k_x = k$ and graphically it lies on the intersection of light line in prism and laser angular frequency. By decreasing θ_i, k_x happens to retreat on the green dashed line, toward the left (e.g. red circle), until it intersects with the SPPs dispersion curve and intersection is shown by red dot, which is where SPR happens. Practically, the visible laser beams have angular frequencies around $0.2\omega_P$ to $0.3\omega_P$, but here we chose $0.4\omega_P$ to avoid zooming in and better graphically present the phenomenon.

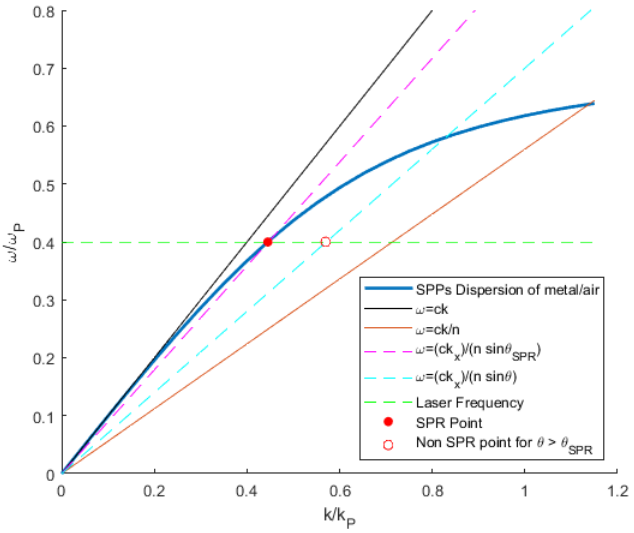

Figure 1.7. SPR point for Prism/Metal/Air structure and $\omega = 0.4\,\omega_P$.

So what happens at θ_{spr}? The laser beam which is supposed to get totally reflected, suddenly transfers all of its energy to SPPs, and a sudden drop of intensity occurs at reflectivity measurement, which shows up as a sharp valley in Reflectance vs. θ_i graph, also known as SPR graph (see Figure 1.8). In ideal situation, i.e. when the film thickness is right, the energy is completely absorbed by the metal, otherwise the SPR peak may not be as expected. Notice that plasmons are created in the metal/air interface; not at prism/metal interface, which is not possible to excite by this method, since its dispersion curve lies to the right side of light line in prism.

There is a very interesting point in Equation 1.36 and it's the sensitivity of θ_{spr} due to the change in ϵ_d. As we raise or lower, even slightly, the amount of ϵ_d, SPPs dispersion curve and consequently the SPR angle will change significantly. This is the whole point for studying SPPs as optical sensors, since SPPs in metals are well entangled with the ambient dielectric material.

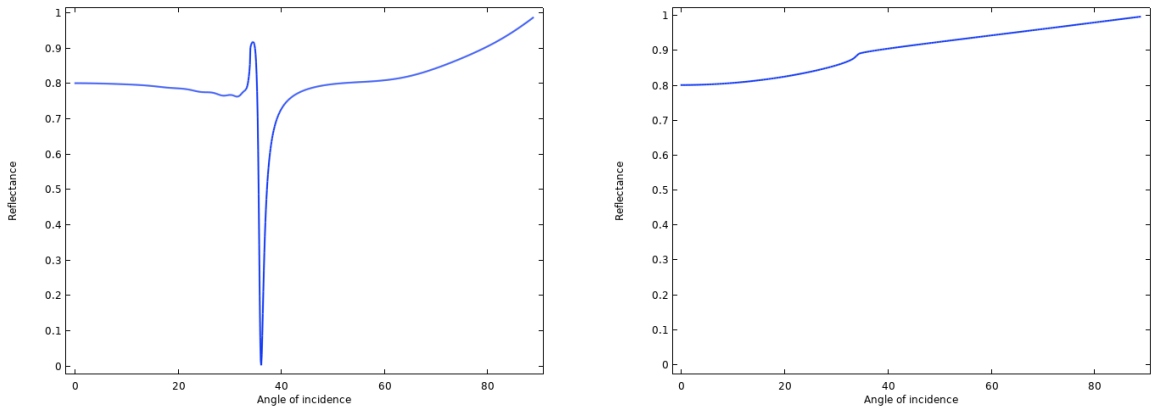

Figure 1.8. Simulated reflectivity for 48nm Au film, using p -polarized (left) & s -polarized (right) waves.

One can find the right thickness of the film, as well as a graph of reflectace vs. angle of incidence, by using Fresnel's coefficients and superposition of the waves, which is what we'll do in the next chapter as we investigate the SPPs excitation in the multi-layer thin films.

1.2.1.1 Reflection and Transmission of Multi-layer Thin Films

When there are more than one layer of material (either metal or dielectric) deposited on top of prism, figuring out the dispersion curve is not that simple. But for experimental reasons, what we are actually more interested in, is having SPR curve, which is relatively easier to obtain by the approach of Fresnel's coefficients and wave superposition.

We're going to first see what these coefficients are for the simple case of two materials with refractive indices of n_1 and n_2. An elliptically polarized light wave (containing both p- and s-polarized waves) is emitted and hits the boundary and gets both reflected and transmitted according to the Figure 1.9.

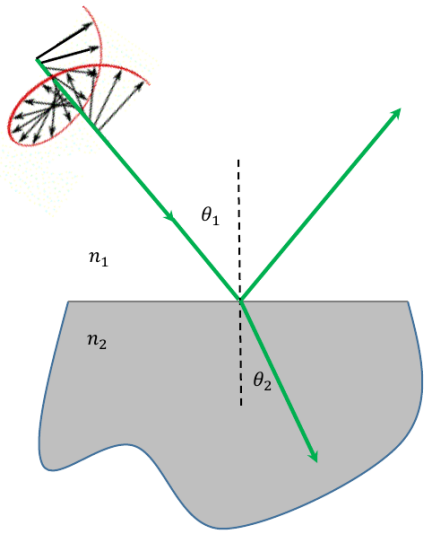

Figure 1.9. Elliptic polarized wave, reflected and transmitted at media interface.

The reflectance $R = |r|^2$ and transmittance $T = \frac{n_2 \cos\theta_2}{n_1 \cos\theta_1}|t|^2$ are not the same for s- and p-polarizations and the amplitudes r & t are given as

$$\begin{cases} r_p = \dfrac{n_2 \cos\theta_1 - n_1 \cos\theta_2}{n_2 \cos\theta_1 + n_1 \cos\theta_2}, \\ t_p = \dfrac{2n_1 \cos\theta_1}{n_2 \cos\theta_1 + n_1 \cos\theta_2}, \end{cases} \qquad \begin{cases} r_s = \dfrac{n_1 \cos\theta_1 - n_2 \cos\theta_2}{n_1 \cos\theta_1 + n_2 \cos\theta_2}, \\ t_s = \dfrac{2n_1 \cos\theta_1}{n_1 \cos\theta_1 + n_2 \cos\theta_2}. \end{cases} \tag{1.37}$$

r and s indices refer to the polarization types. In general the reflected and transmitted beams will have also elliptical polarization, but under special case of angle (Brewster's Angle, $\theta_B = \tan^{-1}(n_2/n_1)$) the reflection is only s-polarized. If the beam was totally p-polarized, there wouldn't be any light reflected at this angle. In addition to production of s-polarized wave, this can be used as a test to check whether our beam is 100% p-polarized, by having no reflection at all, and we applied this method in our lab as well, to make sure our beam is p-polarized.

We are now able to include the case of one (or more) layer of material between two semi-infinite media. See Figure 1.10. On each interface, there will be a reflection and transmission (and absorption if refractive index of the film is a complex number), but

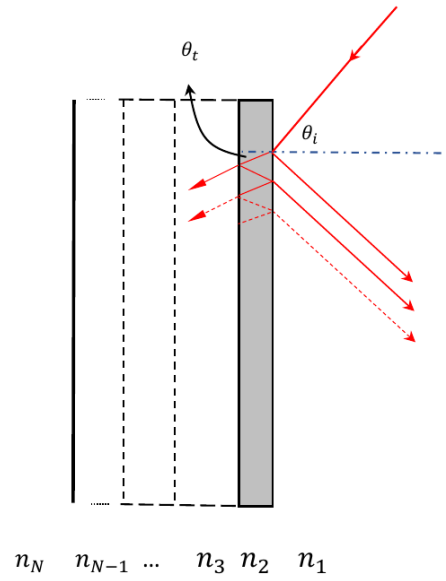

Figure 1.10. Light interference in a stack of thin films, with different refractive indices .

reflection from each end, contains the wave inside the film for a while; and although in principle, this process goes on to the end of the film's length, the intensity drops to almost zero after a few reflections. Let's concentrate first on single layer case only, with real n_2 and $n_1 = n_3$. For p polarized wave or when the E-field is in-plane of incidence, $180°$ phase shift occurs at each internal reflection inside the film. Depending on the thickness of the film, its dielectric constant, and the angle of transmittance, which contribute to the optical path in Equation 1.38, superposition of reflection terms can be constructive or destructive.

$$\delta_2 = 2n_2 d\cos\theta_t = \begin{cases} m\lambda & \Rightarrow \textbf{destructive} \quad E_{0r} = 0, \\ (m+1/2)\lambda & \Rightarrow \textbf{constructive} \quad E_{0r} = \frac{2r}{1+r^2}E_0. \end{cases} \tag{1.38}$$

In above equation, assuming λ_0 is the free space wavelength of the light, then $\lambda = \lambda_0/n_1$ is the wavelength at the first medium. Also m is a positive integer, E_0 is the original beam's electric field, and E_{0r} is the total reflected beam's electric field. Total reflectance is given by $R = \left|\frac{E_{0r}}{E_0}\right|^2$.

When $\delta_2 = m\lambda$, all the following reflections off the surface of the film, are 180° out-of-phase with respect to the original reflection. Adding all these reflection terms, leads to a geometrical series that becomes zero, if we use the identities,

$$r = -r', \qquad \& \qquad tt' - rr' = 1. \tag{1.39}$$

where primed quantities represent reflection inside the film and transmission to the outside of the film. This terminology is true even if $n_1 \neq n_3$, when both are still lower or greater than n_2. For s-polarized waves this is not the case and they are not able to interfere destructively, as we've seen already in Figure 1.8. This is the reason for including polarizer in the setup and only work with p-polarized light.

The significance of Equation 1.38 is that it enables us to determine the thickness of the film, d, which provides the least reflection and the most absorption or energy transfer to SPPs, for particular θ_t; while θ_t is related to SPR angle by $n_1 \sin\theta_{spr} = n_2 \sin\theta_t$ (Snell's law).

Restricting ourselves to $\theta_i \simeq 0$, situation would be similar to the quantum mechanical wave scattering in one dimension, for a particle with mass m, passing through a finite square potential well (Figure 1.11).

As wave comes from the vacuum with energy E, and passes over the potential $-V_0$ ($V_0 > 0$), its momentum increases from $k = \sqrt{2mE/\hbar^2}$, to $q = \sqrt{2m(E+V_0)/\hbar^2}$. In Electromagnetic formulation, the ratio of these two is equal to refractive index of the dielectric; so by analogy we can say the quantity $\sqrt{1+V_0/E}$, plays the same rule as n in optics. Deeper potential well corresponds to higher refractive index. Using continuity of the wave and its derivative with respect to position, the reflection and transmission from the well is calculated as [10]

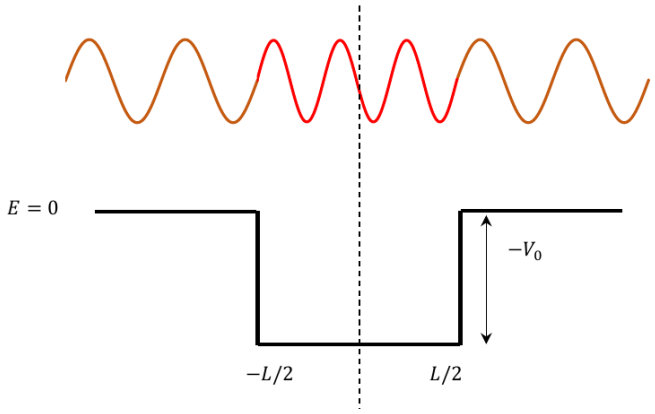

Figure 1.11. Quantum Mechanical wave passing through a square potential well.

$$\begin{cases} R = \frac{(q^2-k^2)^2 \sin^2 qL}{4q^2k^2 \cos^2 qL+(q^2+k^2)^2 \sin^2 qL}, \\ T = \frac{4q^2k^2}{4q^2k^2 \cos^2 qL+(q^2+k^2)^2 \sin^2 qL}. \end{cases} \tag{1.40}$$

when $qL = l\pi$ and $l = 0, 1, 2, ...$, no reflection happens and the wave is totally transmitted; which is in fact the same as first condition in Equation 1.38, when $\theta_t \simeq 0$ and $q = 2\pi n/\lambda$. We can generalize this analysis also for the case of $n_1 \neq n_3$, $\theta_i \not\simeq 0$, and film being metallic. The difference is in the potential, which becomes complex, mostly imaginary, and much stronger than E, for frequencies less than ω_P.

Moreover, because of free electron oscillations, the continuity of the electric fields and their derivatives don't necessarily apply here. Wave amplitude inside the metal decays and we need to include absorption as well, causing transmitted wave to have very smaller magnitude, away from the SPR angle. Surrounding SPR angle, even though the electric field caused by SPPs is evanescent, its initial magnitude is much higher than laser electric field.

Having multilayer films instead of one, makes the analysis more complicated, since there are reflection and transmission terms coming backwards from the adjacent films in the row, which need to be included. It's easier to call the amplitude of all the waves that

are going to the left of the n-th film, as v_n and those to the right as w_n and evaluate them as, [11]

$$\begin{cases} v_{n+1} = e^{i\delta_n} v_n t_{n,n+1} + w_{n+1} r_{n+1,n}, \\ e^{-i\delta_n} w_n = w_{n+1} t_{n+1,n} + e^{i\delta_n} v_n r_{n,n+1}. \end{cases} \tag{1.41}$$

$r_{n,n+1}$ and $t_{n,n+1}$ are reflection and transmission of the light coming from layer n and going to the layer $n+1$, and δ_n is the phase shift caused by layer n. Using identities of Equation 1.39, for the films we get

$$\begin{pmatrix} v_n \\ w_n \end{pmatrix} = M_n \begin{pmatrix} v_{n+1} \\ w_{n+1} \end{pmatrix}, \tag{1.42}$$

where,

$$M_n = \begin{pmatrix} e^{-i\delta_n} & 0 \\ 0 & e^{i\delta_n} \end{pmatrix} \begin{pmatrix} 1 & r_{n,n+1} \\ r_{n,n+1} & 1 \end{pmatrix} \frac{1}{t_{n,n+1}}. \tag{1.43}$$

As the light goes through each film, another one of these matrices gets multiplied. we are interested in calculating reflection by the initial film and transmission from the last film. Calling the amplitudes r and t, while having normalized original amplitude, we get

$$\begin{pmatrix} 1 \\ r \end{pmatrix} = \tilde{M} \begin{pmatrix} t \\ 0 \end{pmatrix}, \tag{1.44}$$

in which

$$\tilde{M} = \frac{1}{t_{1,2}} \begin{pmatrix} 1 & r_{1,2} \\ r_{1,2} & 1 \end{pmatrix} M_2 M_3 ... M_{N-1}, \tag{1.45}$$

and obviously is a 2×2 matrix and one can find r and t by,

$$t = \frac{1}{\tilde{M}_{11}}, \qquad \& \qquad r = \frac{\tilde{M}_{21}}{\tilde{M}_{11}}. \tag{1.46}$$

These results are still applicable when refractive indices are complex numbers. R is already real, and if we filter real part of T, then we use the equation $A = 1 - R - T$,

to get absorption A. One can manipulate all the films' thicknesses here as well to get the highest absorption at SPR angle. If the thicknesses are not optimized, there will be still a diminished signal at SPR angle.

The multilayer sensors that we've made and studies in our group include bi-metallic (e.g. Ag/Au), and bi-metallic waveguide coupled (Ag/Si_3N_4/Au) sensors. The advantage of such a design is that it can combine good properties of each material and give us better performance and durability. One interesting thing that happens specifically in waveguide coupled sensors is that if the waveguide's thickness be higher than wavelength of the laser, there will be several m's that can fulfill destructive condition in wave superposition, so in the SPR graph, we'll see more than one valley that except for one, others do not correspond to SPPs excitations, and are just heat loss inside the metal.

1.2.2 Grating

Another approach for excitation of SPPs, is using gratings. Assume we have a substrate that its surface is cut like a square-wave, as in Figure 1.12. The periodicity is Λ, and the height h is much smaller than Λ. A ray of light coming from medium in above, gets into this structure, while its amplitude, acquires the same periodicity as Λ. This is the general behaviour of light in periodic structures.

Fourier series enables us to approximate this square wave with sine and cosine waves to whatever order we desire. Working with these terms turns out to be simpler in analysis. For example, to the first order, Fourier series is going to be a simple cosine wave with specified amplitude. The dielectric function then, along the x-direction is

$$\epsilon(r) = \epsilon_{avg} + \Delta\epsilon \cos(\mathbf{K}.\mathbf{r}), \tag{1.47}$$

where $|K| = \frac{2\pi}{\Lambda}$. Now, incorporating these terms into the amplitude of the wave, and Taylor expansion leads to,

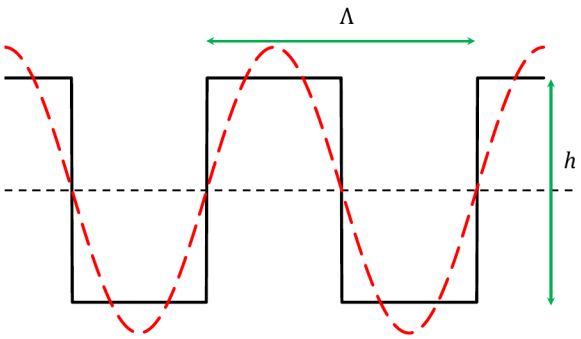

Figure 1.12. Periodic structure like a square-wave, with periodicity of Λ and the height of h; along with its first order Fourier series.

$$\mathbf{E}(\mathbf{r}) = A(\epsilon)e^{-i\mathbf{K_i}.\mathbf{r}} \tag{1.48}$$

$$First\ order \rightarrow \simeq \alpha e^{-i\mathbf{K_i}.\mathbf{r}} + \beta e^{-i(\mathbf{K_i}-\mathbf{K}).\mathbf{r}} + \beta e^{-i(\mathbf{K_i}+\mathbf{K}).\mathbf{r}} \tag{1.49}$$

$$m'th\ order \rightarrow \simeq \alpha_m e^{-i\mathbf{K_i}.\mathbf{r}} + \beta_m e^{-i(\mathbf{K_i}-m\mathbf{K}).\mathbf{r}} + \beta_m e^{-i(\mathbf{K_i}+m\mathbf{K}).\mathbf{r}} \tag{1.50}$$

Where α's and β's are some constants, and $\mathbf{K_i}$ is the wavevector of the incoming light. We got three therms with different wavevectors, $\mathbf{K_i}$, $\mathbf{K_i} + m\mathbf{K}$, and $\mathbf{K_i} - m\mathbf{K}$, that will appear in the reflection and transmission regions. So we were able to change the wavevector by $m\mathbf{K}$, in which $m = 0, 1, 2, ...$ For the m'th order, the angle of reflection θ_r and transmission θ_t, depend on the refractive indices of their media, n_r and n_t respectively, and are given by

$$\begin{cases} n_r \sin\theta_{r,m} = n_i \sin\theta_i + m\frac{\lambda}{\Lambda}, \\ n_t \sin\theta_{t,m} = n_i \sin\theta_i + m\frac{\lambda}{\Lambda}. \end{cases} \tag{1.51}$$

λ is the wavelength of incoming light. As m increases, angle of reflection and transmission for the associated beams, change a little bit, while their amplitudes will decrease. $\theta_{r,m}$s and $\theta_{t,m}$s are measured with respect to the normal dashed line. Eventually there will be an m, with imaginary $\theta_{r,m}$ and/or $\theta_{t,m}$. It means for that order and above, there won't be a corresponding beam of reflection and/or transmission, but collection of those that are

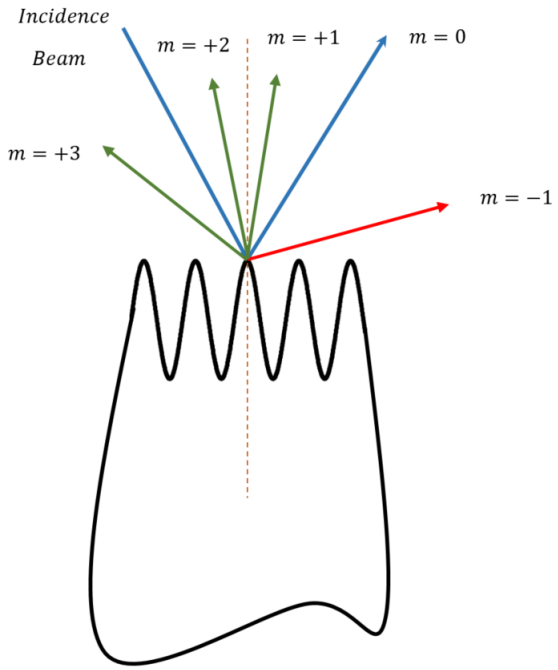

Figure 1.13. Diffraction orders with arbitrary periodicity and wavelength as it's reflected off of a grating structure..

generated, construct a diffraction pattern for both reflection and transmission beams; see figure 1.13. This would happen if there is no other effect included, but if the substrate is coated with a metal film, then things may not be the same.

Recalling from SPPs dispersion derivation, we need certain momentum in x- direction, Equation 1.26, to excite plasmons. This can be achieved by choosing appropriate value of Λ. The strongest effect can be seen in either reflection or transmission region, for $m = 1$, if there is a real θ_i that can fulfill this equation:

$$n_i \sin\theta_i + \frac{\lambda}{\Lambda} = \sqrt{\frac{\epsilon_m \epsilon_d}{\epsilon_m + \epsilon_d}}, \tag{1.52}$$

or for $m = -1$ using:

$$n_i \sin\theta_i - \frac{\lambda}{\Lambda} = -\sqrt{\frac{\epsilon_m \epsilon_d}{\epsilon_m + \epsilon_d}}. \tag{1.53}$$

Under this constraint, we'll observe a missing diffraction spot for the orders of $m = \pm 1, ..$, and it means its energy is consumed for excitation of SPPs which continue to oscillate on the surface even beyond the grating structure.

2

Fabrication of Thin Films and Nano-structures

Three main deposition techniques to grow thin films on a substrate are as the following, although we just used the last one in this research. [12, 13]

- Electro-Chemical Deposition
  - Used for example in copper deposition.
- Chemical Vapor Deposition (CVD)

  - Certain chemical reaction that happens on the surface of substrate, leads to a film deposition. Refractory metals, such as Tungsten are easier to deposit using CVD due their high melting temperature.

- Physical Vapor Deposition (PVD)

  This technique mainly includes:

  - Thermal Evaporation
  - Sputtering

Depending on the purpose of deposition and characteristics of the material, whether it's an element or alloy, there is a preferred technique among above mentioned methods, which provides a better film quality of that material. To evaluate quality of the film, several factors come into account, such as uniformity and accuracy of the thickness, defects and impurities, electrical and mechanical properties, and in case that the substrate is periodic, we may want to have a certain step coverage.

There are also highly accurate techniques like SEM, TEM and AFM that can probe the surface to various scales and depict the quality of the film and tell us whether it's a good fit for the application we have in mind.

2.1 Thermal Evaporation

This technique was used extensively in the past, but today its application is more limited to academic purposes, since it's a relatively cheap and fast process. It operates using a closed chamber in vacuum condition ($\sim 10^{-6} - 10^{-7}$ Torr) and is commonly used for metal deposition, but certain dielectrics as well. As the name implies, material that is supposed to get evaporated (and is called "Charge"), is located in a crucible, at the bottom of chamber, and warmed up until it melts. Liquids evaporate at any temperature, so we'll have some gaseous phase of the charge inside the chamber, moving in all directions. Having a

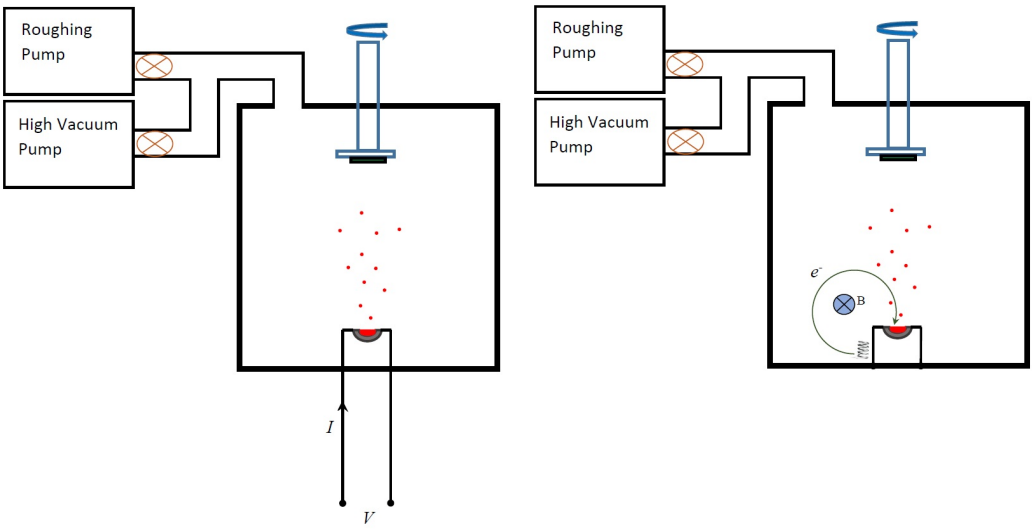

Figure 2.1. Schematics of Thermal Evaporation Machine using electric current (Left) and E-Beam Machine (Right).

cold substrate at designated positions, vapor can easily stick to it, due to the fact that vapor is very reactive. Each crucible is equipped with a shutter, so When the film's thickness is reached to the desired value, the vapor's way out to the chamber can be blocked.

Based on the heating method, Thermal Evaporation devices are categorized into different branches (Figure 2.1 shows the general structure of these devices):

1. Applying high current through the crucible.
    - Problem with method is that if the melting point of the charge is very high, like in Tungsten, crucible will sublimate and leads to impurities of the film.
2. E-beam evaporation, A filament is heated up until it emits electrons. The resulting electrons are guided by a magnetic field to bombard the surface of material and increase its temperature.
    - It produces small amount of X-rays and secondary electrons, but usually they don't have the ability to change the structure of the film.

2.1.1 Deposition Control

Temperature of material is a decisive factor in deposition rate, and meanwhile it's difficult to control. So we can't be sure what the thickness of the film is at each stage and how fast it's growing, just by monitoring the amount of current or energy transferred through the material. On the other hand we can measure the thickness of the film, at real time, using quartz crystals. These minerals vibrate at certain frequency, which is subject to change if we apply even tiny (atomic scale) amount of mass on it. Having the thin film gravity in touch with the crystal, provides us an ultrahigh accuracy tool to measure the thickness of the film.

In some designs, the substrate holder can rotate around its axis at some frequency, like 50 rounds/min or so, in order to achieve a more uniform film and provide the same growth condition for all angles or directions.

2.1.2 Chamber's Pressure

There are reasons for providing vacuum condition in Thermal Evaporation method. Air contains oxygen, which is highly explosive and also reactive with hot vaporized material. Thus for safety issues we need to bring down the pressure so much that the probability of such an interaction becomes very low. The other reason is that some oxygen or nitrogen molecules can get trapped in the film's structure and contaminate it. Moreover excessive air increases the chance of collision with vapor (lowering Mean Free Path, λ, for the vapor), and deposition rate drops down. λ is given by:

$$\lambda = \frac{kT}{\sqrt{2}\pi P d^2}$$

in which k is Boltzmann constant, T is the chamber's absolute temperature, P is its pressure in Pascal, and d is the diameter of vapor molecule in meters.

Rough calculation shows in order to get $\lambda > 1$ meter, we need to provide and maintain at least 10^{-6} Torr vacuum pressure inside the chamber. Vacuum pumps operate at different pressure ranges and we require two different types of pumps. At first we should run Roughing Pump, which can bring down pressure to $\sim 10^{-3}$. Now we are in the operating range of High Vacuum Pumps (including Turbo-molecular and diffusion), to bring it down to the desired value of $\sim 10^{-6}$ or $\sim 10^{-7}$ Torr. At this condition, while assuming the chamber's temperate is around $300°\mathbf{K}$, λ could be as much as several tens of meters for typical metallic elements.

The regular chamber's dimensions used in our facility is at the order of one meter, so almost for certain, vapor can travel straight inside the chamber without any collision, although it still diffuses over a large area. This can cause non-uniformity in the film's thickness but If the dimension of our substrate is much smaller than the distance between the charge and substrate, then the resulting film will be uniform to a high percentage.

2.2 Sputtering

This technique doesn't have problems we encounter with Thermal Evaporation. General schematics is shown in Figure 2.2. It contains two parallel plates, with some potential difference. Cathode is the target and substrate is connected to Anode. Both plates are cooled during the process. Vacuum condition is provided also here, but later we add an inert gas (usually Argon with pressure of ~ 0.1 Torr) to the chamber. Inert gasses are chemically neutral so we are sure that only physical interactions will happen. Argon atom is relatively abundant, heavy, and non-radioactive, which makes it a better candidate over the other inert gases.

Ar gas gets ionized inside the chamber in the presence of enough strong electric field, and induces a kind of plasma called Glow Discharge, see section 2.2.2. Then Ar^+

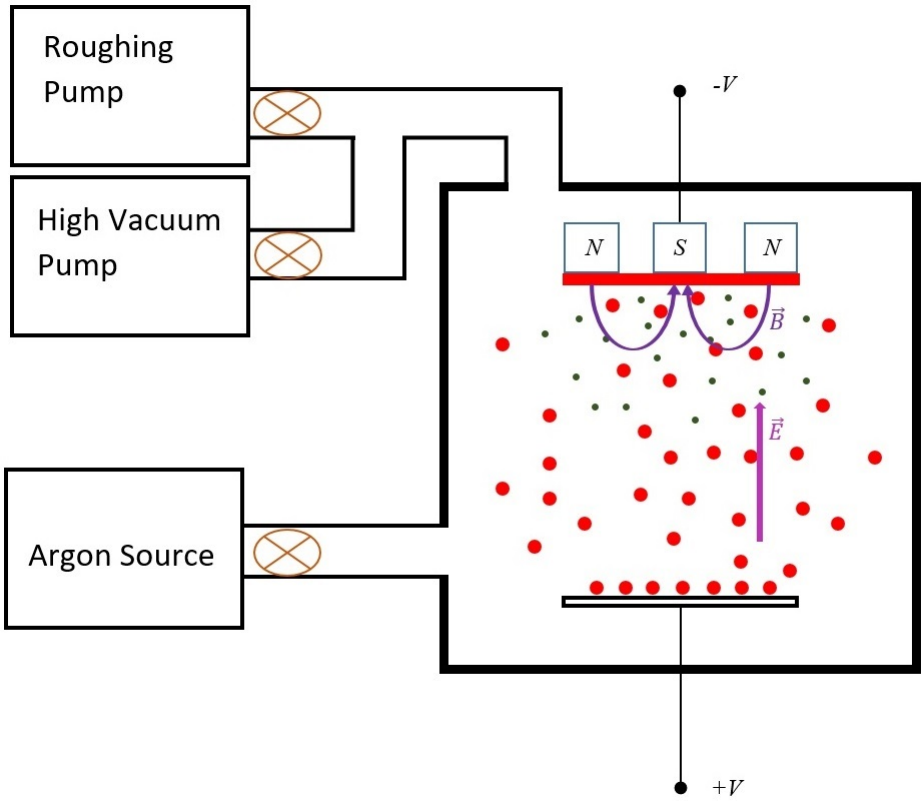

Figure 2.2. Schematics of Sputtering technique. Ar^+ plasma (green dots) hit the substrate (red slab) in helix motion due to EM Fields and release its molecules (red circles).

accelerates toward the target and smashes into it, while transferring its kinetic energy to neighboring molecules in the top layer. These molecules may now be capable of overcoming the inter-molecular forces and leave the target. If so then they get diffused in all directions due to the presence of Argon gas, but those that reach the substrate will stick to it and grow a film. Meanwhile secondary electrons are generated by Ar^+- cathode collisions that are crucial for maintaining steady plasma.

With Argon pressure of 0.1 Torr, Mean Free Path will be in millimeter scale, and sputtered atoms experience lots of collisions before ending up on the substrate. They also come at all direction due to random nature of impacts. Specially for the case that the

substrate has periodic steps, this feature of sputtering can provide pretty good uniformity of film all over the surface.

2.2.1 Sputter Yield

Adding more Argon gas can increase the rate of sputtering off the target, but meanwhile, λ decreases which makes deposition slower. Deposition rate is also affected by the energy of the Argon ions as they hit the target. Let's assume that the number of ions that collide with the target at each second, is N_i, and the number of molecules that are taken off the target, is N_s. In general we can define a factor called "Sputter Yield" as: $\mathbf{Y} = N_s/N_i$.

If the energy of ions that hit the target is less than some threshold, which depends on properties of target and is typically tens of eV, then no target atom is sputtered and $\mathbf{Y} = 0$. On the other hand, if the ion's energy is more than enough, like tens of keV, we'll get implantation instead of sputtering. Ideal value for Yield is between 1 and 2.

Deposition rate is multiplication of Yield and Flux of Ar^+ that collide with the target. One way to increase the flux, without adding to the Argon pressure, is to apply a magnetic field, perpendicular to the E-Field direction. According to Lorentz force, $F = q(E+v\times B)$, resulting electrons from ionization travel through a helix path inside the chamber instead of a relatively straight line. Argon ionization is boosted during this longer trajectory, and it helps to sustain plasma as well.

2.2.2 Glow Discharge

Glow discharge happens between two electrodes when the conditions, like electric potential and gas pressure is right. When it's so, then electrons, which are excited randomly by cosmic rays or an ultraviolet beam in the lab, gain enough energy to ionize the gas molecules/atoms and these positive ions are able to produce secondary electrons, as they hit cathode. This creates a chain reaction. In addition to ionization, excitation and

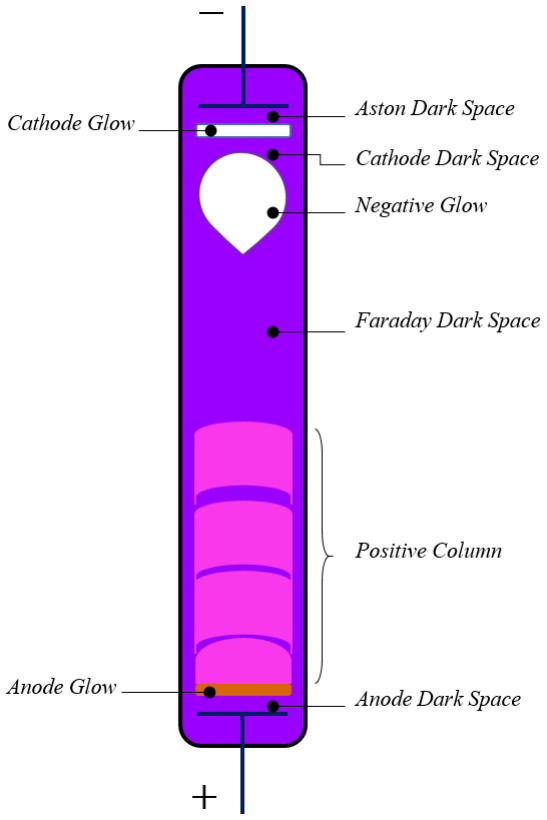

Figure 2.3. Sections of Glow Discharge Tube.

recombination of charged atom and electron happens at some point, which can cause a characteristic visible radiation or glow.

Inert gases are mainly used in this process, as the others may chemically interact with the target. Gas pressure (kept around 1 Torr) is also important because it determines the mean free path of electrons. Very low mean free path prevents electron from acquiring enough energy after each collision to ionize the next impacting atom. High mean free path on the other hand, means less interactions and plasma production which is the main purpose here.

The area between cathode and anode in glow discharge is divided into three main sections: Cathode Layer, Faraday Dark Space, and Anode Layer, as is shown in Figure 2.3.

- **Cathode Layer** with much higher density of electrons which itself consists of four regions, but the main glow (Negative Glow) happens at the last region. Electrons with low kinetic energy recombine with positive atoms or excite (not ionize) them. What matters in sputtering is not Negative Glow, but Cathode Dark Space, where gas ionization is at peak.
- **Faraday Dark Space** that effectively has no electric field, since the number of free electrons and atoms are balanced and not much light is emitted.
- **Anode Layer** consists mainly of a column of excited atoms due to the collisions with re-energized electrons (Positive Column). The length of this section increases with the length of the glow discharge tube.

2.2.3 NanoFab at UT Arlington

Thin films used in this research were grown in class-100 cleanroom at Shimadzu Institute which is located at UTA's NanoFab building. This cleanroom contains several facilities for film fabrication and characterization, including thermal evaporation machine named as AJA ATC ORION Series, see Figure 2.4, that we used for our noble metal depositions. At the bottom of chamber, there are three boats (crucibles) with a switchable shutter that can allow or prevent vapor of moving upward. Not all boats are necessary to be loaded if we want to simply deposit a film of one single element.

Multiple boats are there to allocate each to particular element, so less cleaning is necessary between deposition runs of different metals and to program the machine such that it knows the name and density of the element assigned to that boat. They can also be utilized in alloy deposition. For this purpose, constituent elements sit inside separate boats and adjustable current going through each one, makes us capable of manipulating the deposition rate for specific element and get desirable percentage of that element in resulting film; but we didn't run any experiment on alloys here.

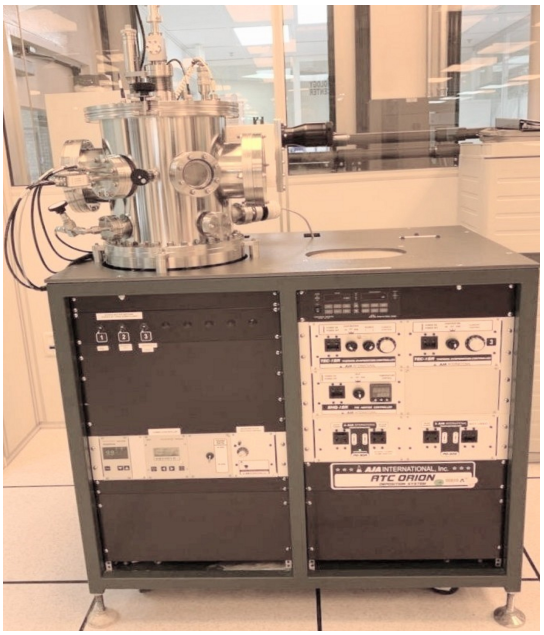

Figure 2.4. Thermal Evaporation Machine.

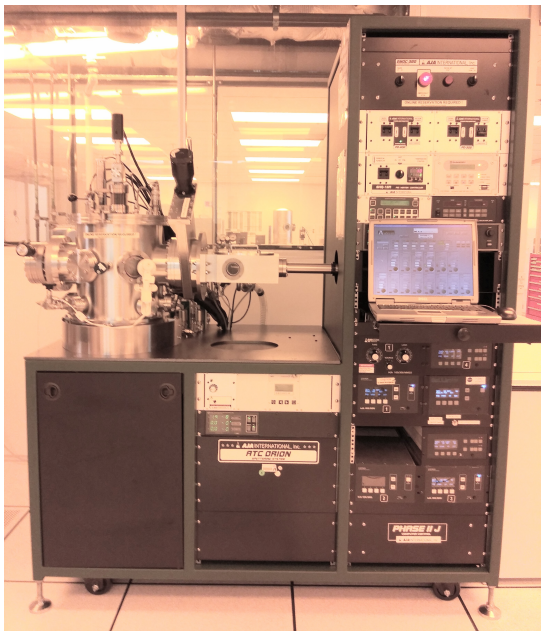

Figure 2.5. Sputtering Machine.

The substrate is loaded on top of the chamber, using some clips screwed to the down side of the lid. We have used SiO_2 and regular glass slides as substrate in our depositions. Then the lid is closed and vacuum pumps start working, until we get to the desired pressure of $\sim 10^{-7}$ Torr. Now the current knob is turned gradually up until we see through the embedded optical window that the metal has started to glow. This is the time to open the shutter, so that the vapor can reach the substrate, which is rotating at the rate of 50 round/minutes during the process to maintain the same geometrical condition for all locations on it and get a uniform film throughout.

The machine should know the exact density and atomic mass of that element, to measure the right thickness of the film, grown on its quartz crystal. If calibrated correctly based on geometrical factors, we can associate the thickness we need on our substrate to the thickness we observe on the monitor for quartz crystal, which is shown in tenth of Angstrom scale. As soon as we get to that point, shutters are closed and current knob is

turned back to zero. After waiting about a minute for the sample to cool down, the job is complete and vacuum valves can be opened.

For dielectric deposition such as Si_3N_4, AJA ATC 5 Orion UHV sputtering machine, see Figure 2.5, is operated. The key part here is to maintain plasma state which was explain in previous section, and to calibrate the machine regularly. To make sure that the calibration here is done correctly, profilometry and ellipsometry is performed on the film, where in the latter the optical properties, like refractive index can also be measured.

2.2.4 Characterization using Ellipsometry, SEM, & TEM

Dielectric materials have almost a fix refractive index with respect to the frequency of the light. But depending on the deposition technique, this value can change considerably. Looking back at the equations 1.37, the ratio of r_p and r_s can be defined as:

$$\rho = \frac{r_p}{r_s} = e^{i\Delta} \tan \Psi$$

in which Ψ and Δ are two new quantities that depend on the refractive indices of the two media. For thin layers it's not as simple as just using Equations 1.37, and interference from consecutive reflections has to be included, see section 1.2.1.1.

What happens in ellipsometry is that both s and p polarized lights with known amplitudes are shone from the air on a film, and reflected light is analyzed to figure out what Ψ and Δ are. Then it uses a model based on e.g. Forouhi-Bloomer dispersion equations, to minimize χ-squared and get the best approximation for refractive index and thickness.

Other advanced techniques like SEM and AFM are implemented to characterize the films. Figure 2.6 shows the quality of one of our silver depositions, with thickness of 50 nm. The sample has been grown in poly-crystal form with occasional obvious spikes, but still to a good extent and for our purposes, it can be considered as a uniform film.

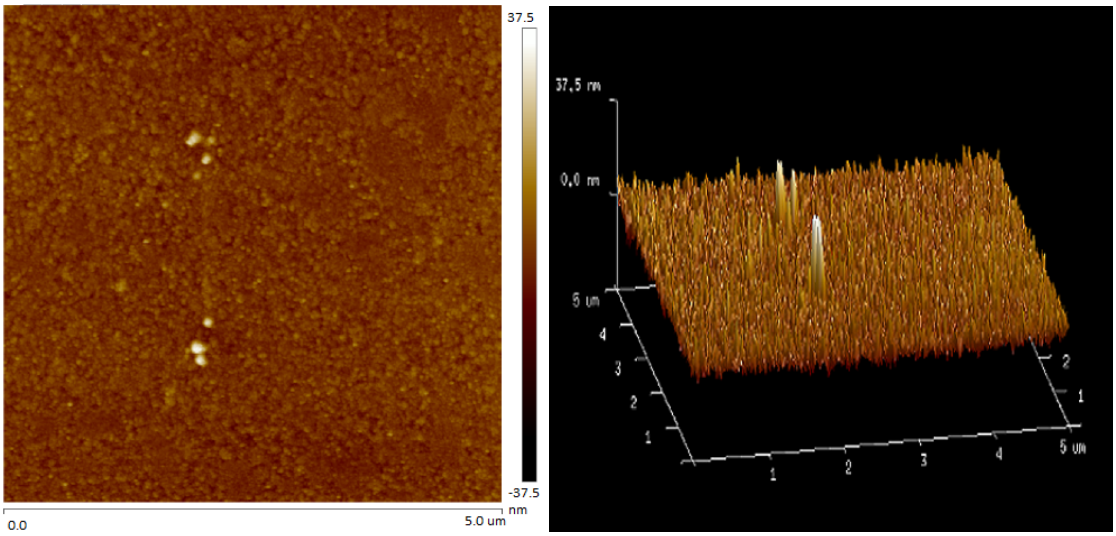

Figure 2.6. Surface topography of a $5\mu m \times 5\mu m$ region of 50 nm silver film using AFM tip in a non-contact mode at a scanning rate of 0.5 Hertz.

Furthermore, an SEM machine, Figure 2.7, is operated to assure the uniformity of the sample in a bigger scale. For example we've shown pictures taken from the same sample above, in Figure 2.8, which shows a polycrystalline surface with average size of 50 nm in diameter. The machine is also capable of taking EDXS or Energy Dispersive X-ray spectroscopy, to ensure that the sample is not contaminated by another element like Oxygen, that can change the property of our films significantly.

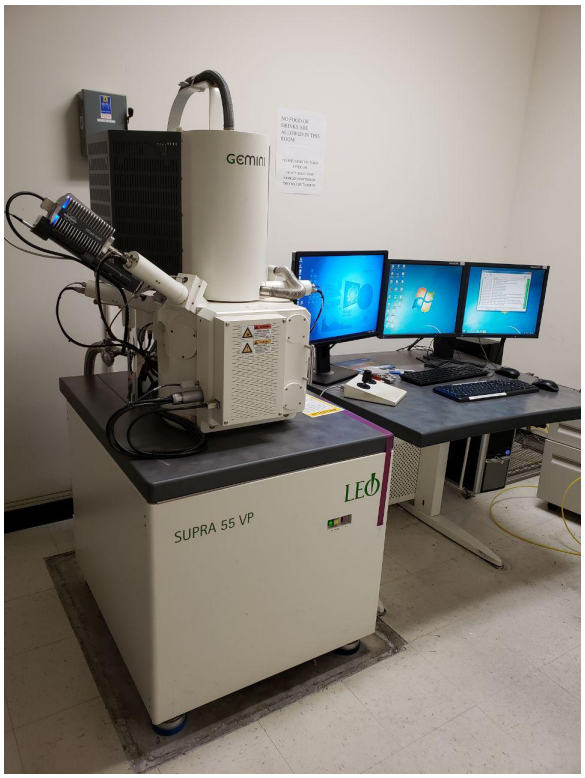

Figure 2.7. SEM Machine at UTA NanoFab used for characterization of our samples.

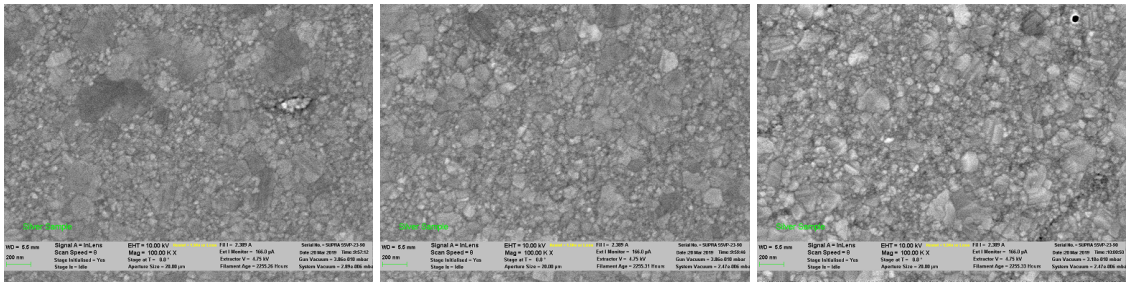

Figure 2.8. SEM pictures of a silver sample use in our experiments..

3

COMSOL Simulations

3.1 COMSOL Multiphysics Software

COMSOL Multiphysics is a simulation software, based on Finite Element Method [14], that is capable of implementing several fields of study in physics, simultaneously. As an instance, assume we want to study how much and at what rate a transistor gets hot if it's used in a certain circuit. For this purpose we need Heat Transfer module and AC/DC Module, or any other module that includes electric circuits. Then we couple these two and apply experimental conditions, including initial temperature, dimensions, material

properties, frequencies and so on. The software is able to mimic these conditions and calculate mutual effect that these factors may have in real experiment.

It has fairly simple interface, so everyone can learn how to work with it. General procedure is the same among all modules with some minor differences. Here is an outline of the workflow one should follow in order to simulate processes in optics module.

- First to choose the symmetry on the model and specific branch of study inside a module. It then takes us to the main window of interface where we construct our model in model builder tab.
- To define global constant parameters and variables to use them easily later on.
- In geometry section under "component", to build the geometry of the model. The model can be in 2D or 3D depending on the symmetry of the device we are working with. If the device has a periodic structure, we can include only one pitch, and add the periodic conditions. 2D simulation are usually run much faster than 3D ones.
- To Fill the geometrical domains with default or user defined materials. Here COMSOL has a material data base, with all the necessary optical properties, but it's also possible to add or change them.
- We mainly worked in "Electromagnetic Waves, Frequency Domain" of the "physics" section, to identify or parameterize the polarization and intensity of the light, as well as its incoming direction.
- To couple the models using multiphysics in case that more than one module is applied.
- To mesh the geometry using automatic option or manually adjusting its size. The finer mesh gives use more accurate and detailed results but increases running time.
- To run the simulation using "Study" over all or certain domains of geometry, with specific frequency, angle, etc, conditions.

- To get results and graphs in 2D or 3D inside the program or extracted in variety of formats.

3.2 Single Layer Simulations

For the first task in our simulations we check for the thickness that provides the best SPR signal for our gold sensor. Throughout this chapter we assume that the laser's wavelength is 632.8 nm and prism index is 1.7847. Otherwise it'll be explicitly mentioned. Figure 3.1 shows simulation for reflectance as a function of the thickness from 40-55 nm and angle from 32-40 degrees. The gold layer is located on top of a prism and it's in contact with air on top. The best signal for this structure is obtained when we deposit a film as much as around 48 nm thick.

The laser beam used in our lab when p-polarized, puts out the intensity of $\simeq 1mW$ that is distributed over the area of $9mm^2$, so in order to get the correct approximation for physical quantities here, we choose input port intensity such that it provides the same intensity over area. In 2-D simulations the port is one dimensional and we need to calculate the area as the length of the port times the unit length in perpendicular and out of plane direction. Therefore, if the port with active excitation has the length of $1\mu m$, and we are using 2-D simulations, the intensity needs to be $111\mu W$ to provide the same conditions as in the lab. The vertical length has to be more than one wavelength to correctly show the electric field values.

Figure 3.2 shows the changes in maximum E-field on the surface of 48 nm gold film, as a function of angle for both vertical and horizontal directions, and also the total field, along with the reflection curve, while there is vacuum on top. A sudden pulse of E-field happens at or close to θ_{spr}. This feature is not specific to gold film but for any metal that supports SPR condition at some laser frequency. However the magnitude of the highest

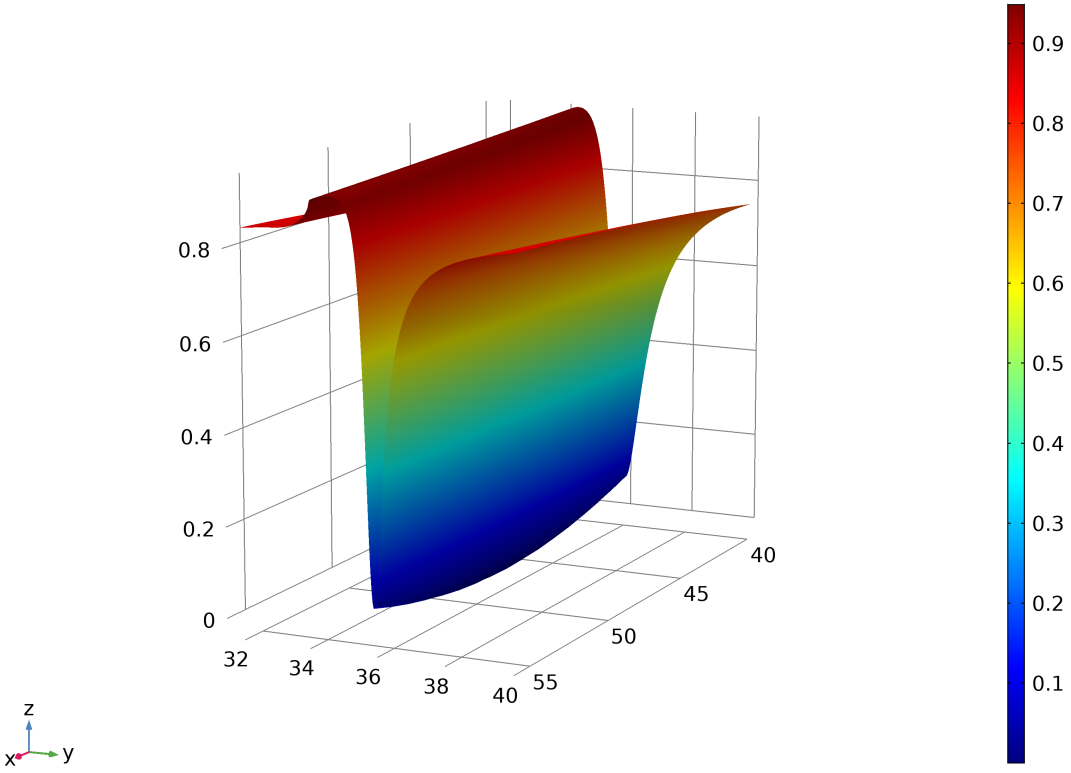

Figure 3.1. Reflection plot of Au with varying thickness of 40 to 55 nm in x- direction and angle range of 32 to 40 degrees in y direction. z axis shows the reflectance..

value that can be achieved depends on the material and quality of the film. The highest magnitude for $\lambda = 632.8nm$ laser is achieved when a $50nm$ silver film is deposited.

Figure 3.3 shows how E-fields change in z- and x-direction at different angles surrounding the SPR angle. Before critical angle θ_c there is a transmission of light that leans toward perpendicular direction with respect to the surface of the film as we go forward in angles. At θ_c transmission becomes completely perpendicular.

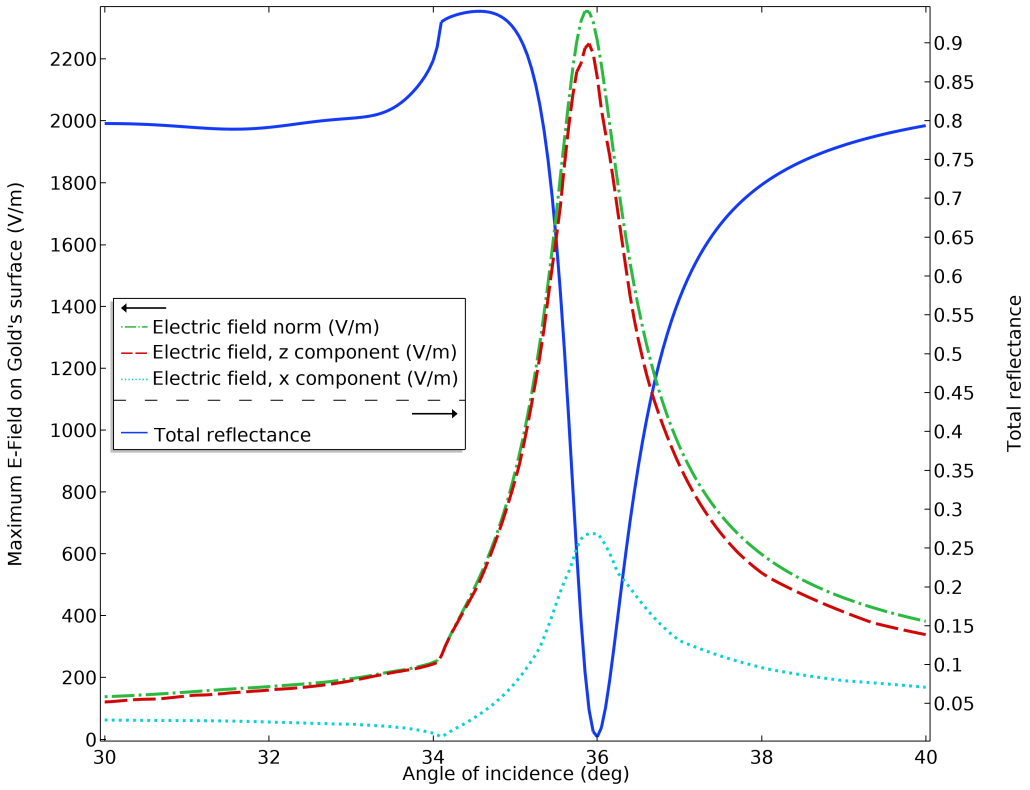

Figure 3.2. Strength of various components of electric field on gold along with SPR curve, For 1mW laser intensity over 9 mm^2 area.

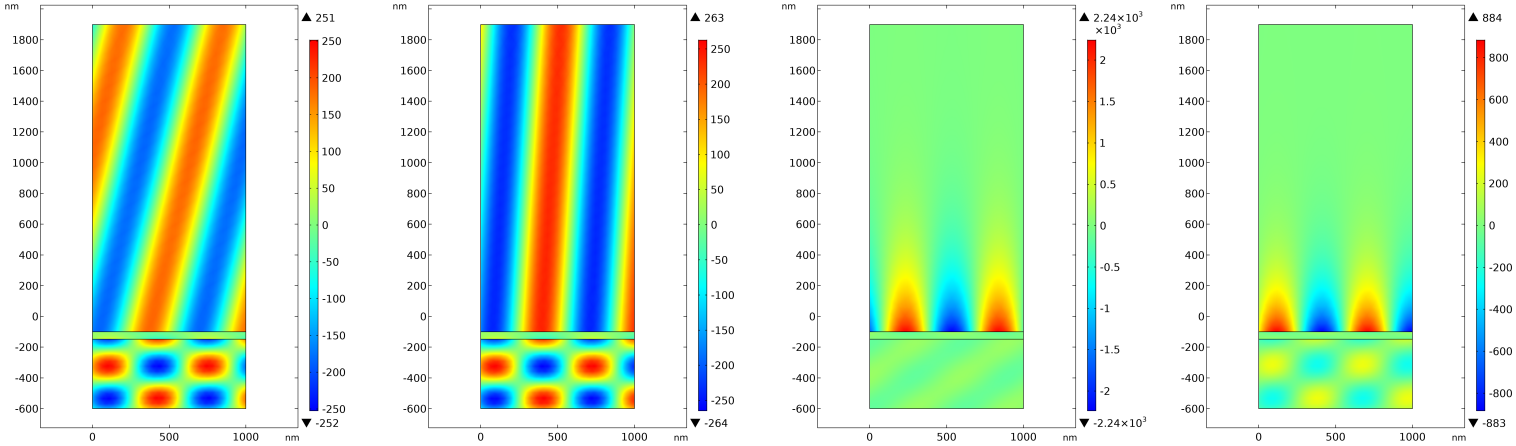

(a) Vertical component of E-field

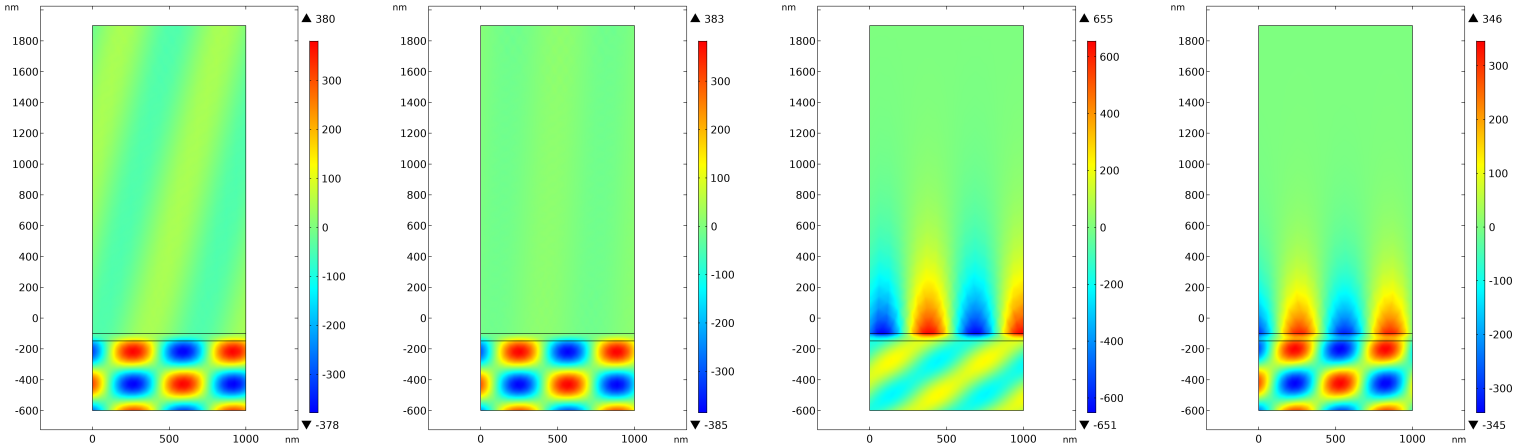

(b) Horizontal component of E-field

Figure 3.3. Incidence angle from left to right: 33°, 34°, SPR=35.9°, and 37° in Prism-Gold-Air system.

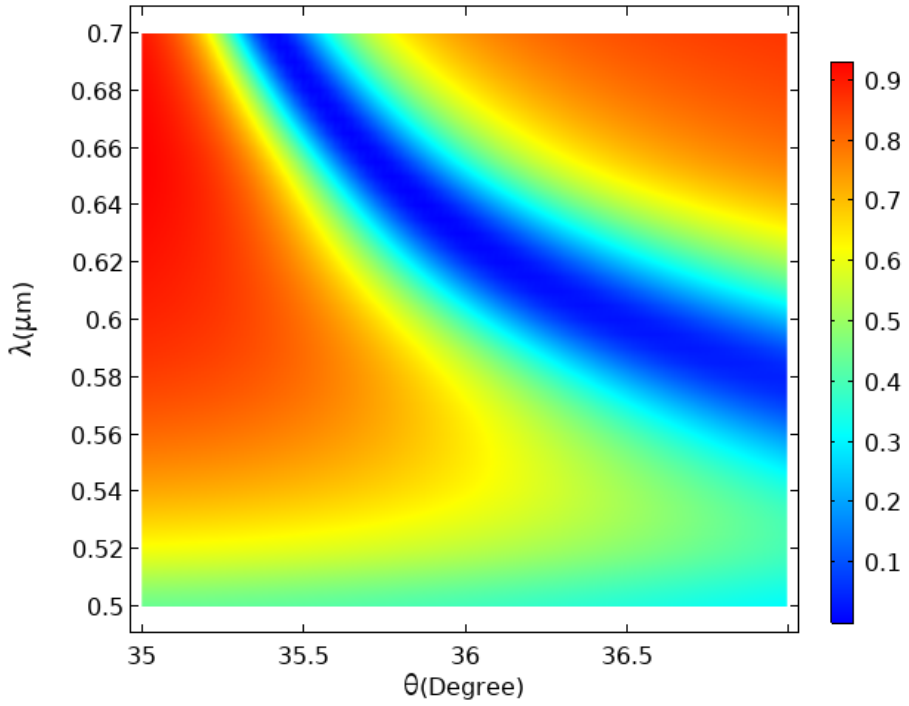

Figure 3.4. Reflection plot as a function of wavelength and angle for the gold film.

By getting closer to θ_{spr}, fields become evanescent. In other words they decay as they get away from the metal's surface. Meanwhile their magnitude close to the surface, increases rapidly and peaks at θ_{spr}. After resonance angle, fields remain evanescent but strength and decay length starts to decrease while reflection is retained.

As discussed earlier, SPR angle depends on dielectric constants of the metal and they are a function of incident light's wavelength. It's possible that for certain wavelength range, particular metal shows a good SPR signal, while not for the nearby regions, as the important condition of $|\epsilon_r| >> 1$, may not be applicable any longer.

For example the Figure 3.4 shows how reflectivity changes with incoming laser's wavelength for 48 nm gold film. For $\lambda < 0.55\mu m$, the signal starts to flatten out and disappear, meaning that by changing the angle, there is no significant or sudden drop in the reflectance any more.

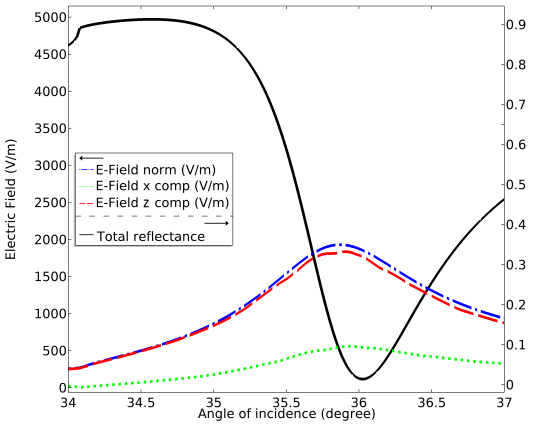

Figure 3.5. Cu SPR and Max E-fields.

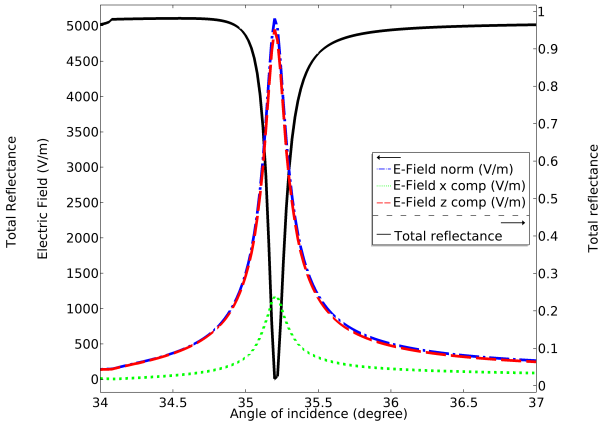

Figure 3.6. Ag SPR and Max E-fields.

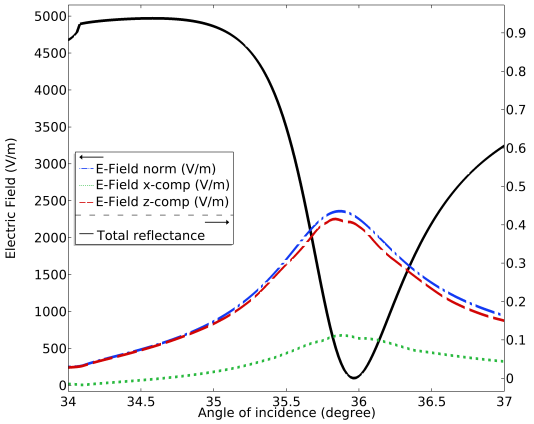

Figure 3.7. Au SPR and Max E-fields.

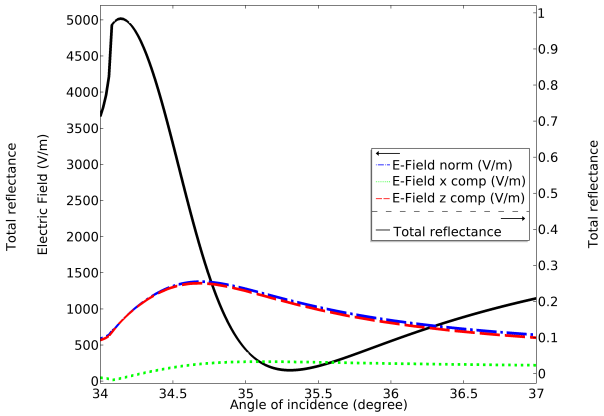

Figure 3.8. Al SPR and Max E-fields.

The quality of the signal and the strength of its evanescent field is not the same among noble metals for particular laser beam. Figures 3.5 - 3.8 compares SPR signal for copper, silver, gold and aluminum as a non-transition metal, in conjunction with electric field strength for a range of angles.

By far, silver has a much better and sharper signal and highest magnitude of electric field on the surface. Despite these advantages, silver oxidizes much faster than gold and the sample degrades over the time, as well as the signal itself. Gold sample on the other hand has less quality of the signal and almost half of the electric field strength, but it remains intact much longer than silver. Copper has downside of both; although it's tempting to

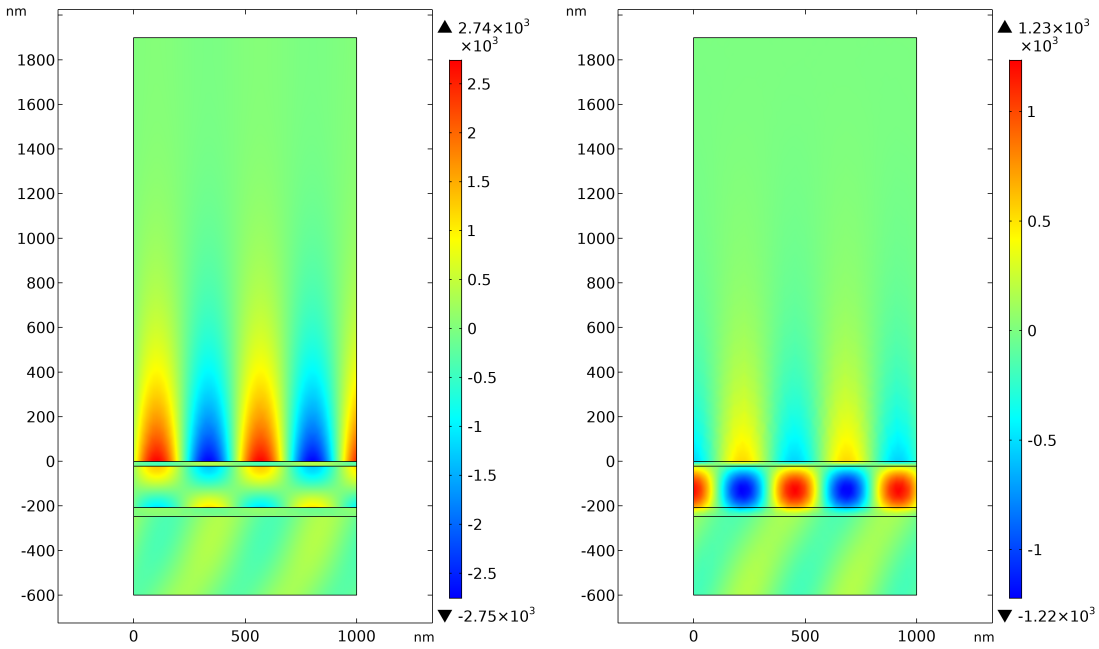

Figure 3.9. $Ag/Si_3N_4/Au/H_2O$ Field with prism index 1.496 and water on top for z (left) and x (right) directions.

excite SPPs on it and see how it can affect the catalyzing property of copper in some chemical interactions.

3.3 Multilayer Simulations

As was done previously in our group, the performance of sensors with bi-metallic layers and bi-metallic waveguide coupled sensors has been investigated in details [2]. These sensors usually use silver as their base layer metal, and cover the outer layer with gold, so it provides the positive effects of both metals at the same time. Silver generates high quality SPR signal while the gold layer protects the device from degradation. A detailed contour plot of the electric field at resonance angle for the configuration of: prism (n=1.5)/Ag/Si_3N_4/Au/water is shown in Figure 3.9, for fields in z (left) and x (right) directions. The field strength of this sensor is almost the same as silver sensor, while decay length of evanescent fields for this device is more than 100 nm longer.

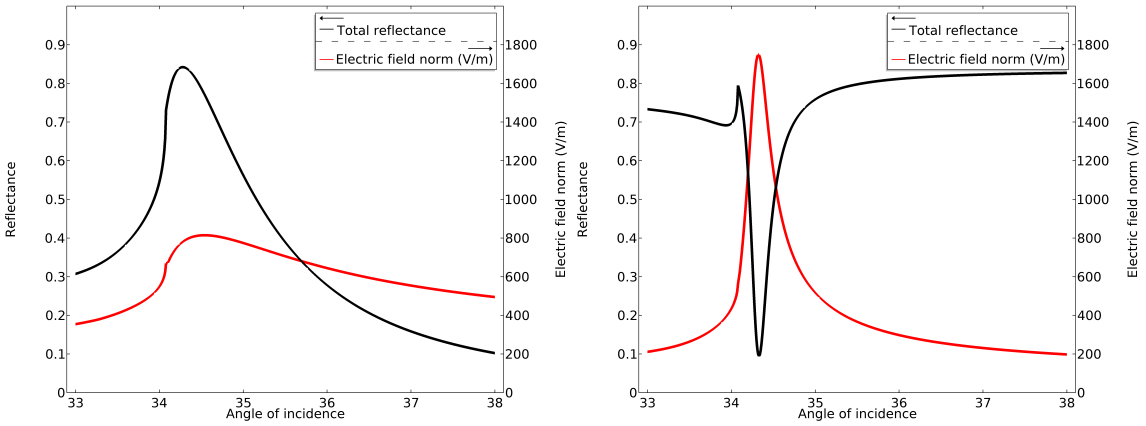

Figure 3.10. Resonance condition on Niobium, in case of single layer Nb sensor (left) and multilayer Ag(50nm)/HfO_2(130nm)/Nb (20nm) sensor (right) using 1.78 index prism and He-Ne laser.

In addition to enhancement of electric field's decay length, this technique can even improve SPR signal for metals that have a large "full width half maximum" or (FWHM) which is a criteria for sharpness of the signal. For example, sensor with single Niobium layer, has an unusual SPR signal in case of He-Ne laser. But making a stack of silver, waveguide (here HfO_2 is chosen) and Niobium, can improve the overall SPR signal dramatically as we can see in Figure 3.10.

Since Niobium shows superconductive properties at very low temperatures, making above mentioned multilayer sensor, can help us run experiments that studies the effect of surface plasmon resonance and superconductivity on each other.

3.4 Hemispherical Dielectrics on Silver

If the thickness of the waveguide becomes non-uniform, then we start seeing the effects due to diffraction. This will be discussed in the next section, but for now we investigate the case that a semi-cylinder strands of HfO_2 with radius 150 nm, located on a uniform 37 nm silver film, with 500 nm distance from each other. The simulation only involves one

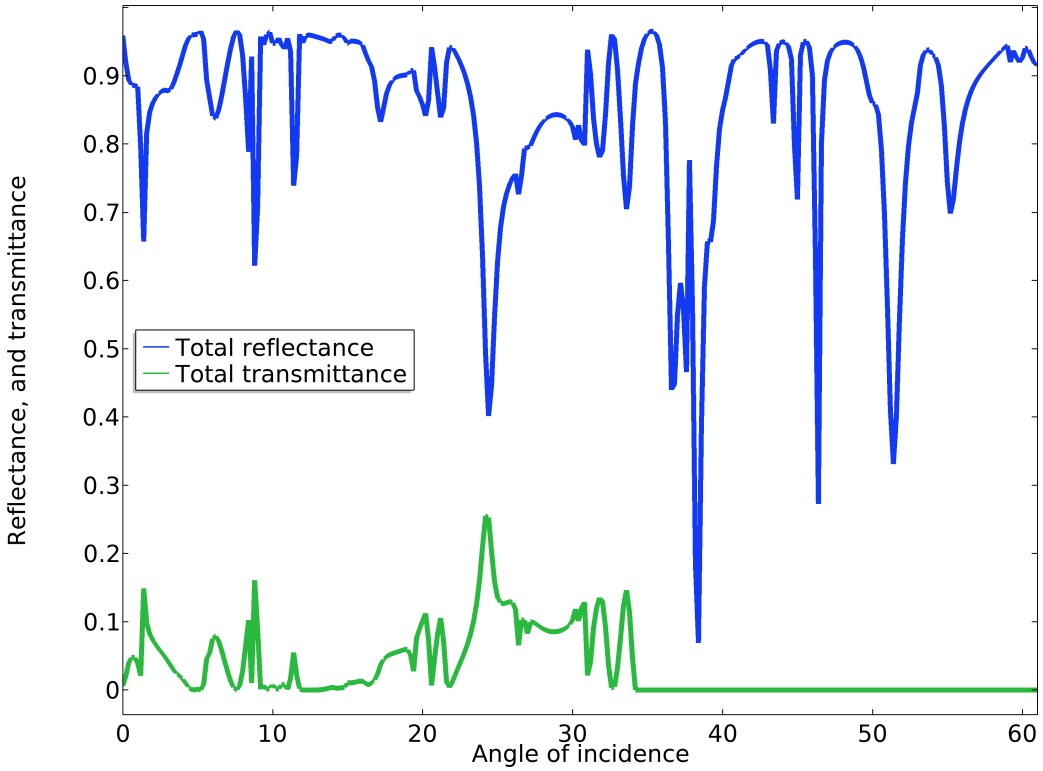

Figure 3.11. Reflection from silver sensor with HfO_2 strands.

unit of in 2D, but we apply floquet periodicity to include repeated structure of this unit. Here also light is hitting the sample from the bottom of the unit.

Now due to the complex effect of diffraction at different angles, we get a much more spiky pattern in total reflection and transmission as in Figure 3.11 for such a structure. One interesting aspect of this structure is that it creates far field electric fields, more than a few hundred nano meters away from the surface of the sensor, which was not possible to create for the regular and uniform film. Figures 3.12 - 3.17 show these fields for several select angle of incidence.

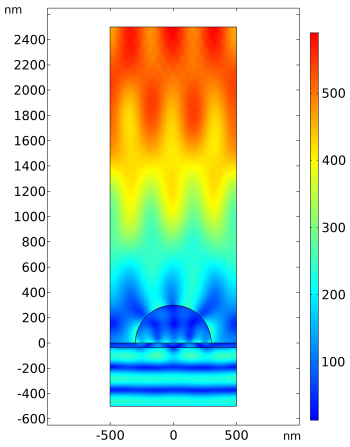

Figure 3.12. $\theta_{in} = 8.6°$.

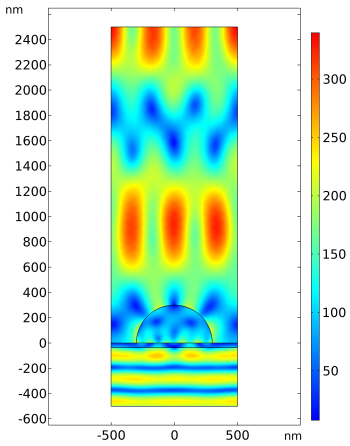

Figure 3.13. $\theta_{in} = 11.2°$.

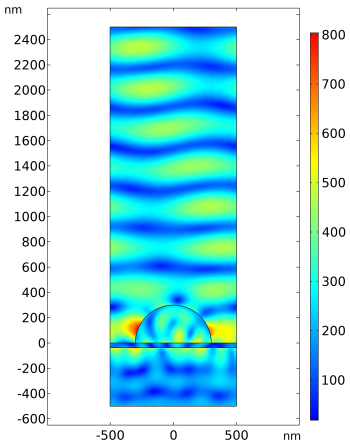

Figure 3.14. $\theta_{in} = 24.2°$.

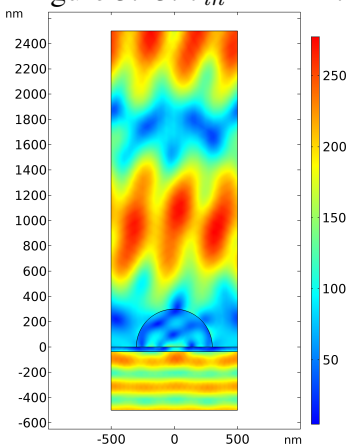

Figure 3.15. $\theta_{in} = 31°$.

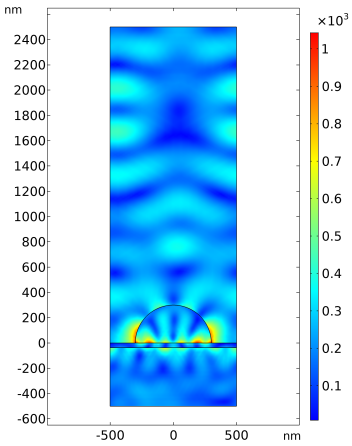

Figure 3.16. $\theta_{in} = 37°$.

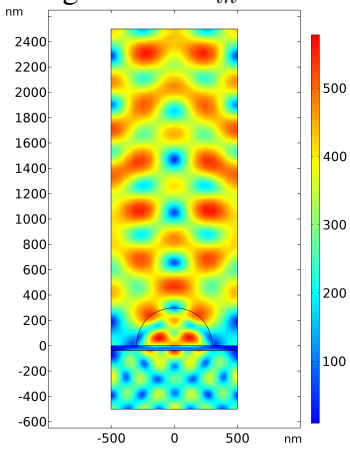

Figure 3.17. $\theta_{in} = 46°$.

Figure 3.18. Electric field for prism/silver/HfO_2(half-cylinder)/Air configuration.

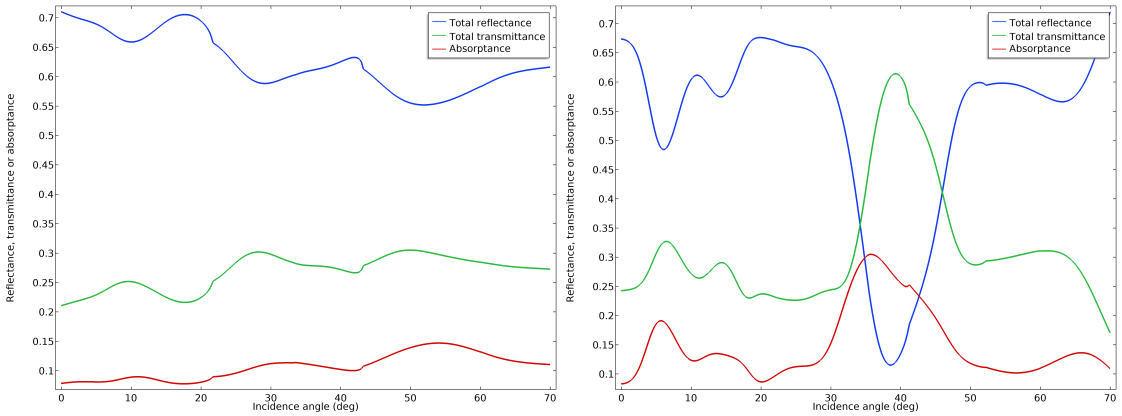

Figure 3.19. Grating simulation for $\Lambda = 1\mu m$ (left) and $\Lambda = 1.5\mu m$ (right) of 30nm gold film. Peak to peak in grating is 150 nm.

3.5 Grating Simulations of SPPs

As was mentioned in the introduction chapter, another method to excite SPPs is to use grating structure and here we ran simulations to demonstrate how grating can transfer energy of the electromagnetic light into surface plasmons. In this set of simulations, light is coming from the air on top with angle θ and hits a sinusoidal grating structure of gold film with periodicity of Λ, coated over glass with the index of 1.5.

The peak to peak distance of the sine wave is chosen to be $150nm$, and the thickness of gold film to be $30nm$. Changing the periodicity would shift the resonance angle for specific diffraction order and may also change the number of possible resonances mainly depending on how it's compared with the wavelength of the light and refractive index of the dielectrics involved.

Figure 3.19 shows how total reflectance, transmittance and Apsorptance changes as a function of incidence angle for two different grating periodicities. As we increase Λ, more orders of diffraction become possible, that's why the one with $\Lambda = 1.5\mu m$ seems to have more minimums in reflection compared to $1\mu m$.

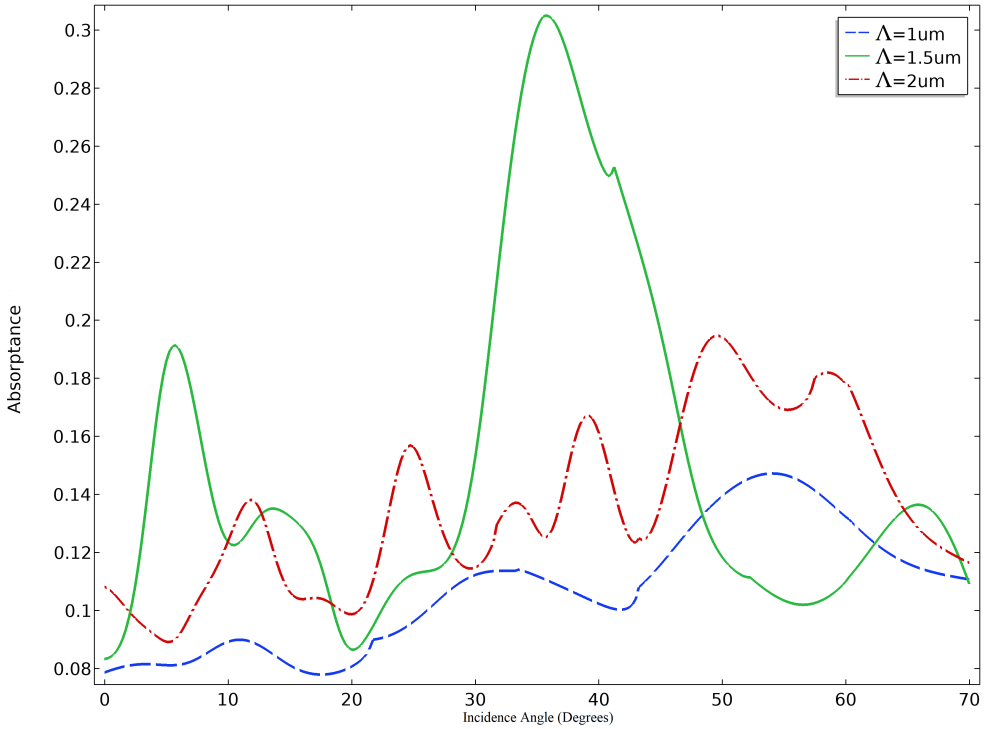

Figure 3.20. Absorptance plot of a 30nm thick gold film on glass in contact with air and for different periodicities.

Like it was mentioned in the introduction chapter, grating causes diffraction in both reflected and transmitted light, but not all diffraction orders are possible to be observed and they are limited by the wavelength and angle of the incidence light and also by periodicity, see Equation 1.51 and Figure 1.13. Each minimum in reflection or in other words each maximum in absorption, corresponds to particular diffraction order. Figure 3.20 shows how the absorptance changes between $\Lambda = 1\mu m, 1.5\mu m$ & $2\mu m$. The existence of a metal coating on glass has caused diffraction orders to temporary vanish due to the fact that their energy is carried out by surface plasmons, since at this angle of incidence they satisfy Equation 1.52 for the gold film.

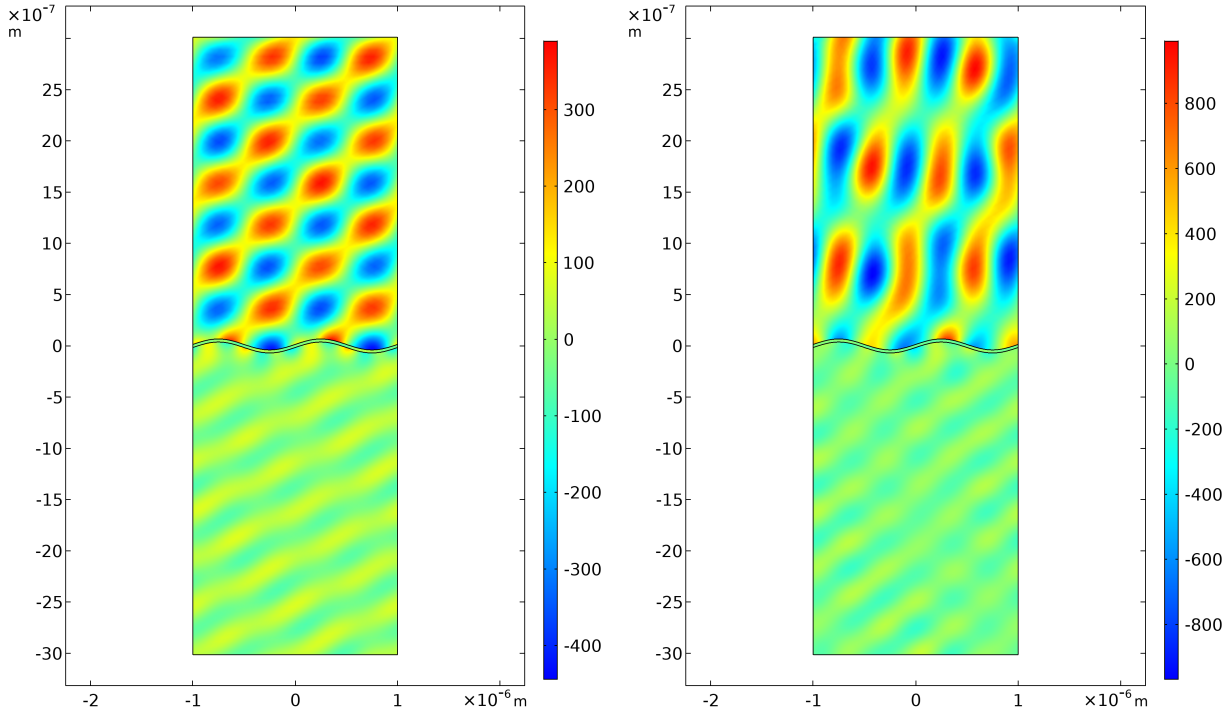

Figure 3.21. Vertical Electric field at $\theta_{inc} = 40°$ (left) and $\theta_{inc} = 54°$ (right), Air/Gold-film/Glass. Input laser power is $1mW$ and it's coming from the air side on top..

4

Experiments and Data

4.1 Kretschmann Configuration

In our experiments, we have used Kretschmann configuration as well as an optimized version of it that provides some advantages in comparison with the traditional configuration. [1,15,16] The laser source which is used in both cases, is the He-Ne type with nominal output power of 10 mW, but in practice it puts out less than 4 mW. Most of optical or optomechanical devices in setups are ordered from Newport^{TM} or Edmund optics website. Next in the line, as we see in Figure 4.2, is a filter mount, which enables us to adjust the intensity of the light to the amount we need using a set of filters.

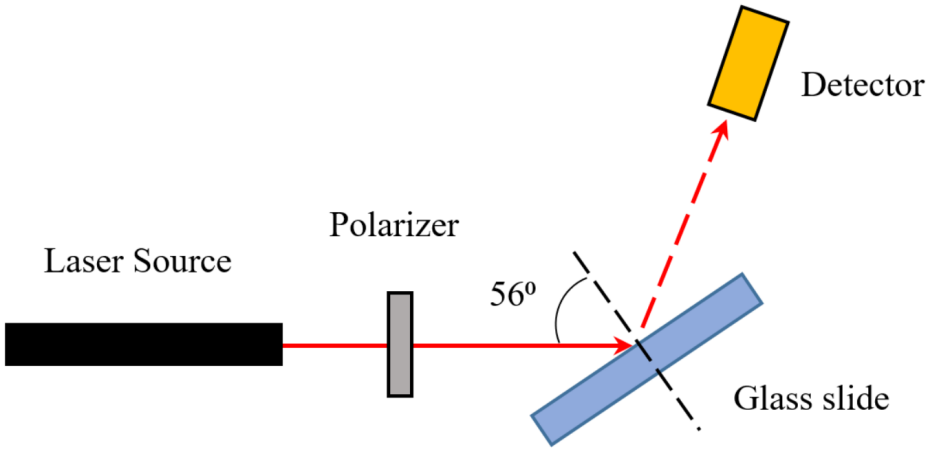

Figure 4.1. Schematics for checking polarization of light using Brewster angle. No reflection is detected when the beam is perfectly p-polarized.

The laser beam of course isn't polarized as it leaves the source and in order to get a p- or s-polarized light, we have to add a polarizer, preferably in a rotation mount that allows us to change the polarization if necessary. As we raised this topic before, Brewster angle would help us to check whether our beam is quite enough polarized. This is done by taking a thick regular glass slide with index of 1.5, to position it in direction of the laser beam , so that the incidence angle be at $56°$. This is Brewster angle for the Air/Glass combination. A perfectly p-polarized light, would have no reflection from Air/Glass interface, since only s-polarized wave has the ability to be reflected at this condition. see Figure 4.1.

Then we add a beam splitter to get reference from the intensity of the incidence beam and normalize transmitted and reflected light based on that, as we know the intensity of the laser even at its best performance, is not completely stable and fluctuates a little bit. So to get the most accurate data, they have to be normalized accordingly.

At this point, beam is ready to be used for generating SPPs and it's guided through a prism that is located and fixed at the center of a $\theta/2\theta$ goniometer. If prism had a half-cylinder shape, then a simple alignment could give us the incidence angle which is mea-

sured with respect to the base of prism.. In case of using a triangular prism, a conversion formula is needed to determine this angle and it's mentioned on page 83 of reference [2].

Now we can affix our deposited layer of metal, to the back of the prism. As was stated before, our depositions are usually done on a piece of silicon dioxide, or regular glass slides. These materials have the index of $\sim$1.45 and $\sim$1.5 respectively, while the prisms that we utilized have either n=1.7847 or 1.496. Slides are attached to prism from the opposite side that the deposition is done. To remove the air between these slides and prism, we used matching oil with an index that is between the indices of prism and slide, to prevent total internal reflection and allowing the beam to reach the sample at all angles.

The material in contact with the deposited layer of metal, and at the vicinity of incident laser spot, determines the SPR angle. Since the prism is sitting on its triangular side, while the sample is attached to the square side, changing the ambient material from air to liquids, is a little bit challenging. To do so, we've made a cubic container out of Teflon or polytetrafluoroethylene (PTFE), which will be shown later in this chapter.

After reaching the sample, the beam splits into three components. One is absorption by the sample which we can't detect. But the other two, which include transmission and reflection are measured by two silicon detectors in front of each beam. The signal then is transferred to the computer for further analysis. The device and software installed for analyzing the data was Science Workshop 750 from PASCO.

The above mentioned method has some downsides that is generally caused by rotating prism, including having the beam that hits at different spots of the sample as we go to a different angle. So throughout the experiment, we are not sure if the signal is only affected by changing the angle or it's also changed due to the hitting at a different part of the sample. Since the sample is not exactly uniform, this could cause misinterpretation of the data.

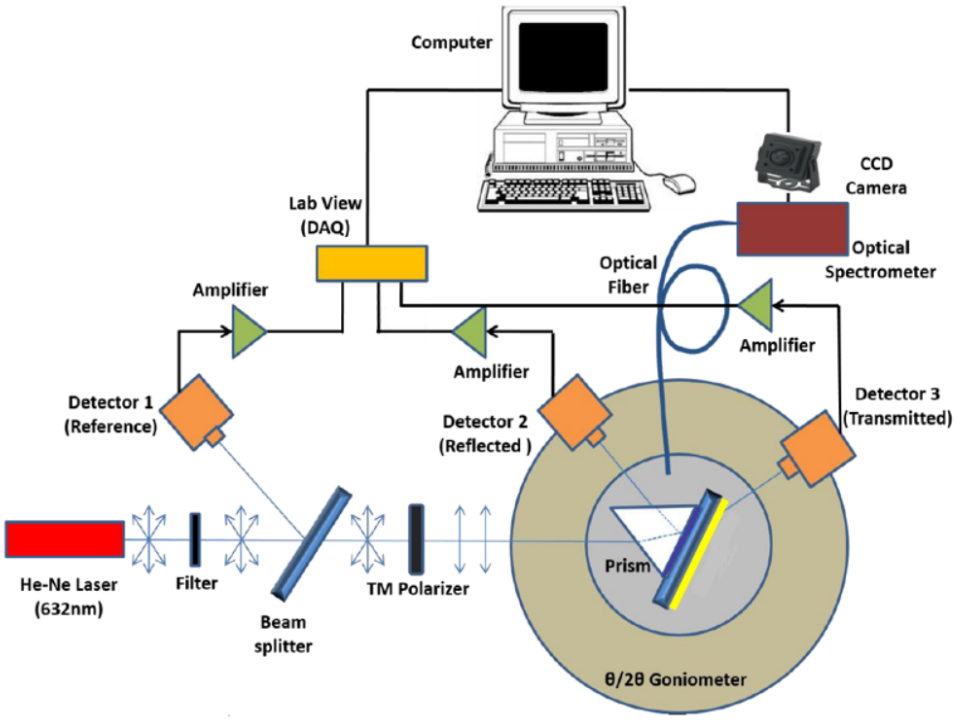

Figure 4.2. Kretschmann configuration for creating SPR. Figure from [1] with some corrections.

4.2 Fixed Detector System

To overcome some problems that comes up with traditional Kretschmann configuration, a fixed prism and detector setup has been proposed, previously in our group, in which the change in angle is taken care of by using several mirrors along the way and those mirrors, change the direction of the laser beam such that it hits the base of prism in a desired angle. [17–20]

As is shown in Figure 4.3, in this configuration, prism is fixed while its square side is facing upward. This allows us to simply put a drop of solution or any material we want to investigate, on top of the sample and there is no need for using another device to hold it for us. It also provides the conditions for running quantum dot experiments that will be discussed later in the next chapters.

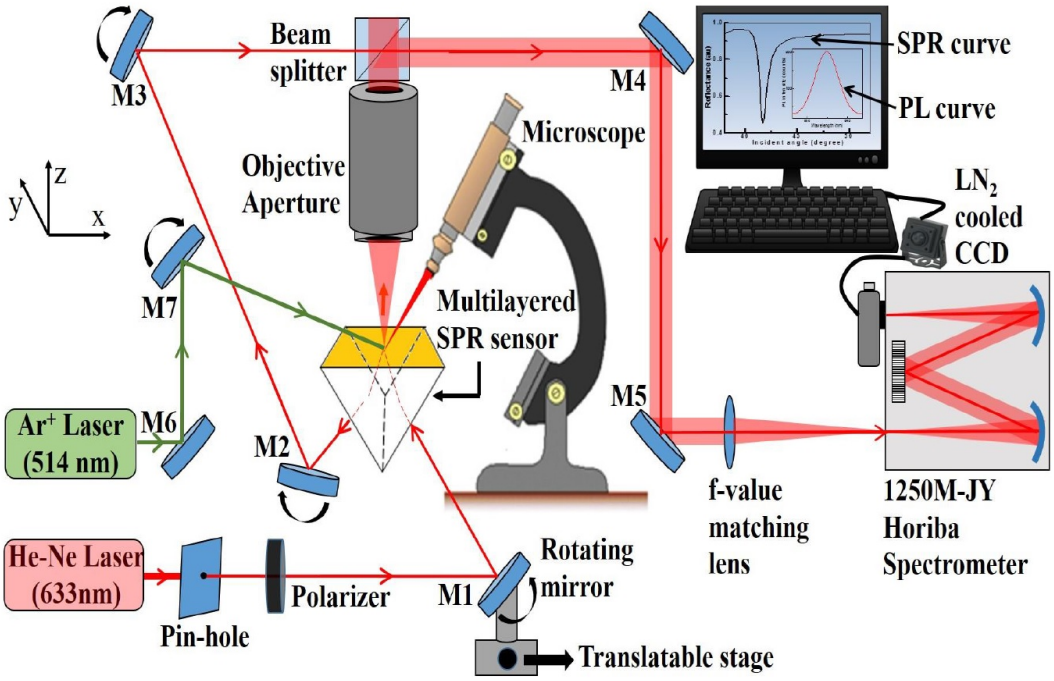

Figure 4.3. Fixed prism and detector configuration, Figure from [2].

Here by rotating the mirror M1, we can change the incidence angle and at the same time, use M7 mirror to guide the reflected light to the detector for intensity measurements. Again a conversion formula is used to figure out the incidence angle on the base of prism, based on the angle of mirror M1.

The Green laser beam coming from Ar^+ Laser source in this setup is not yet discussed but it will be in next chapters when we bring up the interaction and coupling between quantum dots and SPPs. But the setup works well without this laser in order to produce SPR effect.

4.3 Sensitivity and Resolution of SPR Signal

To better define sensitivity, let's rewrite Equation 1.36 as

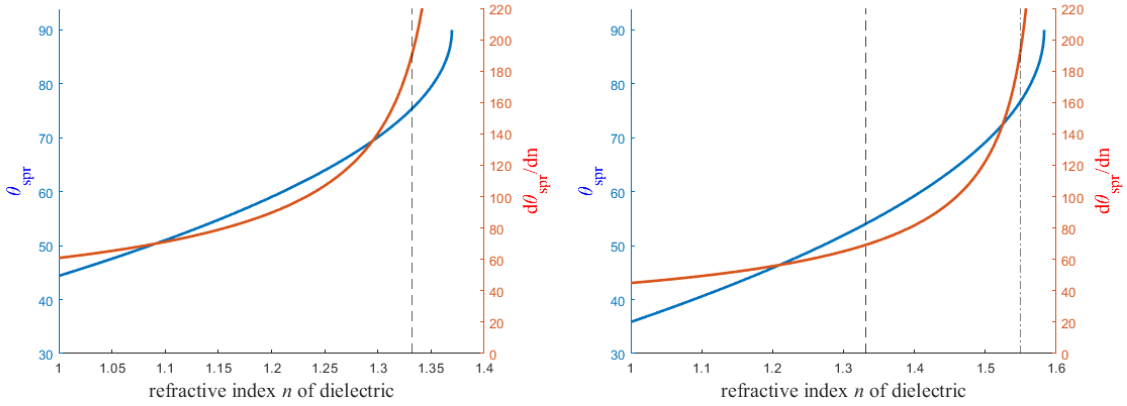

Figure 4.4. θ_{spr} as a function of dielectric's refractive index for a gold film and prism index of $n = 1.4960$ (left) and $n = 1.7847$ (right) in Kretschmann configuration.

$$\sin\theta_{SPR} = \frac{1}{n_p}\sqrt{\frac{\epsilon_m n_d^2}{\epsilon_m + n_d^2}}. \tag{4.1}$$

where n_d is the refractive index of ambient material, so $n_d^2 = \epsilon_d$, and n_p is the index of prism. Therefore θ_{spr} is a function of n_d. For simplicity we sometimes put $n_d = n$. Figure 4.4 shows this dependence in blue curves for the case of gold film and prisms with $n_p = 1.4960$ (case-1) and $n_p = 1.7847$ (case-2). Case-1 can not detect materials with refractive index higher than 1.375, while this number for case-2 is 1.58. To be able to detect wider range of materials, we ought to use a higher index prism. Red curves show the derivative of θ_{spr} as a function of n_d, or $S_n = d\theta_{spr}(n)/dn$, and it's called sensitivity. Higher sensitivity is desired for a good sensor as it shows significant change in the value of SPR angle as we slightly change the refractive index of material. In the same figure, dashed lines indicate index of 1.33, and 1.55. These are the indices that have sensitivity of about 200° per refractive index unit (RIU) for the case-1 and case-2 respectively.

In general, by changing the dielectric constant of ambient material, the sensitivity in SPR angle is much higher than change in critical angle, like in figure 4.5. Consequently it makes sense to consider SPR angle instead of critical angle for sensitivity purposes. One

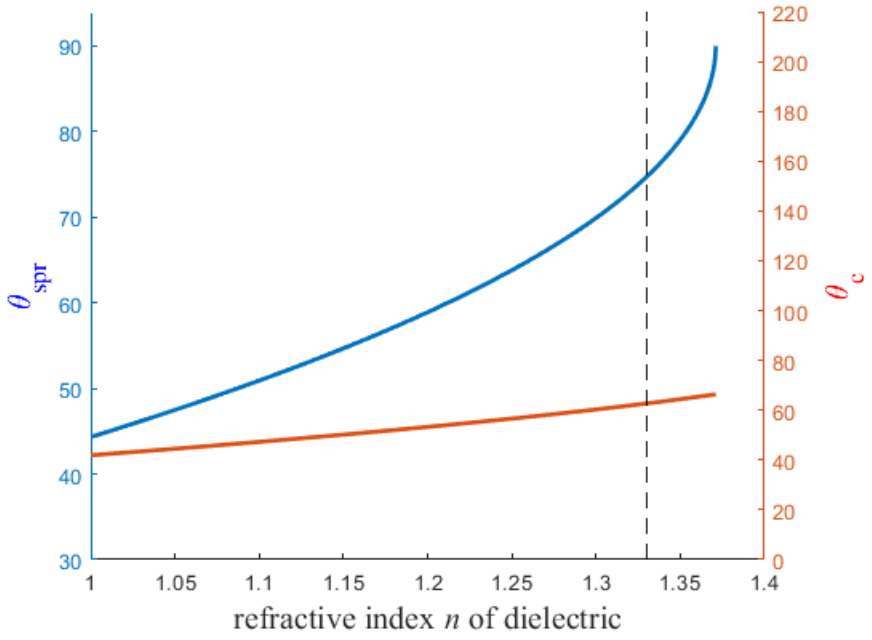

Figure 4.5. Resonance and critical angles as a function of dielectric's refractive index.

important property that should be mentioned here is that sensitivity increases rapidly as we get to the detection threshold of our sensors, which its value depends on the index of prism. This means if we want to have higher sensitivity for particular material, we should choose a prism so that its detection threshold be closely above the refractive index of that material. Considering distilled water as our dielectric (with $n_d = 1.3317$), the sensitivity using case-1 is close to 200° per RIU, while case-2 results sensitivity of about 70°. On the other hand case-1 can't be used for detection of Ethyl salicylate (with $n_d = 1.523$), and case-2 has sensitivity of $\sim 145^\circ$ at this point.

Table 4.1, has listed some common types of prisms along with their detection threshold and the index of material that can be detected by sensitivity of 200° per RIU, with that particular prism. So choosing the prism pretty much depends on the type of material we want to detect and its index is not usually far beyond the index of material.

Prism Type	Prism Index	Index with $S_n \simeq 200$	Highest detectable index
N-BK7	1.52	1.35	1.37
N-SF5	1.67	1.47	1.50
N-SF10	1.72	1.51	1.53
N-SF11	1.78	1.55	1.58

Table 4.1. Detection threshold and material's indices that correspond to 200° sensitivity for some commonly used prism types

4.4 Precise Measurements of Glucose Concentration in Distilled Water

So we now know that SPPs have sensor applications in physics and biology, [21–25] and if we operate these sensors in the right index region of both prism and material, they can be quite precise and highly sensitive. In a particular experiment, we used glass slides to deposit gold with 48 nm thickness, and then used matching oil with index of ~ 1.52 to attach the glass slide on the side of a half-hemispherical prism with the measured index of $n = 1.496$.

The general structure of our sensor is schematically shown in the Figure 4.6. For the simplest sensor, we just have the gold layer, without silver and Si_3N_4 waveguide included. This single gold layer sensor as we can tell from the left graph in Figure 4.4, has a high sensitivity for detecting materials with indices between 1.3 to 1.35, including water with index 1.3317 for $\lambda = 632.8nm$.

To check whether our setup is capable of detecting purity of these materials and to determine to what extent it can do that, we conducted an experiment that can be used to evaluate the concentration of glucose in distilled water. A container of 20% glucose solution was purchased commercially with the measured index of 1.3602. A 20% glucose contains 20 grams of pure glucose powder solved in 100 mL of distilled water.

Also a cubic container with capacity of around 30 drops was designed and manufactured from Teflon and affixed to the sensor. See Figure 4.7. Glass slide will be glued to the

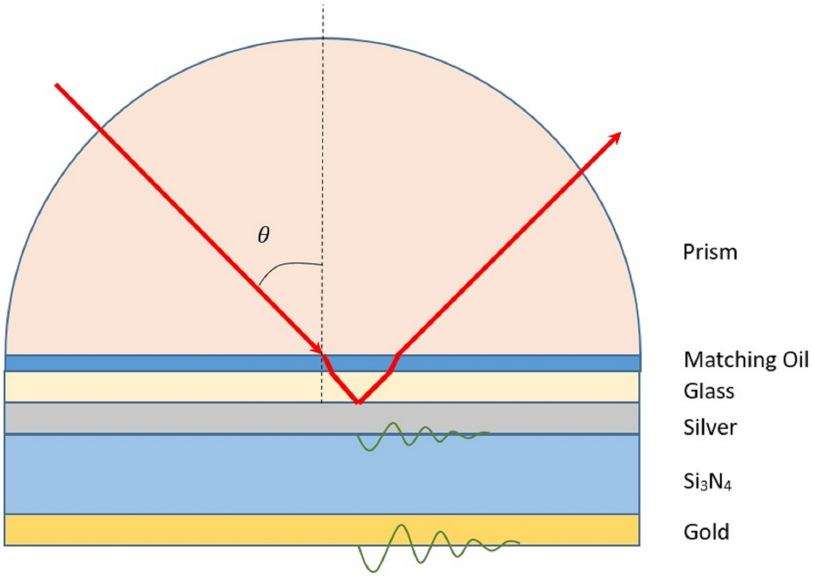

Figure 4.6. Schematics of structure of a bi-metal waveguide coupled sensor attached to a prism.

front face of this piece of cube, while its deposition side is toward the cube, and the opposite side is attached to the prism with matching oil. Then by a pipette, required amount of glucose solution was transferred to the cubic container from the top slit. The setup then was calibrated using the reflection data for known cases like air or distilled water in comparison with the simulations.

In the next steps, we gradually reduced the concentration of glucose. To make a 10% glucose solution for example we took certain volume amount of 20% glucose and added the same amount of distilled water into it. The experiment was run with 10%, 5%, 2% and 1% glucose concentrations, as well as distilled water and air. The sensor was able to distinguish between distilled water and 1% glucose, while the difference between their refractive indices is less than 0.002. This is the case because as the theory suggests, this device should be able to bisect two materials with difference in index of around 0.002, with almost half a degree difference in SPR angle, which is close by outside of our experimental

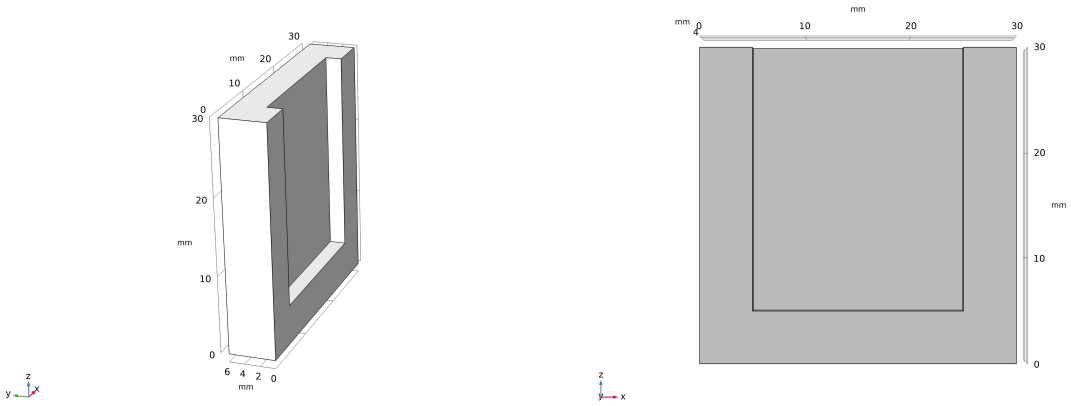

Figure 4.7. Liquid holder of our setup.

error. We couldn't distinguish any lower concentrations due to our limitations in precise angle reading.

The results of experiment is skimmed and shown in Figure 4.8. There is a good agreement between simulation and data in this experiment, but calculations based on the data show that the sensitivity is 167° per RIU, see Figure 4.9 while theoretical values predict it to be $\sim 180^\circ$. This could be due to the difference in metal's dielectric constants that we include in our simulations. According to measurements and interpolations by Johnson & Christy, gold dielectric constants for 0.6328 μm wavelength is given by, $\epsilon_r = -11.740$ and $\epsilon_i = 1.2611$, but the exact values could be affected by deposition and film growth conditions.

In principle we can improved the precision of this experiment and detect the changes in glucose concentration of less than 1% if we utilize a rotation stage that can read angle change of small fraction of a degree. One affordable choice that is available in Newport^{TM} website is the model M-UTR80 with resolution of 0.016°. In this case, we will be able to detect the change of glucose in blood as much as a few mg/dL in a short period of time, by this setup; which is pretty simple and cheap.

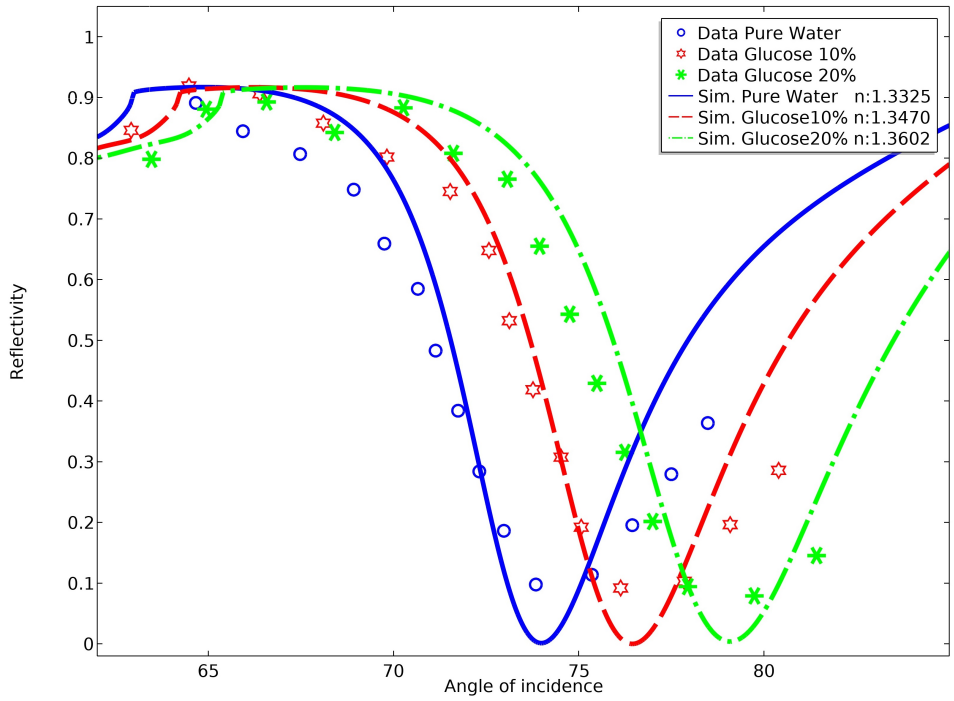

Figure 4.8. Gold sensor reflectivity data along with simulations.

The same experiment was done using multilayer sensor with the structure as the following: Silver(40nm)/Si3N4(186nm)/Au(22m). This configuration has less sensitivity according to simulations, but has stronger evanescent field and higher decay length. The data for this experiment is shown in Figure 4.10, and sensitivity calculations are summarized in Figure 4.11. Again the analysis of these experiments agrees with theoretical predictions to a good extent.

According to our results, there is a linear relation between concentration of glucose solution and its refractive index, see Figure 4.12, although due to experimental errors, this linearity is not perfect.

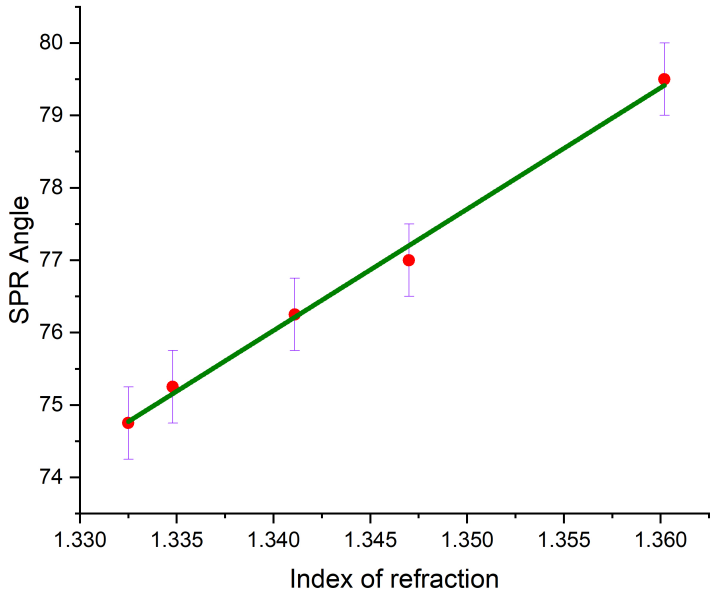

Figure 4.9. SPR angle vs. index of Glucose solution with various concentrations for single gold layer sensor.

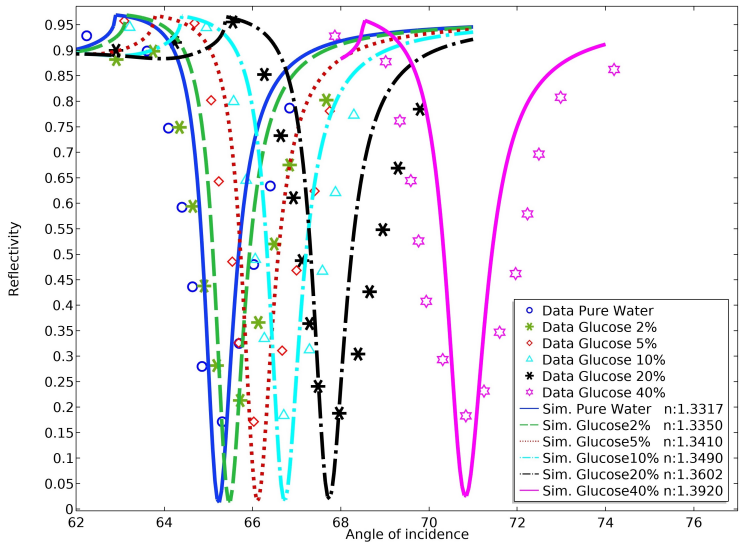

Figure 4.10. Reflectivity data for $Ag/Si_3N_4/Au$ sensor along with simulations.

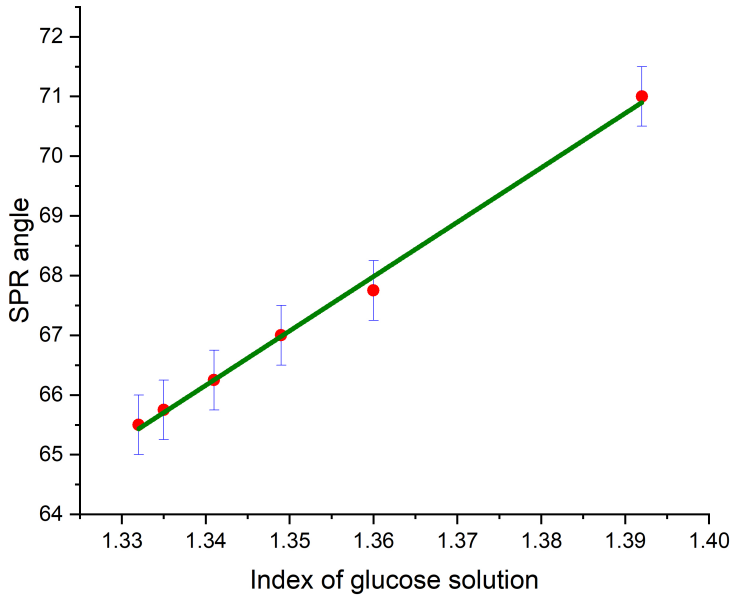

Figure 4.11. SPR angle vs. index of glucose solution with various concentrations for $Ag/Si_3N_4/Au$ sensor.

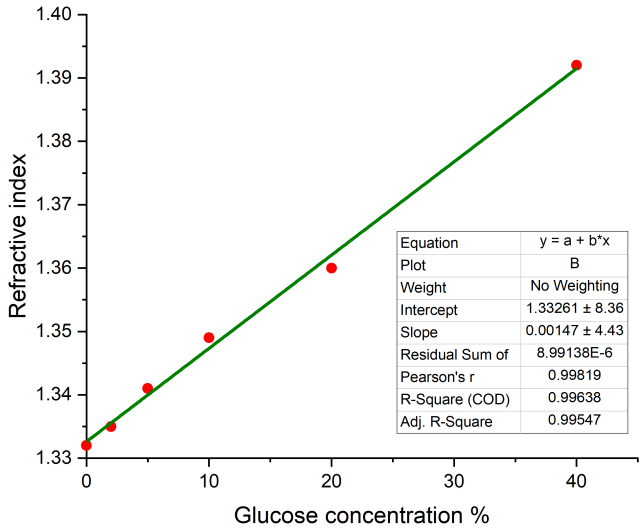

Figure 4.12. Index of refraction vs. concentration of glucose, based on results of experiment with $Ag/Si_3N_4/Au$ sensor.

4.5 SPR Measurements on Several Samples

In many chemical interactions copper acts as a catalyst and it was tempting for us to see if at SPR condition, this property of copper could get enhanced or its efficiency get a boost. In order to test this idea, we had to first check whether copper shows a fair enough signal and how strong electric field it can produce on its surface. It turns out that its property is pretty close to the gold sample. We can use instead our bi-layer waveguide coupled technique and made a sensor with Ag/Si_3N_4/Cu structure that has good characteristics of previous multilayer sensors as well. Figures 4.13 shows the SPR data on copper (45nm), gold (48nm), silver (50nm) and Ag(37nm)/Si_3N_4(160nm)/Cu(21nm) along with their simulated curve. Data and experiment are in pretty good agreement.

In addition Figure 4.14, shows how evanescent electric field stretches beyond the surface of different metals in resonance condition. By making stack of copper, we are in fact making the electric field to go further in distance away from the surface and possibly have more effect if any on its catalyst property.

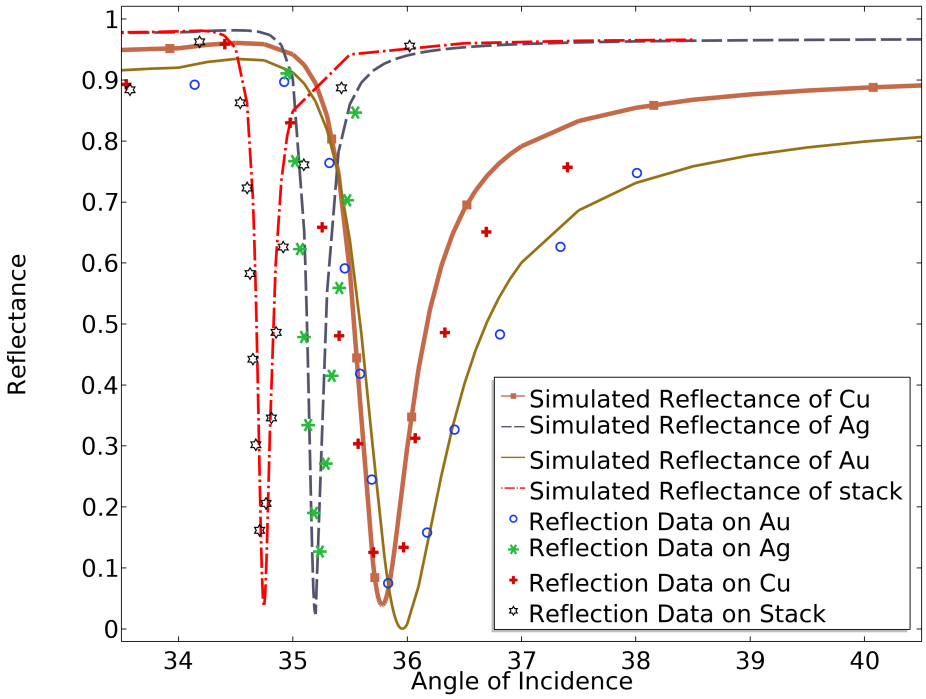

Figure 4.13. SPR data on noble metals.

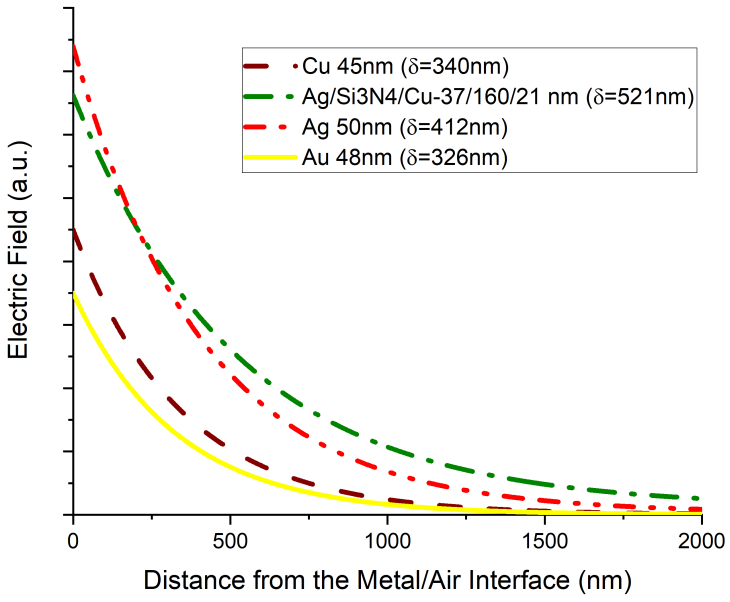

Figure 4.14. E-field decay length for noble metals at SPR condition.

5

Theory and Simulation of Quantum Dots

5.1 Quantum Dots and their coupling with SPPs

Quantum dots (QDs) are nano-scale spherical crystals, made of semiconductors like ZnS and CdSe, typically made of a core, a shell and in some cases, a ligand like tri-octylphosphine, attached on the shell as shown in Figure 5.1. Quantum dots absorb light on a relatively wide range of wavelengths, but their photo-luminescence (PL) is mainly specific to a wavelength that is a signature of that type of QD and it depends on its size. Their size is typically between 2 to 10 nm. The higher size of QDs causes the radiated wavelength to be higher, since the band gap between valance band and conduction band

becomes smaller as the size grows. In that sense, a 10 nm QD radiates a red light, while a 2 nm QD radiates blue light, See Figure 5.2.

Figure 5.1. General structure of quantum dots [3].

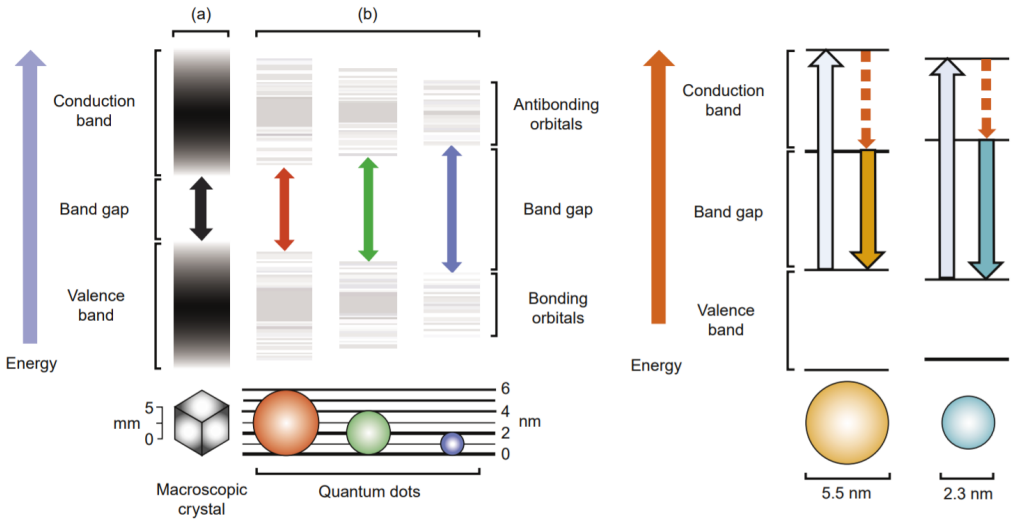

Figure 5.2. Size-dependence of quantum dot radiation [4].

Here we are after exploring the mutual effect of a quantum emitter or quantum dot in particular, and SPPs, when they are coupled. If the PL frequency of QDs lie within the

frequency range of the light used in experiment, then most likely a significant coupling between SPPs and emitters would occur at SPR angle, and it causes dispersion curve to split at the intercept of emitter's frequency line and regular dispersion curve.

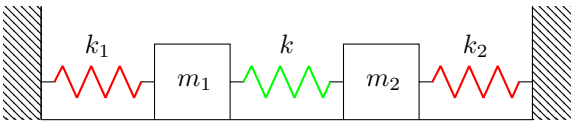

Figure 5.3. Coupled harmonic oscillators.

In classical explanation, two independent harmonic oscillators with natural frequencies of $\omega_1^2 = k_1/m_1$ and $\omega_2^2 = k_2/m_2$, can be coupled using a third spring, with spring constant of k (Figure 5.3). Ignoring any damping effects, differential equations for coupled state are given as [26]

$$coupled: \begin{cases} m_1\ddot{x}_1 + k_1x_1 + k(x_1 - x_2) = 0, \\ m_2\ddot{x}_2 + k_2x_2 - k(x_1 - x_2) = 0, \end{cases} \tag{5.1}$$

that can be rearranged in matrix language:

$$\begin{pmatrix} k_1 + k & -k \\ -k & k_2 + k \end{pmatrix} \begin{pmatrix} x_1 \\ x_2 \end{pmatrix} = - \begin{pmatrix} m_1 & 0 \\ 0 & m_2 \end{pmatrix} \begin{pmatrix} \ddot{x}_1 \\ \ddot{x}_2 \end{pmatrix}, \tag{5.2}$$

while assuming $x_{1,2} = A_{1,2}e^{-i\omega_\pm}$, the above equation is simplified to

$$\begin{pmatrix} k_1 + k - m_1\omega_\pm^2 & -k \\ -k & k_2 + k - m_2\omega_\pm^2 \end{pmatrix} \begin{pmatrix} x_1 \\ x_2 \end{pmatrix} = 0. \tag{5.3}$$

Putting the determinant of the first matrix equal to zero, gives us the following quadratic equation for $\omega_\pm^2$:

$$\omega_\pm^4 - \omega_\pm^2 \left(\frac{k_1 + k}{m_1} + \frac{k_2 + k}{m_2} \right) + \left(\frac{k_1 + k}{m_1} \right) \left(\frac{k_2 + k}{m_2} \right) - \frac{k^2}{m_1 m_2} = 0, \tag{5.4}$$

and by defining $\omega_1'^2 = \frac{k_1+k}{m_1}$, $\omega_2'^2 = \frac{k_2+k}{m_2}$, and $\Omega^2 = \frac{k}{\sqrt{m_1 m_2}}$, we'll have

$$\omega_{\pm}^2 = 0.5\left(\omega_1'^2 + \omega_2'^2 \pm \sqrt{(\omega_1'^2 - \omega_2'^2)^2 + 4\Omega^4}\right). \tag{5.5}$$

$\omega_{\pm}$ are dispersion curves in coupled state and the normal modes of oscillation. One can find similar results using perturbation theory in quantum mechanical analysis. Based on how k is compared to k_1 & k_2, or how Ω is compared to $\omega_1^{'}$ & $\omega_2^{'}$, we would have weak or strong couplings. While $k = 0$, retrieves uncoupled states, the criteria for having strong coupling could be different from one field of physics to the other.

The PL frequency of a particular quantum dot in normal conditions, is assumed to be constant. Suppose we put some of them on a silver film and assign $\omega_1 = \omega_{QD} = 0.25\omega_P$, and $\omega_2 = \omega_{SPPs}$ (same as Equation 1.34), along with coupling strength of $\Omega = 0.1\omega_P$. The dispersion curves would look like Figure 5.4, for $m_1 \simeq m_2$. At the crossing point of ω_1 and ω_2, the curves avoid each other and separation of these two, called anticrossing, is proportional to the coupling strength, i.e. $\omega_+ - \omega_- \propto \Omega$. One crucial result here is that for some interval of θ_i, we'll have two visible light frequencies that have intersection with the coupled dispersion curve (black dots in Figure 5.4). So a plot of reflection intensity vs. wavelength of white light, unlike the decoupled case, will have two minimums rather than one.

5.2 Simulation of Rabi Splitting

We now pursue to simulate Rabi splitting by using COMSOL Multiphysics. In this regard QDs are treated as emitters with dipole moment of [27]:

$$P = \frac{Ne^2}{Vm}\frac{E}{\omega_0^2 - \omega^2 + i\gamma\omega,} \tag{5.6}$$

in which N/V is the number of QDs per unit volume, e and m are the charge and mass of electron respectively, ω_0 is the PL frequency that QDs emit, γ is the loss factor and ω is

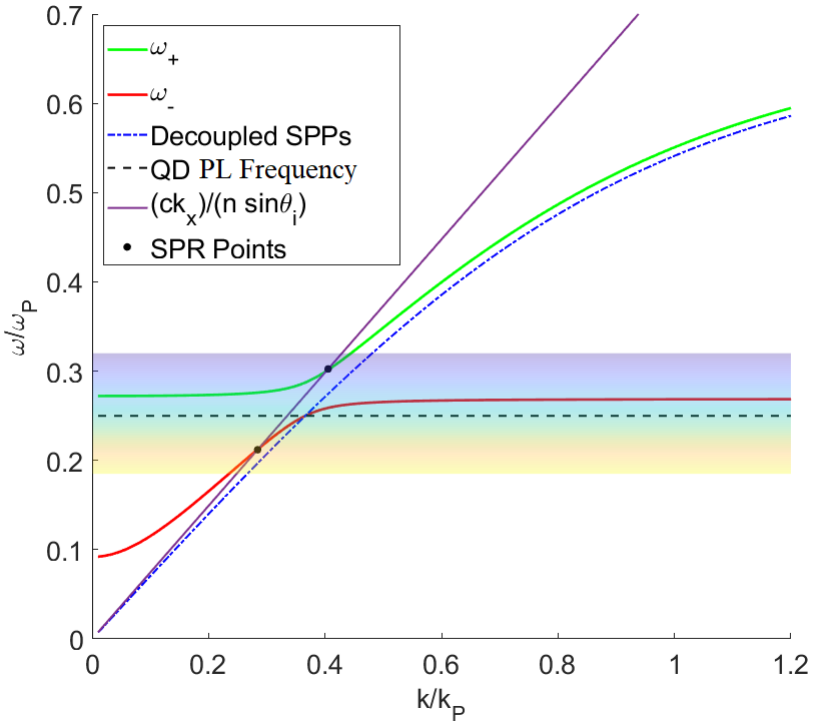

Figure 5.4. Rabi Split for hypothetical QD coupling with SPPs of silver and $\Omega = 0.1$.

the frequency of the incidence light. This equation is derived by solving displacement r in Drude Model differential equation:

$$m\ddot{r} + m\gamma\dot{r} + m\omega_0^2 r + eE(r,t) = 0,$$

and letting $P = -er$.

Electric Field E decays exponentially in z-direction with decay length of $\sim$ 400 nm for the case of 48 nm gold film, and a prism with 1.7847 index and He-Ne laser with $\lambda = 632.8$ nm; but since the emitters are assumed to be at the distance of a few nano-meters above the surface, the field that they experience is almost constant in magnitude, although it flips in direction every about 100 nm along the surface.

There is also an electric field in x-direction with 90 degrees phase shift, but it's much smaller in magnitude, see Figure 1.4. The same logic used for surface plasmon oscillations

can be used for single electron oscillation inside a QD, while they are treated as emitters with dipole moment in Equation 5.6 and coupled to the evanescent electric filed, while now ω_0 is the PL frequency of QDs emission, and γ is the loss factor in quantum dot. As explained above, QDs experience almost a constant evanescent field due to their small size ($\leq 10nm$), while usually for the decay length of these fields we get around several hundred nanometers.

Simulation results for maximum strength of these evanescent fields in z-direction on 48 nm gold film for the incidence wavelength range of 550 nm to 750 nm, and angle of incidence between 35 and 37 degree is shown in the Figure 5.5. Real part of the gold dielectric constant doesn't have high enough magnitude to show a strong SPR effect for wavelength less than 550nm.

Then we fit a two independent variable function as the following, to describe this plot and use it in our simulations. The outcome formula is given by:

$$E_{z,max} = 1000e^{-[\frac{\theta-35.2(0.75-\lambda)}{1+10(0.75-\lambda)}]^2}[44.026(1/\lambda)^3 - 210.24(1/\lambda)^2 + 327.26(1/\lambda) - 163.63] \tag{5.7}$$

Photo-Luminescence frequency ω_0 for CdSe/ZnS has been measured experimentally to be around 630 nm [28], and the ones that we purchased had its maximum intensity PL at around 618 nm [2]. The loss factor is also assumed to be small and with the order of 10^{13} Hz. So parameters and variables needed to simulate SPR-QDs in COMSOL are now figured out. Figure 5.6 shows the meshed unit block of our structure. The top layer is the 1.7847 index prism. A gold film with 48 nm thickness is located underneath of this prism and itâĂŹs in touch with air which includes the thick layer at the bottom of the unit. Floquet periodic condition is applied to vertical faces of this block, while the incidence light

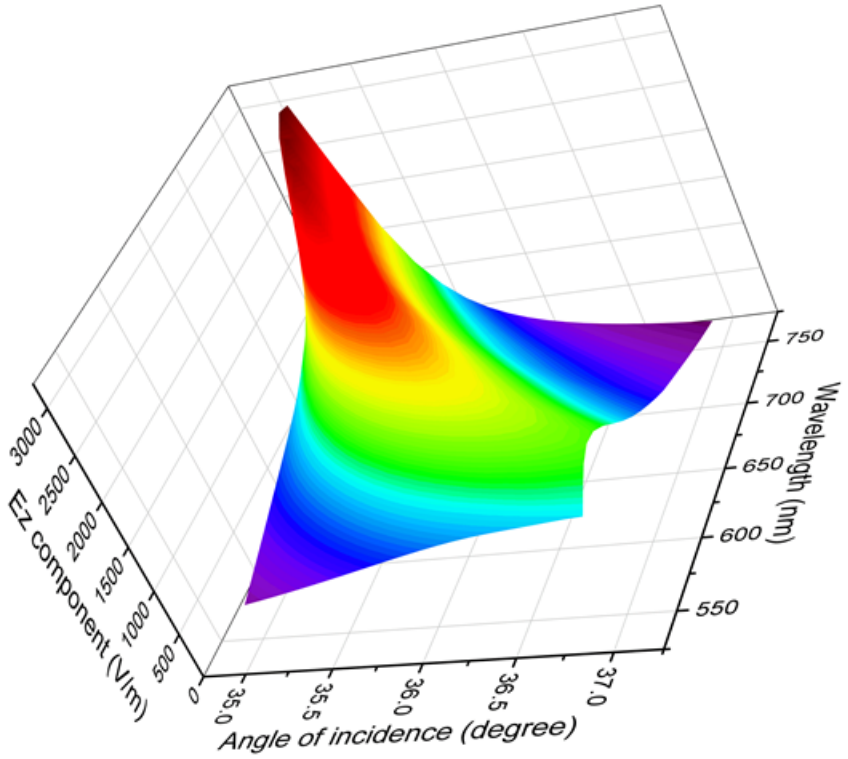

Figure 5.5. Maximum electric field amplitude on gold surface at a range of angles.

is approaching from the top face with some angle with respect to normal, and transmitted light is collected from the bottom face.

Quantum dots, treated as emitters, are located in 10nm proximity of the gold film and also in 10nm distance with respect to each other. For them, COMSOL needs electric current dipole momentâĂŹs magnitude and direction. For direction we already decided to ignore the x-component and focus on z-direction as itâĂŹs much stronger in magnitude. Also what we figured in the previous section was the magnitude of electric dipole moment which is a static quantity. In order to generalize it to the dynamic case, we multiply this by the frequency f that it changes over time to get the dynamic quantity of electric current dipole moment and we call it here ECDM.

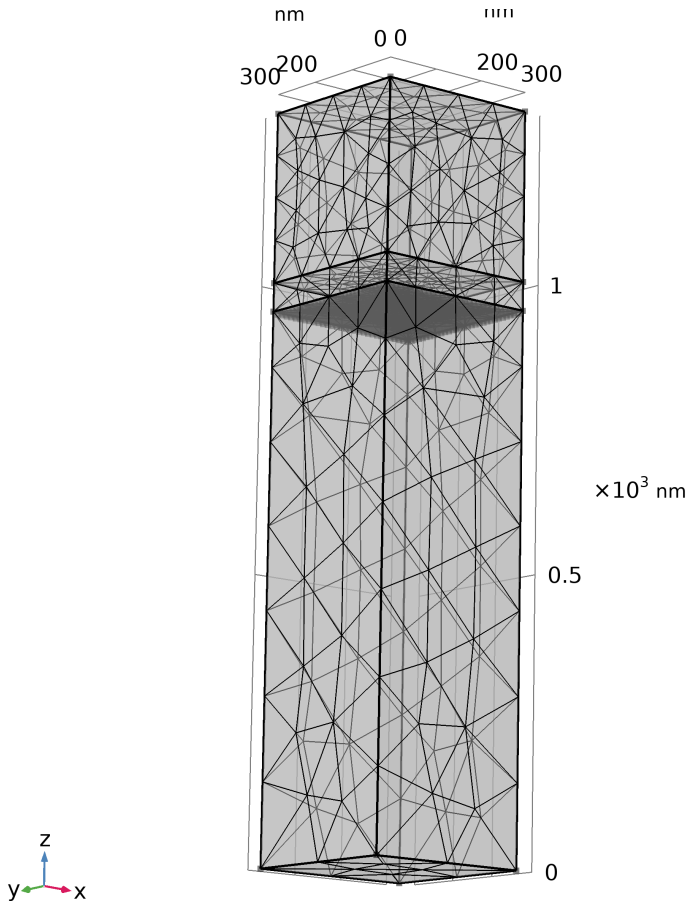

Figure 5.6. Meshed structure of SPPs-QDs coupling.

The coupling strength here between SPPs electric field and QDs shows up in the number of electrons inside QD that are engaged in oscillations and emission. A factor N is inserted in front of electric current dipole moment to represent the coupling:

$$ECDM = \frac{Ne^2}{m} \frac{Ef}{\omega_0^2 - \omega^2 + i\gamma\omega,} \tag{5.8}$$

For the case of $N = 0$ or no QD, the simulation is run for reflectance vs. angle of incidence, for the above mentioned structure; and it would result in part (a) of Figure 5.7. The next sections of this figure correspond to $N = 10, 20,\& \ 30$.

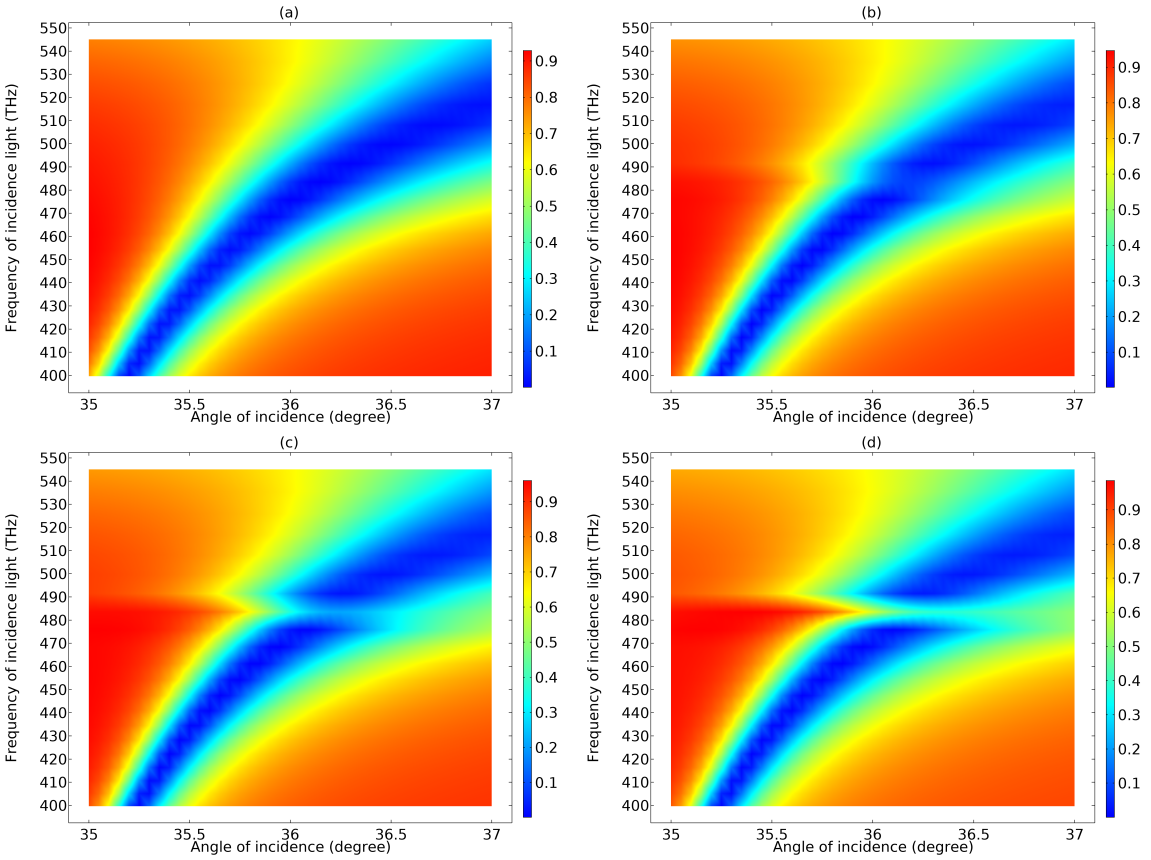

Figure 5.7. Number of emitters, N=0 (a), N=10 (b), N=20 (c), and N=30 (d) in each QD on gold sensor.

As the number of electrons involved in the coupling increases we see a more pronounced splitting in these curves, which is known as Rabi splitting. The width of this splitting is a factor of coupling strength. In part (d) of the figure 5.7, we see splitting of about 10 THz which corresponds to the energy shift of 40 meV.

Similar process is gone through for 50 nm silver replacing gold but keeping the same arrangement of quantum dots and the results show a much more pronounced splitting with less number of emitters, see Figure 5.8

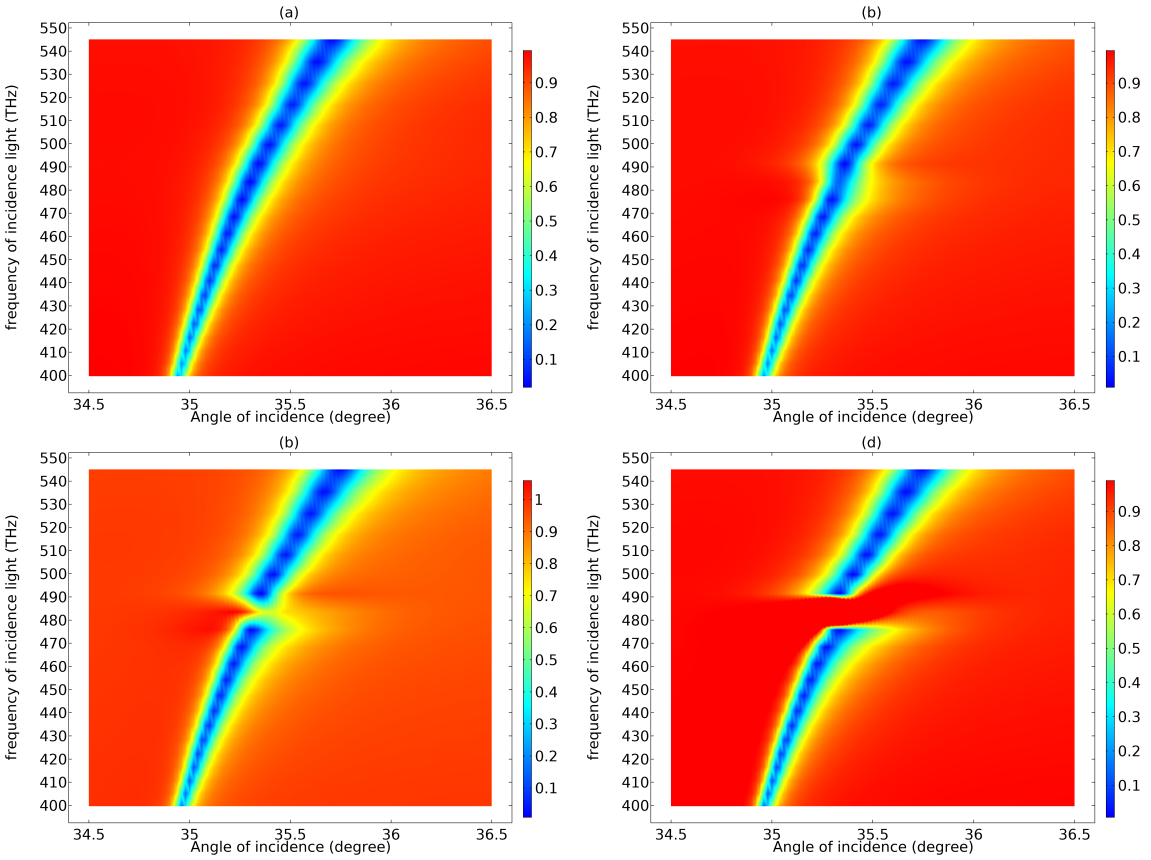

Figure 5.8. Number of emitters, N=0 (a), N=5 (b), N=10 (c), and N=20 (d) in each QD on silver sensor.

5.3 Data on QDs

Experimental setup for PL data of QDs which are taken by previous graduate student in our group, Kunal Tiwari, is shown schematically in Figure 4.3. Working with He-Ne laser with 632.8nm wavelength and creating surface plasmons on 48nm thick gold film, we ran an experiment to investigate SPPs-QD coupling. Covering the surface of the same gold film with CdSe/ZnS quantum dots and creating SPR condition by this red laser that reaches the sample from the bottom through the prism, would allow us to study SPR effect on QDs. At the same time a 514nm green laser hitting from air and top side on gold film at the same spot that QDs are located. The incoming direction of this laser is fixed and its

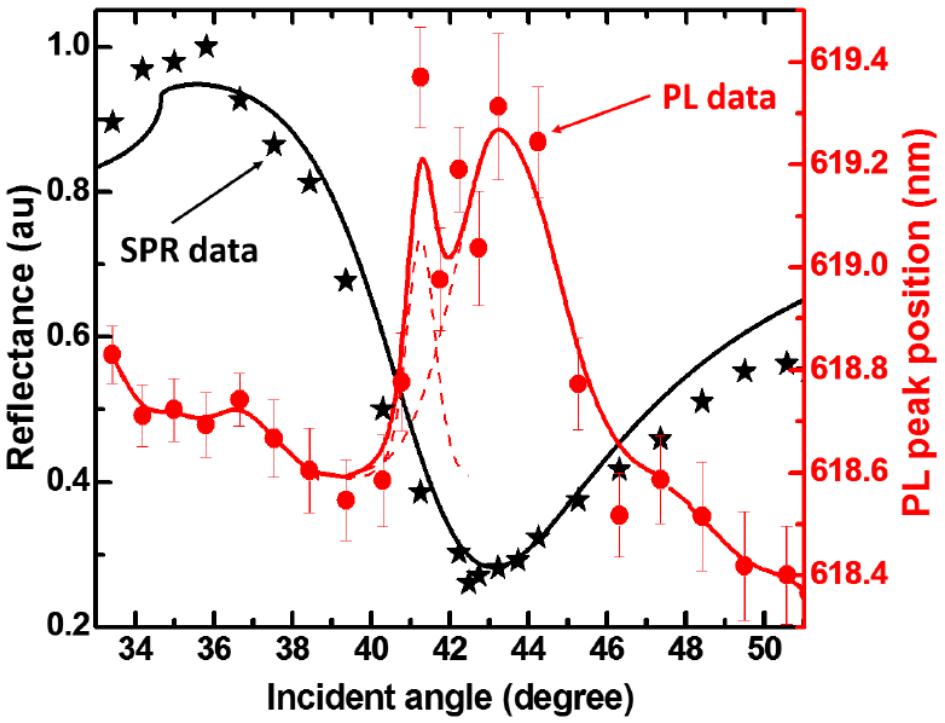

Figure 5.9. SPR and PL curve for QD thin film coated at the Bi-WC SPR sensor.

reflected beam is guided through a spectrometer. In no coupling case or before SPR angle which is at $\theta_{in} = 43^\circ$ for red laser in this case, these quantum dots absorb a broadband light spectrum and instead emit mainly a red light with Gaussian distribution around that is centered at ~ 618.7 nm. By getting close to SPR angle, this wavelength suddenly shifts in value and jumps to ~ 619.3 nm, see Figure 5.9. [29]

This jump corresponds to the energy shift of $\simeq 2meV$ is obviously due to the change in band gap of QDs and could be explained using Stark effect, here caused by evanescent waves created at SPR angle, as it's been suggested in some articles. According to formula (23) of this paper [30], the shift in the wavelength based on the stark effect, has quadratic dependence on electric field.

$$EnergyShift = \frac{-9}{4}\epsilon_2 a_{ex}^3 E^2 \tag{5.9}$$

According to this reference, and above mentioned formula, in which ϵ_2 (relative permittivity) and $a_{ex} = \epsilon_2 \hbar^2 / \mu e^2$ (Bohr radius of exciton in a semiconductor), depend on specific type of QD. For typical values of a_{ex} & ϵ_2, and electric fields in the order of $1keV$ or so, the shift in the band gap energy is usually about a few meV which is consistent with our measurements. Of course by increasing the strength of electric field, this shift is predicted to grow larger and we can check that by running this experiment by another type of our sensors which has significant difference in the maximum value of electric field at SPR angle. One good option here could be the use of silver sample, as its E-field according to simulations is double amount of gold sample.

6

Highly Efficient Sunlight Absorber

6.1 Previous Studies on Sunlight Absorbers

Metamaterials that can absorb broadband sunlight with high absorption efficiency without suffering loss in light absorbance for different polarizations and angle of incidence are important for thermophotovoltaic applications. An additional requirement for an ideal thermophotovoltaic absorber is that its performance does not deteriorate at high temperatures. Numerous metamaterial nanostructures have been proposed with absorption efficiencies in the range of approximately 70%-90% for limited bandwidths of the solar spectrum. [31–40]

In recent years, refractory plasmonic metamaterials have emerged as important materials for energy applications. [41–47] In this regard, titanium nitride (TiN) is an attractive building block for thermophotovoltaic applications because of its high melting point ($2930^{\circ}C$), plasmonic resonance in the visible (VIS)-to-near-infrared (NIR) range, chemical stability, and compatibility with CMOS fabrication. [47–52]

For example, Chirumamilla et al. have studied the feasibility of 3D TiN pillar-based ultra-broadband absorbers for high temperature applications. [51] Through computer simulations, they observed a polarization independent average absorption of 94% over a 300-2300 nm wavelength range for 320 nm diameter and 1500 nm high TiN nanopillars. Similarly, Wang et al. obtained a light absorption of 93% over a 300-900 nm wavelength range by using TiN-nanopatterns/dielectrics/TiN stack metamaterials. [46]

In another study, COMSOL Multiphysics computer simulations by Li et al. obtained absorption exceeding 87% with an average integrated absorption of about 95% over the visible range [47]. Liu et al. have performed computer simulations by using the 3D finite-difference time-domain method for a structure composed of a periodic TiN disk array coated with a 220 nm diameter and 50 nm thick TiO2 disk array patterned on a 50 nm thick SiO_2 film on a 100 nm thick TiN opaque substrate. They observed a solar weighted absorptivity of 93% with 1110 nm spectral bandwidth over the UV-VIS-NIR range. [50]

6.2 Suggested Design For The Maximum Absorption

In this section, we talk about a design of new CMOS-compatible metamaterial nanostructure and study its performance as a broadband solar energy absorber by utilizing the COMSOL Multiphysics software. [14] Our metamaterial nanostructure provides an impressive value of 98% for absorption efficiency integrated over the broadband wavelength range of the solar spectrum from 250 nm to 1100 nm. To our knowledge, solar absorp-

tion by the proposed metamaterial is the highest for a broad range of wavelength from 250 nm to 1100 nm. Additionally, the incorporation of an excellent high-temperature dielectric hafnium-dioxide (HfO_2) adds to the functionality of the absorber at high temperatures. [20]

A unit cell of one of the metamaterial nanostructures is sketched in Figure 6.1. It is composed of a $300nm \times 300nm \times 100nm$ TiN base covered with 60-nm thick SiO_2. A TiN disk of 90 nm radius and 50 nm height sits over the SiO_2 dielectric and is capped with another disk of a high-temperature dielectric (HfO_2) of 90 nm radius and 30 nm height. A set of six 10 nm radius Au NPs is implanted symmetrically in the near surface region of HfO_2.

A periodic array of such unit cells, with a periodicity of 300 nm, covers the entire surface of the underlying solar panel. The bottom layer of the unit cell (TiN) provides Ohmic contact through which absorbed energy is transmitted to the solar panel. Because of CMOS compatibility and outstanding optical and physical properties, the HfO_2 dielectric is of particular interest. [53–56] For example, its optical transparency over a wide range of wavelengths from 250 nm to 2000 nm, high density (9.68 g/cm^3), chemical stability, and high melting point ($2758°C$) make it an ideal dielectric for high temperature solar absorbers. We have recently observed superior performance of HfO_2 as a dielectric for high sensitivity waveguidecoupled surface plasmon resonance sensors. [17, 20]

6.3 COMSOL Simulations on Absorption Efficiency

A mesh used for the simulations presented in this work is sketched in Figure 6.2. It is a physics controlled extra fine mesh of a free triangular type, in which COMSOL determines the concentration of the elements according to values of the refractive indices and dimensions of the materials. Obviously, the mesh is the smallest unit. Periodic boundary conditions are imposed on the x-z and y-z sides. Light is incident from the top through

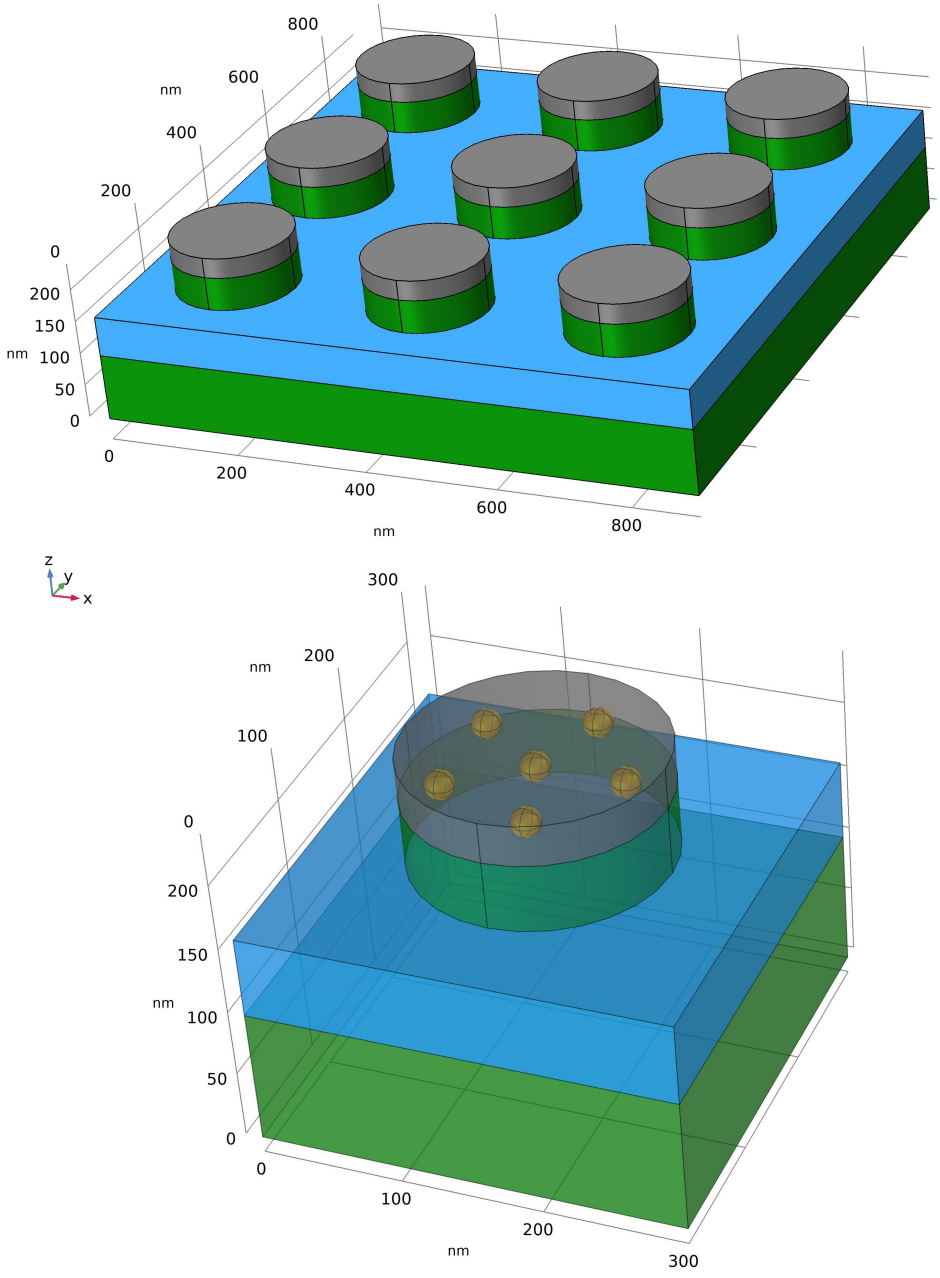

Figure 6.1. Top - the metamaterial structure containing TiN/SiO_2/TiN disks/HfO_2disks. Bottom - a unit cell containing six Au NPs.

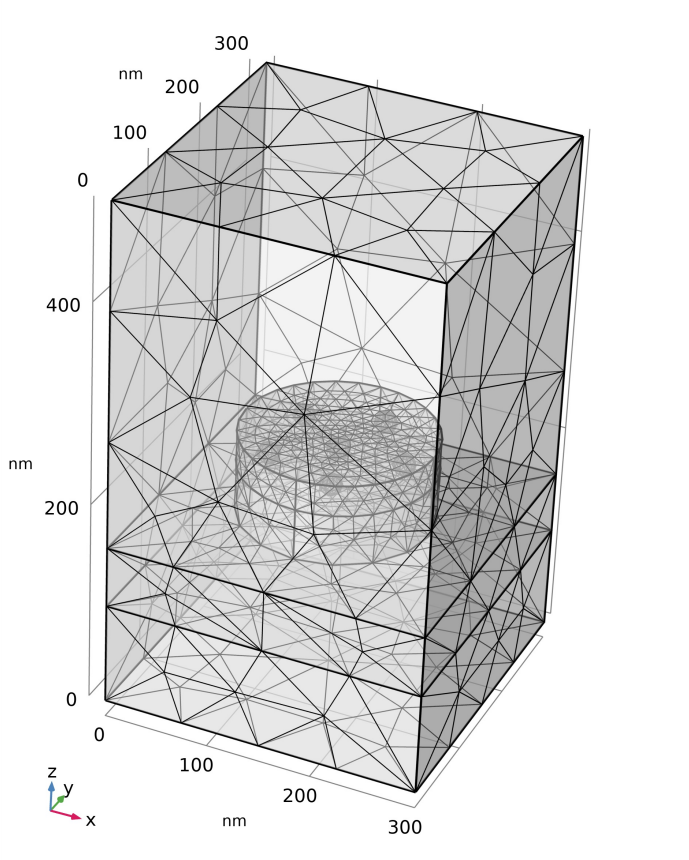

Figure 6.2. Physics controlled fine mesh of a free triangular type used in COMSOL simulations.

a designated periodic port. A second port is added at the bottom of the cube to transmit absorbed energy to the underlying solar panel.

The radius and height of each one of the top disks (TiN and HfO_2) are optimized to yield the highest absorption coefficient. Figure 6.3 shows the wavelength dependence of the absorption coefficient for different radii of the TiN disk. Out of all the simulations which yielded an absorption coefficient higher than 90% for wavelengths ranging from 0.25μm to 1.1 μm, the 90 nm radius disk provides the highest absorption.

An absorber nanostructure having the optimized disk, in conjunction with 50 nm high TiN and 30 nm high HfO_2, provides the best results. Figure 6.4 shows changes in absorption

for three different values of the height of the TiN disk. Whereas the nanostructure with 60 nm thick TiN yields higher absorption for wavelengths ranging from about 0.3μm to 0.6μm, it is the structure with 50 nm thick TiN which performs better for higher wavelengths.

As shown in Figure 6.5, absorption is sensitive to SiO_2 thickness. For these simulations, only the thickness of SiO_2 was varied from 50 nm to 70 nm while keeping all other parameters of the structure fixed at the described optimized values of TiN and HfO_2. The structure with 50 nm thick SiO_2 provides the highest absorption of up to about 0.5μm. In the mid-wavelength range from about 0.6 to 0.75μm, the structure having 70 nm thick SiO_2 yields the highest absorption. For longer wavelengths, the structure with 60 nm thick SiO_2 yield the highest absorption. The final optimized metamaterial nanostructure consists of a $300nm \times 300nm \times 100nm$ TiN base covered with 60 nm thick SiO_2. A 50 nm high and 90 nm radius TiN disk is placed over the SiO_2 dielectric. The TiN disk is capped with another disk of an HfO_2 dielectric. Six Au NPs, each of 10 nm radius, are accommodated symmetrically over the HfO_2 disk.

The results presented in this section are obtained for the final optimized structure of the absorber. Figure 6.6, shows absorption for vertical incidence ($\theta = 0$) as a function of wavelength of the solar spectrum for three different configurations of the unit cell:

1. An optimized unit cell, as shown in Figure 6.1, having symmetrically arranged six 10 nm radius Au NPs,
2. The same unit cell except the fact that this unit cell contains four, rather than six, Au NPs,
3. The same unit cell without any Au NPs.

In all three cases, it is remarkable that absorption remains higher than 93% for the entirerange of the wavelengths from 250 nm to 1100 nm. The upper range of the wavelength is chosen keeping in view the energy bandgap of the silicon solar panel. These data clearly show that doping the unit cell with Au NPs results in a very significant enhancement in

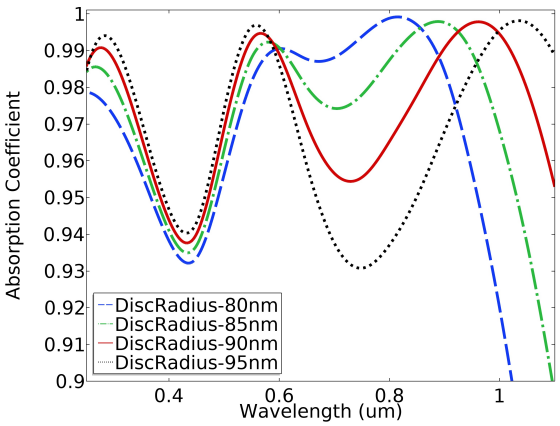

Figure 6.3. Optimization of disk's radius.

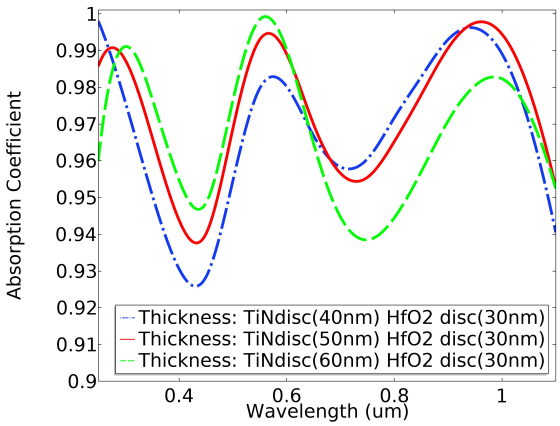

Figure 6.4. Optimization of TiN disk's thickness.

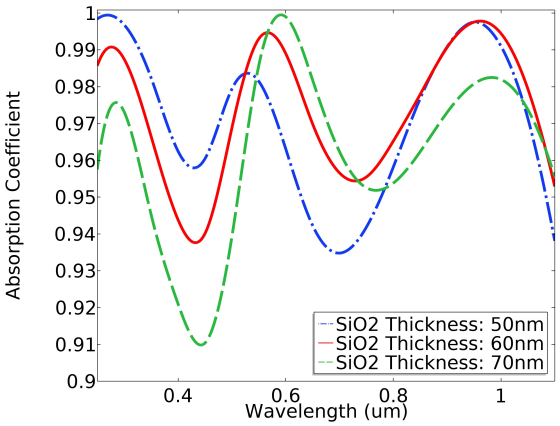

Figure 6.5. Optimization of SiO_2 layer's thickness.

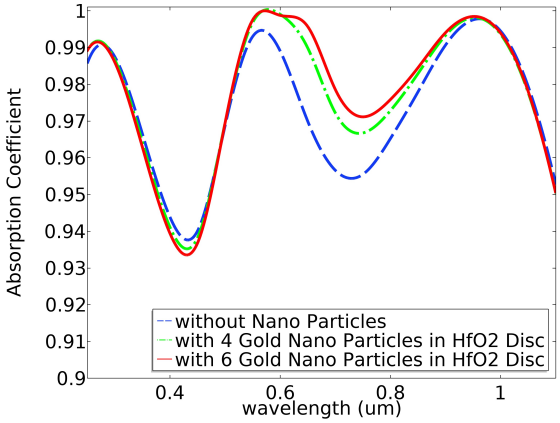

Figure 6.6. Optimization by doping with Au NPs.

absorption at wavelengths ranging from 500 nm to 950 nm. This finding is consistent with the well-established results that the excitation of localized surface plasmon resonance in Au NPs enhances optical properties of materials. [17, 57–69] However, the wavelength dependence of the relative change in absorption is different from the wavelength dependence of absorption by NPs themselves.

It is well-known that absorption by 10 nm Au NPs peaks at around 510 nm and decreases precipitously at higher wavelengths, approaching zero at about 700 nm. [70] In contrast and as seen in Fig. 6, addition of Au NPs to the unit cell enhances absorption in such a manner that the relative change in absorption reaches maximum at a much higher

wavelength of 670 nm and continues being significant up to about 900 nm. Although the increase in absorption is due to the addition of the NPs, the process by which absorption is enhanced appears significantly different from simple absorption of light by the NPs. An understanding of the precise nature of the mechanism behind this difference awaits additional research.

6.4 Calculations Using Sun Spectrum on Earth

Figure 6.7 compares the solar spectrum on Earth, with water absorption bands around 0.75 μm and 0.95 μm, and the absorption by our optimized metamaterial. The absorption by our optimized metamaterial of almost all the visible solar spectra, that is useful for silicon thermophotovoltaics, is impressive; the magnitude of the largest difference is less than 6% around 0.45 μm. Not only does this metamaterial exhibit exceedingly high absorption efficiency ($\sim 98\%$ integrated absorption for normal incidence), it also exhibits near-independence from the angle of incidence over a wide range of angles as well as from polarization of sunlight.

6.5 Indirect Light Absorption

How the absorption changes as functions of the wavelength of the incident light and the angle of incidence for both p- and s-polarizations of sunlight? This question is answered in Figures 6.8 and 6.9. It is remarkable that for both polarizations, the absorption coefficient is predominantly higher than 95% for wavelengths from 0.3 μm to 1.10 μm and for incident angles from zero (normal incidence) to 60°. At lower angles of incidence $(0^\circ - 35^\circ)$, there are two narrow bands from about 0.37 μm to 0.47 μm and from about 0.72 μm to 0.76 μm, where absorption is only slightly lower but remains higher than 92% or so.

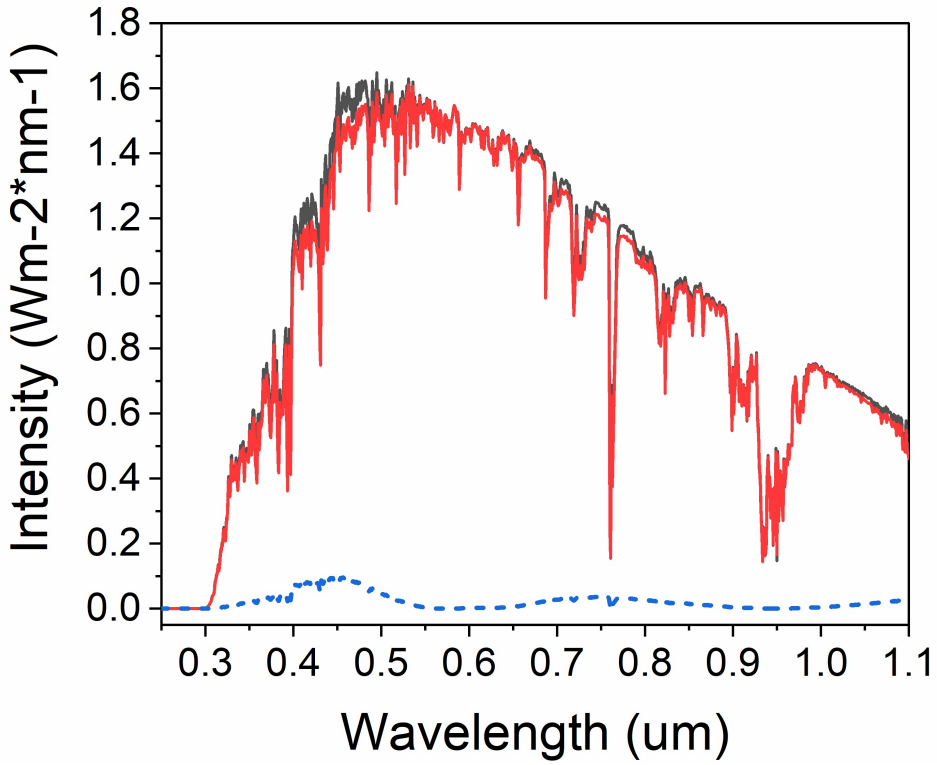

Figure 6.7. The solar optical spectrum on Earth (black), absorption by the optimized metamaterial (red), and difference between the solar spectrum and absorption by the metamaterial (dashed blue).

For higher angles, absorption is lower within narrow bands: one around 0.7 μm and the other above 1 μm. Between 45° and 60°, absorption decreases but remains above 85% for both polarizations, except for small range of wavelengths shown by blue shadows.

If the orientation of a solar panel (for example, in the case of a solar panel mounted on a spaceship) can be adjusted continuously such that the sunlight falls upon it vertically, the proposed metamaterial will absorb remarkably 98% of the incident visible energy.

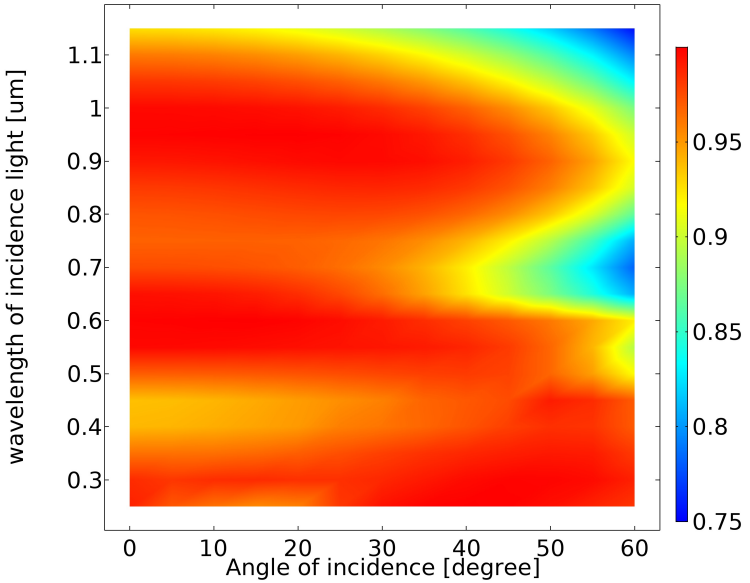

Figure 6.8. Absorption for different angles, p-polarized light.

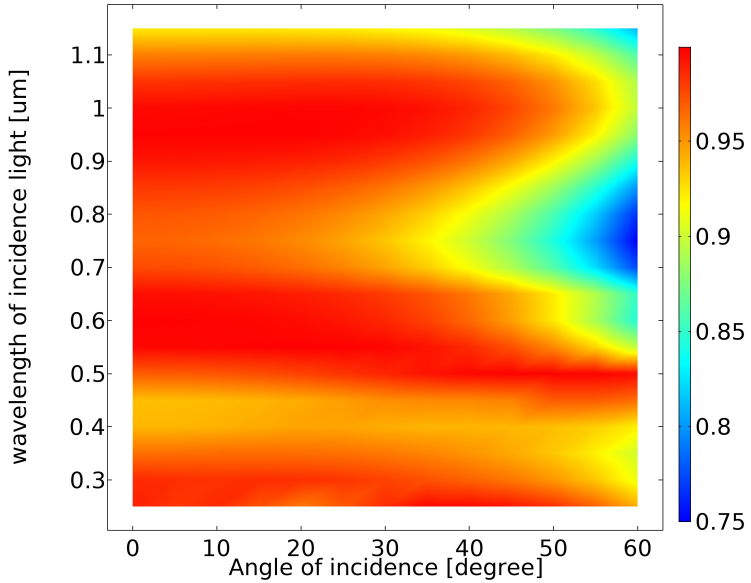

Figure 6.9. Absorption for different angles, s-polarized light.

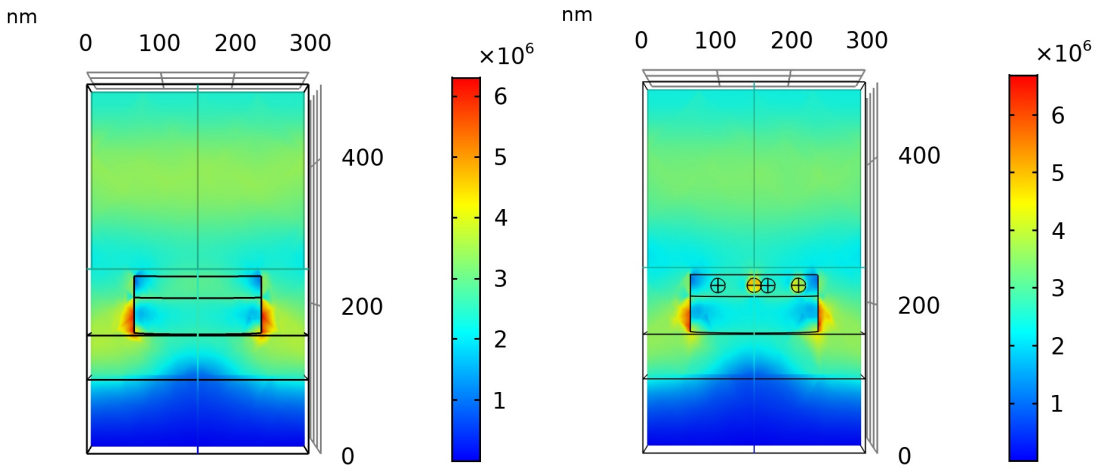

Figure 6.10. Evanescent electric fields present in two metamaterial nanostructures: one without Au NPs (left) and another with Au NPs embedded in the material (right).

6.6 Electric Field Strength

As discussed, the incorporation of Au NPs into the nanostructure increases absorption by the metamaterial primarily because of the excitation of the localized surface plasmon resonance. In this context, it is interesting to examine the evanescent fields associated with these excitations. [17] Toward this, we show in Figure 6.10 evanescent electric fields present in two metamaterial nanostructures: one without Au NPs and another with Au NPs embedded in the material. In both cases, p-polarized light of wavelength Îż = 0.500 μm is incident normally along the z-axis.

Figure shows field distributions in the xâĂŞz plane of the structures (the plane of incidence). In the absence of Au NPs, the resonant field is concentrated mostly around the edges of the periodic array of TiN disks. The resonant field at the edges of the disk is about 6×10^6 V/m for 1 mW incidence power and decays exponentially from the edge of the disk with a decay length of approximately 0.05 μm. Not only does inclusion of the above-described Au NPs enhance absorption, it also modifies the resonant field and its distribution in the nanostructure because of localized surface plasmons around Au NPs. [17,20,57] The

data in Figure 6.10 (right) clearly show the concentration of the resonant field around Au NPs, as well as enhanced field distributions at and near the edges of the TiN disks.

Once again, the field around the edges of the disk decays exponentially from the edge of the disk with a decay length of nearly 0.025 μm. These fields are the highest at the interface between the metal (for example, TiN) and the dielectric in the nanostructure without Au NPs.

As stated, the fields decay exponentially with increasing distance from the interface. When Au NPs are present in the structure, localized surface plasmons are excited at the interface between Au NPs and surrounding the dielectric, and this gives rise to much higher evanescent electric fields, as shown in Figure 6.10. This is reinforced by the previous simulations, where the presence of the Au NPs in the structure further enhances absorption of sunlight because of localized surface plasmons at the metal/dielectric interface in the material.

Our choice of HfO_2 as an excellent high-temperature dielectric for the proposed metamaterial nanostructure, compared to another CMOS compatible dielectric (Si_3N_4), is supported by the data shown in Figure 6.11. Here, we examine the changes in the relative absorption for a structure in which the HfO_2 disk is replaced by a Si_3N_4 disk.

We define relative absorption by

$$R_A = \frac{A_1 - A_2}{A_2},$$

where A_1 and A_2 are the absorptions by metamaterial structures having HfO_2 and Si_3N_4 disks, respectively. Si_3N_4 is also an excellent CMOS-compatible dielectric with optical transparency from ultraviolet to infrared (250-900 nm), a relatively large refractive index ($1.91@\lambda = 632.8nm$), thermal stability, and good insulating properties. [19, 71, 72]

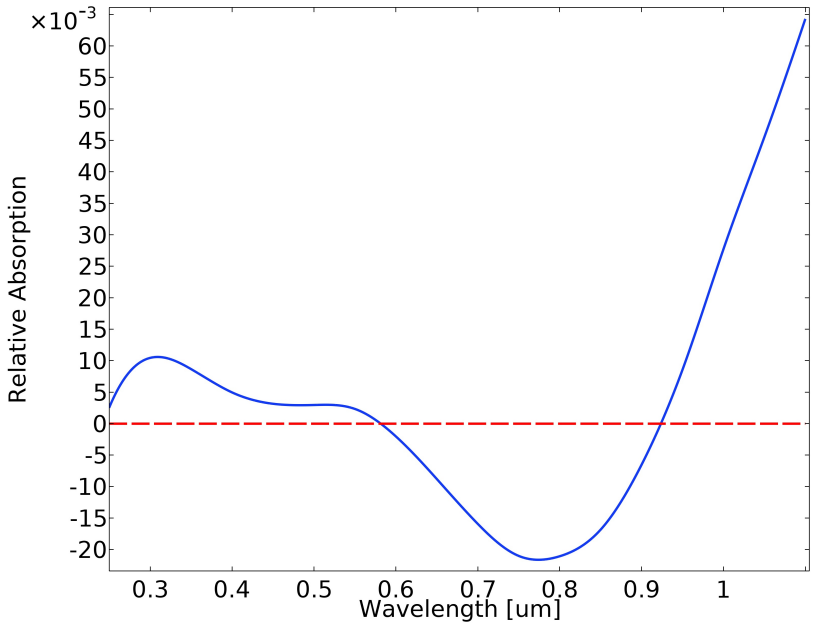

Figure 6.11. Relative absorption for disks using Si_3N_4 and HfO_2.

It is widely used by the microelectronics industry as oxidation masks, protection and passivation barriers, gate dielectrics, etc., using the procedure outlined above. These data show that the metamaterial structure with the HfO_2 disk performs better as an absorber of sunlight for wavelengths from 250 nm to about 600 nm and much better in the near IR range of wavelengths from about 900 nm to 1100 nm. From about 600 nm to about 900 nm, the metamaterial having the Si_3N_4 disk outperforms the structure with the HfO_2 disk.

7

Conclusions and Future Work

Surface plasmons are a powerful and important phenomenon with applications in medical and biophysics as an extremely powerful sensors. The focus of this dissertation was mainly on how we can improved the structure of these sensor, operating them in the region that give us the highest sensitivity and simulate the strength of evanescent field that they create.

Optimized cases for both Kretschmann and grating structures show that the SPR signal is the best for Kretschmann configuration and it can be even improved if we go to multilayer structures combining metals and waveguide. Depending on the index of material we want to detect, we need to choose specific value of the prism index and thickness of

Figure 7.1. M-UTR80 rotation stage by Newport™.

metal. Doing so can give us sensitivities of around 200 degrees that makes these structures a good candidate for applications in biology and medical detectors.

For future work, we have several plans that can be run simultaneously. Fist could be the study of temperature effect on the quality of SPR signal. Primary simulations by COMSOL shows that in general the signal gets enhanced by going to lower temperature as it intuitively makes sense since at lower temperatures resistance of the metals becomes even lower and surface charges can move more freely.

Another project could be to study and test the effect on SPR on catalytic properties of copper sensor, when exposed to certain chemical and biological interactions. We've already made measurements on single Cu and $Ag/Si_3N_4/Cu$ sensor and they both show good SPR effect, especially the results with stack configuration is promising and the signal is pretty good. So we can move forward with providing this condition at the same time that a chemical interaction is happening at the presence of copper surface as a catalyst.

In addition we saw that due to lack of precision in angle measurements, we weren't able to detect concentration of glucose for lower than 1%, but by enhancing our setup by

purchasing a more sophisticated rotation stage, e.g. Figure 7.1, we can detect the change in concentration as much as 0.02% which would be enough to for example identify the change in glucose level of blood in a short period of time and in a very cheap and reliable way.

And at last, we are capable of testing the results of simulations for the interaction between surface plasmons and QDs for gold sample. This experiment includes using a white light that provides the wavelengths from 400 to 700 nm and by using this light as the source to generate surface plasmons. Through the interaction with QDs we can determine whether there is going to be a single or double minimum in the reflection off of gold sensor, which specific Quantum dots are located on top of it.

REFERENCES

[1] A. K.Singh, and S.C. Sharma. A fixed detector kretschmann configuration optical system to study surface plasmon excitations. *Optics $ Laser Technology*, 56:256–262, 2014.

[2] K. Tiwari. Bimetallic-waveguide coupled sensors for tunable plasmonic devices. `http://hdl.handle.net/10106/25938`.

[3] Hamish Johnston. `http://www.taopatch.com/blog/quantum-dots-\entangled-with-single-photons/`.

[4] D. Ioannou, and D. Griffin. Nanotechnology and molecular cytogenetics: the future has not yet arrived. *Nano Reviews*, 1:5117, 2010.

[5] Heinz Raether. *Surface plasmons on smooth and rough surfaces and on gratings*. Springer Tracts in Modern Physics, 1988.

[6] K. Welford. Surface plasmon-polaritons and their uses. *Opt Quant Electron*, 23:1–27, 1991.

[7] R. H. Ritchie. Plasma losses by fast electrons in thin films. *Phys. Rev.*, 106:874, 1957.

[8] P. Drude. Zur elektronentheorie der metalle. *Annalen der Physik*, 306(3):566–613, 1900.

[9] J.J.Quinn. Bulk and surface plasmons in solids. *Nuclear Instruments and Methods in Physics*, 96(3-4):460–464, 1995.

[10] Stephen Gasiorowicz. *Quantum Physics*. Wiley, 0471057002, 2003.

[11] Steven J. Byrnes. Multilayer optical calculations. *arXiv [physics.comp-ph]*, 2019.

[12] Donald M. Mattox. *Handbook of Physical Vapor Deposition (PVD) Processing*. ELSEVIER, 9780815520375, 2010.

[13] Stephen A. Campbell. *Fabrication Engineering at the Micro- and Nanoscale*. Oxford University Press, 0199861226, 9780199861224, 2013.

[14] COMSOL, 2018. `https://www.comsol.com/comsol-multiphysics`.

[15] E. Kretschmann. The determination of the optical constants of metals by excitation of surface plasmons. *Z. Phys.*, 241:313, 1971.

[16] A. Otto. Excitation of nonradiative surface plasma waves in silver by the method of frustrated total reflection. *Z. Phys.*, 216:398, 1968.

[17] S. C. Sharma. *Advances in Sensors: ReviewsâĂŹ Book Series, edited by S. Y. Yurish*. IFSA Publishing, Barcelona, Spain, Vol.25, 2018.

[18] K. Tiwari and S.C. Sharma. plasmon based sensor with order-of-magnitude higher sensitivity to electric field induced changes in dielectric environment at metal/nematic liquid-crystal interface. *Sensors and actuators. A. Physical.*, 216:128–135, 2014.

[19] K. Tiwari, S. C. Sharma, and N. Hozhabri. High performance surface plasmon sensors: Simulations and measurements. *J. Appl. Phys.*, 118(9):093105, 2015.

[20] K. Tiwari, S. C. Sharma, and N. Hozhabri. Hafnium dioxide as a dielectric for highly-sensitive waveguide-coupled surface plasmon resonance sensors. *AIP Adv.*, 6(4):045217, 2016.

[21] Nguyen, H.H.; Park, J.; Kang, S.; Kim, M. Surface plasmon resonance: A versatile technique for biosensor applications. *Sensors*, 15:10481–10510, 2015.

[22] Victoria S. Application of surface plasmon resonance (spr) for the detection of single viruses and single biological nano-objects. *J Bacteriol Parasitol*, 3:e110, 2012.

[23] Y. Meng, H. Ma, J. Wang, Y. Li, Z. Li, and S. Qu. Broadband spoof surface plasmon polaritons coupler based on dispersion engineering of metamaterials. *Appl. Phys. Lett.*, 111:151904, 2017.

[24] S. Pillai, K. R. Catchpole, T. Trupke, and M. A. Green. Surface plasmon enhanced silicon solar cells. *J. Appl. Phys.*, 101:093105, 2007.

[25] R. Bakhtiar. Surface plasmon resonance spectroscopy: A versatile technique in a biochemistâĂŹs toolbox. *J. Chem. Educ.*, 90:203–209, 2013.

[26] L. Novotny. Strong coupling, energy splitting, and level crossings: A classical perspective. *American Journal of Physics*, 78:1199, 2010.

[27] P TÃűrmÃd' and W L Barnes. Strong coupling between surface plasmon polaritons and emitters: a review. *Rep. Prog. Phys.*, 78:013901, 2015.

[28] D. Ioannou, and D. Griffin. Fabrication of cdse/zns quantum dots thin film by electrohydrodynamics atomization technique for solution based flexible hybrid oled application. *Chemical Engineering Journal*, 253(1):352–331, 2014.

[29] K. Tiwari, S. C. Sharma, H. Akafzade, N. Hozhabri. Energy exchange between surface plasmon polaritons and cdse/zns quantum dots. *arXiv:2007.04090*, 2020.

[30] S. I. Pokutnyi, L. Jacak, J. Misiewicz, W. Salejda, and G. G. Zegrya. Stark effect in semiconductor quantum dots. *Journal of Applied Physics*, 96:1115, 2014.

[31] A. Hubarevich, A. Kukhta, H. V. Demir, X. Sun, and H. Wang. Ultra-thin broadband nanostructured insulator-metal-insulator-metal plasmonic light absorber. *Opt. Express*, 23(8):9753, 2015.

[32] A. Kukhta, A. Hubarevich, H. Wang, X. Sun, and H. Demir. Physics, chemistry and applications of nanostructures: Reviews and short notes. *World Scientific Publishing Co.*, page 222, 2013.

[33] Z. Q. Liu, X. S. Liu, S. Huang, P. P. Pan, J. Chen, G. Q. Liu, and G. Gu. Automatically acquired broadband plasmonic-metamaterial black absorber during the metallic film-formation. *ACS Appl. Mater. Interfaces*, 7(8):4962, 2015.

[34] K. Aydin, V. E. Ferry, R. M. Briggs, and H. A. Atwater. Broadband polarization-independent resonant light absorption using ultrathin plasmonic super absorbers. *Nat. Commun*, 2:517, 2011.

[35] E. Unal, M. Bagmanci, M. Karaaslan, O. Akgol, and C. Sabah. Strong absorption of solar energy by using wide band metamaterial absorber designed with plus-shaped resonators. *Int. J. Mod. Phys. B*, 32(25):1850275, 2018.

[36] M. Bagmanci, M. Karaaslan, E. Unal, O. Akgol, M. Bakir, and C. Sabah. Strong absorption of solar energy by using wide band metamaterial absorber designed with plus-shaped resonators. *Int. J. Mod. Phys. B*, 33(8):1950056, 2019.

[37] P. Rufangura and C. Sabah. Perfect metamaterial absorber for applications in sustainable and high-efficiency solar cells. *J. Nanophotonics*, 12(2):26002, 2018.

[38] P. Yu, L. V. Besteiro, Y. J. Huang, J. Wu, L. Fu, H. H. Tan, C. Jagadish, G. P. Wiederrecht, A. O. Govorov, and Z. M. Wang. Broadband metamaterial absorbers. *Adv. Opt. Mater*, 7(3):1800995, 2019.

[39] S. Mehrabi, M. H. Rezaei, and A. Zarifkar, 36(9), 2602 (2019). Ultra-broadband solar absorber based on multi-layer tin/tio$_2$ structure with near-unity absorption. *J. Opt. Soc. Am. B*, 36(9):2602, 2019.

[40] Q. Ni, H. Alshehri, Y. Yang, H. Ye, and L. P. Wang. Plasmonic light trapping for enhanced light absorption in film-coupled ultrathin metamaterial thermophotovoltaic cells. *Front Energy*, 12(1):185, 2018.

[41] S. M. Choudhury, D. Wang, K. Chaudhuri, C. DeVault, A. V. Kildishev, A. Boltasseva, and V. M. Shalaev. Material platforms for optical metasurfaces. *Nanophotonics*, 7(6):959, 2018.

[42] S. Venkataramanababu, G. Nair, P. Deshpande, M. A. Jithin, S. Mohan, and A. Ghosh. Chiro-plasmonic refractory metamaterial with titanium nitride (tin) coreâĂŞshell nanohelices. *Nanotechnology*, 29(25):255203, 2018.

[43] B. B. Wu and J. G. Wang. Polarization-insensitive,wide-angle broadband perfect absorber with patch structures. *Optoelectron. Adv. Mater.âĂŞRapid Commun.*, 12(7-8):417, 2018.

[44] D. W. Huo, J. W. Zhang, H. Wang, X. X. Ren, C. Wang, H. Su, and H. Zhao. Broadband perfect absorber with monolayer mos_2 and hexagonal titanium nitride nano-disk array. *Nanoscale Res. Lett.*, 12:456, 2017.

[45] D. Y. Jiang and W. M. Yang. Refractory material based frequency selective emitters/absorbers for high efficiency and thermal stable thermophotovoltaics. *Energy Mater. Sol. Cells*, 163:98, 2017.

[46] H. C. Wang, Q. Chen, L. Wen, S. C. Song, X. Hu, and G. Q. Xu. Titanium-nitride-based integrated plasmonic absorber/emitter for solar thermophotovoltaic application. *Photonics Res.*, 3(6):329, 2015.

[47] W. Li, U. Guler, N. Kinsey, G. V. Naik, A. Boltasseva, J. G. Guan, V. M. Shalaev, and A. V. Kildishev. Refractory plasmonics with titanium nitride: Broadband metamaterial absorber. *Adv. Mater.*, 26(47):7959, 2014.

[48] P. Patsalas, N. Kalfagiannis, and S. Kassavetis. Optical properties and plasmonic performance of titanium nitride. *Materials*, 8(6):3128, 2015.

[49] G. V. Naik, J. L. Schroeder, X. J. Ni, A. V. Kildishev, T. D. Sands, and A. Boltasseva. Material platforms for optical metasurfaces. *Opt. Mater. Express*, 2(4):478, 2012.

[50] Z. Q. Liu, G. Q. Liu, Z. P. Huang, X. S. Liu, and G. L. Fu. Ultra-broadband perfect solar absorber by an ultra-thin refractory titanium nitride meta-surface. *Sol. Energy Mater. Sol. Cells*, 179:346, 2018.

[51] M. Chirumamilla, A. Chirumamilla, Y. Q. Yang, A. S. Roberts, P. K. Kristensen, K. Chaudhuri, A. Boltasseva, D. S. Sutherland, S. I. Bozhevolnyi, and K. Pedersen. Thermophotovoltaics: LargeâĂŘarea ultrabroadband absorber for solar thermophotovoltaics based on 3d titanium nitride nanopillars. *Adv. Opt. Mater.*, 5(22):1700552, 2017.

[52] F. Cao, L. Tang, Y. Li, A. P. Litvinchuk, J. M. Bao, and Z. F. Ren. A high-temperature stable spectrally-selective solar absorber based on cermet of titanium nitride in sio_2 deposited on lanthanum aluminate. *Sol. Energy Mater. Sol. Cells*, 160:12, 2017.

[53] V. Kolkovsky, K. Lukat, E. Kurth, and C. Kunath. Reactively sputtered hafnium oxide on silicon dioxide: Structural and electrical properties. *Solid-State Electron*, 106:63, 2015.

[54] H. F. Jiao, X. B. Cheng, J. T. Lu, G. H. Bao, Y. L. Liu, B. Ma, P. F. He, and Z. S. Wang. Effects of substrate temperatures on the structure and properties of hafnium dioxide films. *Appl. Opt.*, 50(9):C309, 2011.

[55] 7C. Adelmann, V. Sriramkumar, S. Van Elshocht, P. Lehnen, T. Conard, and S. Gendt. Dielectric properties of dysprosium- and scandium-doped hafnium dioxide thin films. *Appl. Phys. Lett.*, 91(16):162902, 2007.

[56] J. P. Lehan, Y. Mao, B. G. Bovard, and H. A. Macleod. Optical and microstructural properties of hafnium dioxide thin films. *Thin Solid Films*, 203(2):227, 1991.

[57] A. Hinojosa and S. C. Sharma. Effects of gold nanoparticles on electro-optical properties of a polymer-dispersed liquid crystal. *Appl. Phys. Lett.*, 97(8):081114, 2010.

[58] 1B. Ding, T. C. Gao, Y. Wang, D. H. Waldeck, P. W. Leu, and J. K. Lee. Synergistic effect of surface plasmonic particles in pbs/tio_2 heterojunction solar cells. *Sol. Energy Mater. Sol. Cells*, 128:386, 2014.

[59] Q. F. Zhang, E. Uchaker, S. L. Candelaria, and G. Z. Cao. Nanomaterials for energy conversion and storage. *Chem. Soc. Rev.*, 42(7):3127, 2013.

[60] S. C. Sharma, J. Murphree, and T. Chakraborty. Photoluminescence spectra of thin films containing cdse/zns quantum dots irradiated by 532-nm laser radiation and gamma-rays. *J. Lumin.*, 128:1771, 2008.

[61] M. Sharma, S.Tiwari, and J.Bijwe. Optimization of material parameters for development of polyetherimide composites. *Mater. Sci. Eng., B*, 168:5, 2010.

[62] K. Tiwari, A. K. Singh, and S. C. Sharma. Evidence for surface plasmons in a liquid crystal containing gold nanoparticles. *Appl. Phys. Lett.*, 101(25):253103, 2012.

[63] D. Wu, C. Liu, Y. M. Liu, Z. H. Xu, Z. Y. Yu, L. Yu, L. Chen, R. Ma, J. Q. N. Zhang, and H. Ye. Numerical study of a wide-angle polarization-independent ultra-broadband efficient selective metamaterial absorber for near-ideal solar thermal energy conversion. *RSC Adv.*, 8(38):21054, 2018.

[64] X. F. Liu. Colloidal plasmonic nanoparticles for ultrafast optical switching and laser pulse generation. *Front. Mater.*, 5:1, 2018.

[65] 8C. Radder, B. S. Satyanarayana, and C. Radder. Fdtd based plasmonic light trapping analysis in thin film hydrogenated amorphous silicon solar cells. *Int. J. Renewable Energy Res.*, 8(3):1464, 2018.

[66] A. Viswanathan and S. Thomas. Tunable linear and non linear optical properties of gesesb chalcogenide glass with solute concentration and with silver doping. *J. Alloys Compd.*, 798:424, 2019.

[67] A. I. Zvyagina, A. A. Ezhov, I. N. Meshkov, V. K. Ivanov, K. P. Birin, B. Konig, Y. G. Gorbunova, A. Y. Tsivadze, V. V. Arslanov, and M. A. Kalinina. Plasmon-enhanced light absorption at organic-coated interfaces: collectivity matters. *J. Mater. Chem. C*, 6(6):1413, 2018.

[68] J. Cao, T. Sun, and K. T. V. Grattan. Gold nanorod-based localized surface plasmon resonance biosensors: A review. *Sens. Actuators, B*, 195:332, 2014.

[69] E. Petryayeva and U. J. Krull. Localized surface plasmon resonance: Nanostructures, bioassays and biosensingâĂŤa review. *Anal. Chim. Acta*, 706(1):8, 2011.

[70] Y. Q. He, S. P. Liu, L. Kong, and Z. F. Liu. A study on the sizes and concentrations of gold nanoparticles by spectra of absorption, resonance rayleigh scattering and resonance non-linear scattering. *Spectrochim. Acta, Part A*, 63(13-14):2861, 2005.

[71] S. Yoshinaga, Y. Ishikawa, Y. Kawamura, Y. Nakai, and Y. Uraoka. The optical properties of silicon-rich silicon nitride prepared by plasma-enhanced chemical vapor deposition. *Mater. Sci. Semicond. Process*, 90:54, 2019.

[72] J. S. Park, K. H. Kim, M. S. Hwang, X. Zhang, J. M. Lee, J. Kim, K. D. Song, Y. S. No, K. Y. Jeong, J. F. Cahoon, S. K. Kim, and H. G. Park. Enhancement of light absorption in silicon nanowire photovoltaic devices with dielectric and metallic grating structures. *Nano Lett.*, 17(12):7731, 2017.